

Frictional behaviour of altered rhyolitic volcanic rocks under in situ conditions in the Wairakei Geothermal Field, New Zealand

Master Thesis

J.T.F. Spierings

High Pressure and Temperature Laboratory,
Department of Earth Sciences, Utrecht University,
Utrecht, The Netherlands

Supervision: A. R. Niemeijer & C. Massiot

February 22, 2018

Contents

	<u>Abstract</u>	2
1.	<u>Introduction</u>	3
2.	<u>Geological Setting</u>	6
3..	<u>Theoretical background on slip behaviour of faults</u>	10
4.	<u>Methods</u>	14
5.	<u>Results</u>	21
6.	<u>Discussion</u>	42
7.	<u>Conclusion</u>	53
	<u>Acknowledgements</u>	54
	<u>References</u>	55
	<u>Appendices</u>	59

Abstract

The utilisation of geothermal resources disturbs the reservoir conditions due to extraction and reinjection, which may have consequences for the behaviour of faults, including triggering earthquakes and permeability enhancement. The frictional properties of the fault gouge are needed for simulation models of faults and earthquakes. The frictional properties of volcanic rhyolitic fault gouges under in situ conditions have been investigated in this study in an attempt to better comprehend the conditions in which faults slip. The frictional behaviour and seismic potential was investigated for altered rhyolitic tuffs, ignimbrites and lava fault gouges in this study. The samples used were taken from cores and cuttings originate originating from 100 m to 2 km depths from drilling in the Wairakei geothermal field in New Zealand. The frictional behaviour was tested on a ring shear apparatus by velocity stepping and slide-hold-slide experiments. The loading velocities varied between 10^{-6} - 10^{-4} m/s. The applied conditions were 50 MPa effective normal stress and 20 MPa pore fluid pressure corresponding to a depth of 2-2.5 km at Wairakei, at variable temperatures of 24, 100, 200 and 300 °C consistent with reservoir temperatures. The obtained results show coefficients of friction under the applied conditions for the different lithologies. A velocity weakening is observed under all temperatures indicating, in the framework of rate-and-state friction, that all fault gouges show the potential for unstable slip, i.e. for the nucleation of earthquakes. A sampled ignimbrite from a well in Karapiti South shows a significant weaker frictional behaviour compared to samples from the Poihipi West area. I did not observe effects of welding on the frictional strength of the simulated fault gouges. A fault re-strengthens after slip by strengthening of contacts, the increases of area contact and gouge compaction and loglinear relationship that is a time-dependent process. The healing rate of the fault gouge increases strongly with temperature. The increase in shear strength ranges from $0.004\ln(t)$ to $0.018\ln(t)$. The frictional properties of rocks in hydrothermal altered rocks and the loglinear re-strengthening of faults presented in this work will support future numerical models for fault behaviour and help in evaluating reservoir permeability.

1. Introduction

Understanding the reactivation of faults is crucial to comprehend the conditions in which fracture permeability can be increased in hydrocarbon or geothermal reservoirs (Barton et al., 1995) and also to mitigate induced seismicity risks which can occur by the injection and extraction of fluids (Ellsworth, 2013). An increase in the pore fluid pressure reduces the effective stress in a rock. The Coulomb failure criterion of a rock describes the relationship between stresses, pore fluid pressure and the coefficient of friction equation 1.1 (Scholz, 2002).

$$\tau = S_0 + \mu(\sigma_n - P_f) \quad (1.1)$$

The normal stress is σ_n in this criterion, P_f is the pore fluid pressure, μ is the coefficient of friction, S_0 is the cohesion term and τ is the shear stress. Geothermal field operators re-inject a large proportion of the produced fluids due to (1) environmental regulations and (2) to maintain the reservoir pressure. An increase in pore fluid pressure will shift the Mohr circle to the left (figure 1.1), which can cause shear or hydraulic failure of the rock depending on the magnitude of differential stress (Beeler et al., 2000). However a decrease in pore fluid pressure can stimulate the generation of earthquakes due to compaction (figure 1.2; Yerkes et al., 1976).

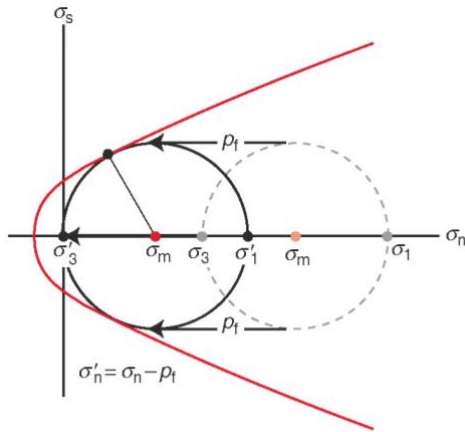


Figure 1.1: The shift of the Mohr circle due to an increase in pore fluid pressure.

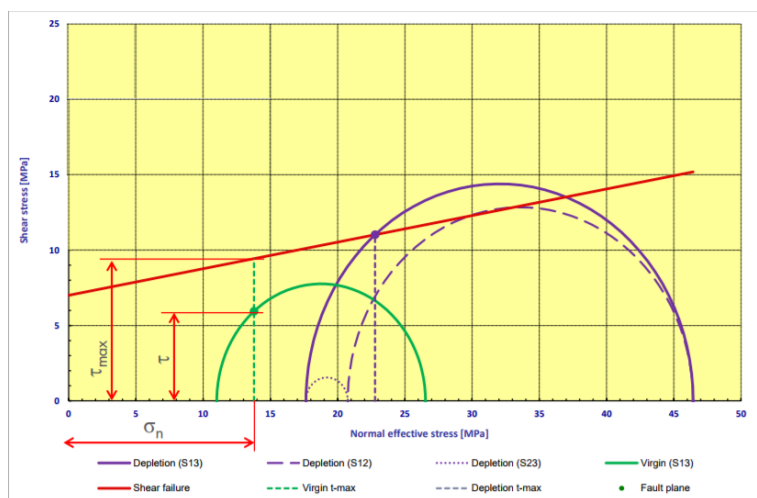


Figure 1.2: The shift of the Mohr circle due to a decrease in pore fluid pressure (from van den Bogert, 2015)

The results of extraction or injection of fluids in the subsurface can have varying consequences. Critically stressed faults, which have a high potential of slip and are located above the failure envelope in a Mohr diagram, have been demonstrated to provide the most important fluid conduits in reservoirs (Barton et al., 1995, Townend et al., 2000). Intersecting these critically stressed fractures during geothermal drilling is thus desirable, but rely on the knowledge of the coefficient of friction. Variations in reservoir fluid pressures associated with extraction or injection of fluids modify the shape of the Mohr diagram, and thus the range of fracture orientations likely to be permeable in a given stress field. In New Zealand, natural and induced micro-seismicity levels vary between geothermal fields: most earthquakes magnitudes are well below ML 2.5 (maximum of ML 3.5), which has not been an issue with local rural inhabitants who are used to this size of events (Sherburn et al., 2015). On the other hand for example, the province Groningen in The Netherlands has huge costs and social unrest, because of the gas extraction that caused induced seismicity and soil subsidence (van Thienen-Visser and Breunese, 2015). Estimating the conditions in which faults slip is only possible through acquiring a good understanding of the movement along faults.

Faults typically contain the wear product of sliding which is unconsolidated and termed fault gouge. The material properties of this fault gouge determine the frictional behaviour on the fault. The frictional behaviour of fault gouge depends on many factors such as pore fluid pressure, grain size, confining pressure, temperature, sliding distance, wear, hardness and sliding velocity. When an earthquake nucleates, slip velocity rapidly increases until it reaches seismic velocities of 1 m/s (Mizoguchi et al., 2007), however lower velocities are normally applied in the range of 10^{-6} - 10^{-4} m/s in laboratories. The fault gouge can weaken or strengthen with an increase in velocity. When it weakens it has the potential for seismic nucleation and its potential for seismic nucleation along a fault can potentially be extrapolated to nature (see section 3).

Many geothermal reservoirs are hosted in volcanic rocks, but little is known about the frictional properties of fault gouge in volcanic rocks, in particular under hydrothermal in situ conditions. Volcanic rocks have been studied for their mechanical and physical properties, such as their uniaxial compressive strengths, thermal conductivity and porosities (e.g. Smith et al, 2009; Pola et al, 2012; 2014; Heap et al., 2014, Mielke et al., 2015), but little is known about the frictional properties of volcanic rocks under in situ conditions. The Wairakei geothermal field in New Zealand is the ideal place to conduct a study on the sliding behaviour along faults in silicic volcanic rocks altered by hydrothermal fluids. In the 1950's engineers build the second geothermal plant in the world at Wairakei. The Wairakei geothermal field is still in use today and the three power stations (Poihipi, Te Mihi and Wairakei) have a combined production capacity of 353 MW (Contact Energy, 2017). In optimal performance the Wairakei geothermal field can provide the electricity consumed by 358,000 households in New Zealand (Electricity Authority, 2016). The geothermal field has been investigated in great detail over the last 60 years. Its seismicity is monitored (Sepulveda et al., 2013; 2015 etc.), faults and fractures have been mapped on surface and in boreholes (Massiot et al., 2013; McNamara et al., 2016) and its lithology and PT conditions are known (e.g. Rosenberg, 2017; Bolton, 1970; Rowland et al., 2004; etc.). Sepulveda et al. (2015) has demonstrated a connection between hydrothermal production, reinjection areas and clustered seismicity at the Wairakei geothermal field, but the nature of the seismic nucleation is not well understood. The continuation of exploitation of geothermal energy is important for New Zealand due to its large renewable energy contribution. Induced seismicity is a potentially adverse effect of production and reinjection considering the existence of the Taupo township near the Wairakei geothermal field. It is important to have a robust knowledge of the physical properties of the rocks and the frictional behaviour of faults that cross-cut them. The rocks in a geothermal field undergo alteration, which can change the physical properties of the rock and so the cohesion and friction of faults (Wyering et al. 2014). The rocks in the Wairakei geothermal fields are

suited for a comparison in alteration effects, because of varying degree of rock alteration across the field.

The aim of this project is to investigate the effect of hydrothermal alteration and rock texture on the frictional strength and stability of the faults in high temperature geothermal systems hosted in silicic volcanic rocks, with the example of the Wairakei geothermal field, New Zealand. Samples comprised cuttings and cores obtained from drilling in the geothermal field, representing the different type of rocks of the used reservoirs for production. I investigated the effect of alteration on the sliding behaviour of faults using simulated fault gouges from these samples. In addition, I tested whether samples derived from cuttings give similar results to those derived from cores and the possible effect of welding from variably welded ignimbrite rock specimens. I investigated which deformation mechanisms controlled frictional sliding of the fault gouges. Finally I suggested the implications of the experimental results for a geothermal field in a naturally seismically active region.

The experiments were conducted using the unique rotary shear apparatus in the HTP lab in Utrecht , The Netherlands, for a series of hydrothermal friction experiments. All experiments were executed under the same conditions to observe any clear differences in the frictional behaviour of the different sample types. The experiment conditions were set to create the in situ conditions in the Wairakei geothermal reservoir at 2-2.5 km depth.

2. Geological setting

The Wairakei geothermal field is located in the volcanic region Taupo Volcanic Zone (TVZ) on the North Island of New Zealand. The TVZ has a longitudinal form, that is 300 km long and 60 km wide (figure 2.1). The volcanic arc is the result of the subduction of the Pacific plate under the Australian plate (Wilson and Rowland, 2016). The zone is rifting and the formed basin in the thinned crust is filled with mainly felsic volcanic deposits and sometimes andesitic rocks. The rifting process is an intra-arc rift and called the Taupo Rift that spreads with 7-15 mm year⁻¹ as a results of crustal thinning, with dominantly NE-SW striking normal faults (Wilson et al., 1995; Villamor et al., 2017). The basement of the rift zone is made up of an assembly of greywacke metasedimentary rocks of Mesozoic age, plutons and dikes (Wood et al., 1996). The volcanic activity started with the deposition of andesitic lava's around 2 Ma (Houghton et al., 1995). Around 1.6 Ma the deposition of rhyolite commenced (Houghton et al., 1995). These rhyolitic deposits were intensive and volumetrically dominant. The central part of the TVZ is among the largest and most active silicic volcanic system on earth with a production of 0.3 m³/s (Wilson et al., 1995). The TVZ is divided in at least eight caldera centres (Wilson et al., 1995). The central segment of the TVZ, where the Wairakei geothermal field is located, is dominated by rhyolitic magmas (Houghton et al., 1995).

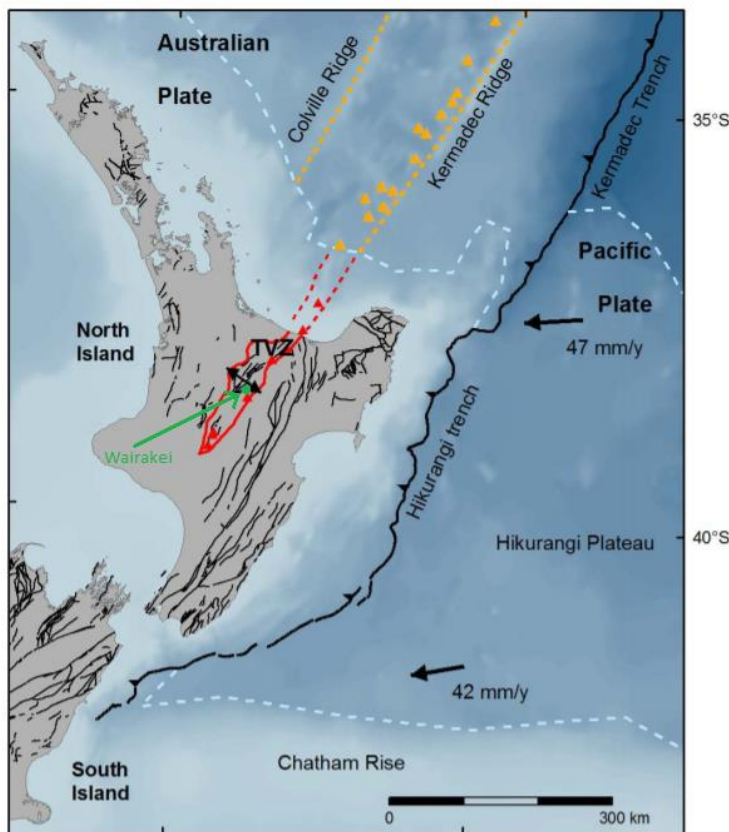


Figure 2.1: Wairakei geothermal field at the Taupo volcanic Zone on the North Island, New Zealand (from Rosenberg, 2017).

Conceptual model of the Wairakei geothermal field

The geothermal fields are uppermost manifestation of rising, high temperature, convective hydrothermal plumes (Rowland et al., 2004). These plumes originate from a depth of 7-8 km (Rowland et al., 2004). The recharge for the convective system comes from the downflow of meteoric water. The

Wairakei geothermal field is hydrologically connected to the Tauhara geothermal field that lies to the east of the Waikato river. Geothermal fields have a long life span and are stable on a time scale of 200,000 years. The geothermal fields are recognizable by shallow (<500 m deep) low resistivity anomalies, which are the result of alteration in smectite and illite near the surface (Bibby et al., 1995; Bertrand et al., 2012). The edges of the geothermal fields have a sharp increase in resistivity because of the lack of altered clay minerals.

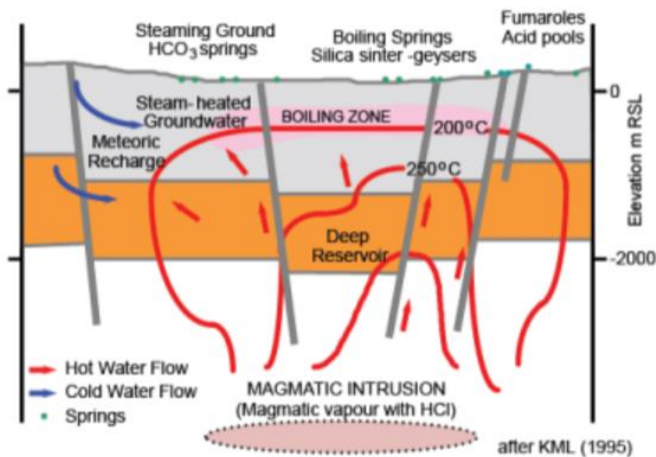


Figure 2.2: Schematic profile of the Wairakei geothermal system (from Millicich, 2013).

Some of the faults act as fluid conduits for deep fluids travelling upwards. However faults also act as barriers to flow as observed along the Paeroa fault in the TVZ (Rowland and Sibson, 2004). The flow of hot hydrothermal fluids alters rocks in geothermal fields. The Wairakei geothermal field is a geothermal field hosted in dominantly silicic volcanic rocks (figure 2.2). Deep magmatic intrusions at 8 km depth or shallower are thought to be the heat source driving the convective geothermal system. Near the surface the convective flow is blocked by an argillic zone preventing the fluids to escape to the surface, except in areas of surface thermal manifestations which represent leakage of the geothermal system to surface. This sealing cap is formed mainly by smectite-illite minerals (Steiner, 1953). The smectite zone reaches a depth of 200 m (Yang et al., 2000). Smectite is a low temperature mineral and is stable in the field till a maximum temperature of 140 °C (Steiner, 1968). The type and intensity of the hydrothermal alteration varies with depth (Bignall et al., 2010), in response to varying temperature and pressure conditions as well as permeability structure (Steiner, 1968). For instance the smectite-illite zone near the surface starts with smectite that changes into a mixture of illite-smectite and finally completely changes into illite with increasing temperature (Steiner, 1968). The reservoir is altered by a propylitic alteration beneath the smectite zone (Rosenberg et al., 2009).

Seismicity

The Wairakei geothermal field lies in a seismically active area with events of magnitude $M < 4$ and generally in the magnitude of micro-earthquake activity ($M < 2$) (Hunt et al., 2009). In the TVZ, and also at Wairakei, most of the earthquakes occur in the shallow crust with a maximum depth of 7-8 km (Bryan et al., 1999; Sherburn et al., 2003; Sepulveda et al., 2013). A proportion of the micro-seismic events in the past can be attributed to reinjection. At Wairakei, more than 70% of the total mass flow rate produced is reinjected, which has had an associated pressure recovery in the field (Sherburn et al, 2015). Figure 2.3 shows the distribution of seismic events at Wairakei between 2009 and 2012. The seismic events with M 0-4 cluster around a fault at 4-6 km depth. This fault underlies the high

temperature thermal flow at the Te Mihi sector, a production area in the northwest of the geothermal field (Sepulveda et al., 2013).

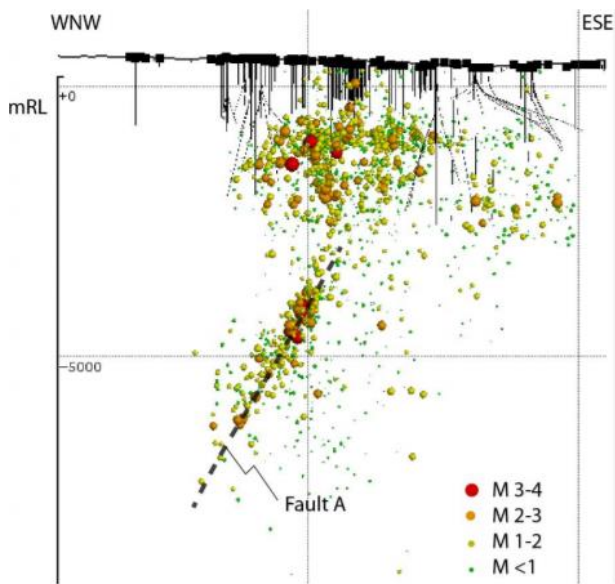


Figure 2.3: Distribution of seismic events on a cross section at Wairakei from 2009-2012 (from Sepulveda et al., 2013).

Faults

Many normal faults with displacements of several hundred meters are thought to be located within the geothermal field associated with the extension of the Taupo Rift. The geothermal field has a horst graben structure, with a dominant NE-SW fault strike with some N-S and E-W fault strikes (McNamara et al., 2016; figure 2.4). The basement of the geothermal field is expected to contain large scale NW-SE structures which represent regional scale faults, through their location and even existence remains to be proven (McNamara et al., 2016). The intersections between NW-SE structures and NE-SW trending faults may be associated with enhanced vertical permeability (Rowland and Sibson, 2004).

Stratigraphy of the Wairakei geothermal field

The stratigraphy of the Wairakei geothermal field contains a series of volcanic, volcanoclastic and sedimentary formations, most likely overlying the greywacke basement which has not been reached by drilling to date. The greywacke is supposed to occur deeper than 2250 m based on the regional structure, gravity and seismic refraction data (Rosenberg et al., 2009). On top of the greywacke basement lies the Tahorakuri formation (figure 2.4) which is a member of the Reporoa group. This formation consists of sedimentary, volcanic and volcanoclastic strata. The formation is at least 650 m thick and has a broad range in age (Rosenberg et al., 2009). The Stockyard Ignimbrite is a member of the Tahorakuri formation. It is probably a 100 m thick sheet (Rosenberg et al., 2017).

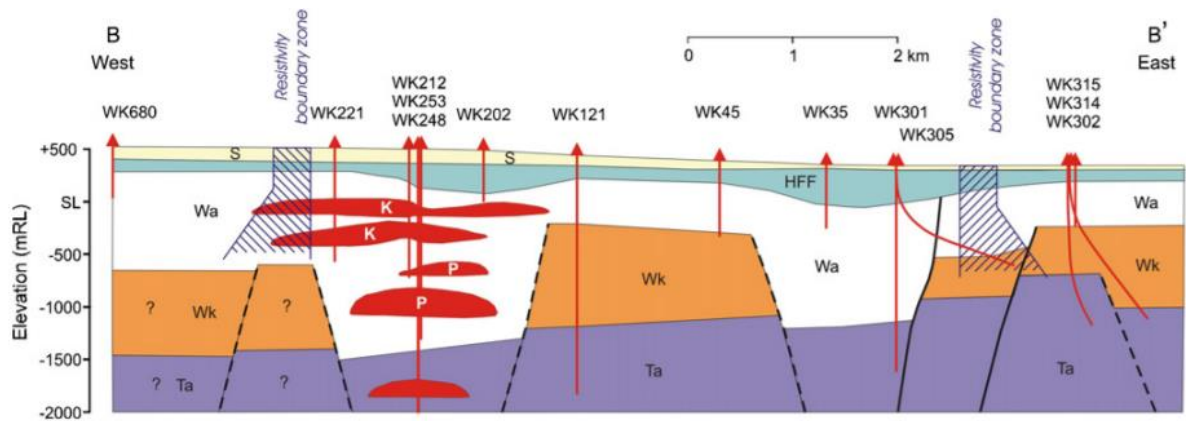


Figure 2.4: West to east cross-section of the 2D structural interpretation of the Wairakei geothermal field. The dashed lines are simplified faults. Abbreviations: Superficial (S); Huka Falls Fm. (HFF); Waiora Fm. (Wa), Karapiti (K) and Poihipi Rhyolites (P); Wairakei Ignimbrite (Wk) and Tahorakuri Fm. (Ta). mRL: metres with respect to sea level (from Rosenberg et al., 2009).

The Tahorakuri formation underlies the Wairakei Ignimbrite which is part of the Whakamaru group. The Wairakei Ignimbrite is 0.34 to 0.32 Ma old and the result of single source caldera volcanism (Houghton et al., 1995). The ignimbrite has a varying thickness from 100 m to 1000 m (Rosenberg et al., 2009). The Waiora formation lies on top of Wairakei ignimbrites. The Waiora formation is a complex sequence of varying successions of volcanic deposits, with interlayered mudstones and sandstones (Rosenberg et al., 2009). The thickness varies roughly between 400 m and 2 km. Rhyolite lavas occur within the Wairakei Ignimbrite and Waiora formation. The rhyolitic lavas in the Waiora formation are important reservoirs for geothermal production. The age of the Waiora formation is poorly constrained, but starts at 0.32 Ma. On top of the Waiora formation are deposited lacustrine sediments and water-deposited tuffs, collectively grouped into the Huka Falls formation. These sediments have accumulated in a shallow lake probably since ~ 150 Ka (Rosenberg et al., 2009). The Huka Falls formation consist of impermeable layers that seal off the hot fluids from the cool overlying groundwater. The Huka Falls formation is overlain by the Oruanui formation that exists of the deposits of the single eruption of the Taupo volcano 26,500 years ago (Wilson, 2001). The sequence comprises ignimbrites and tuffs (Rosenberg et al., 2009). The deposits from the surface down to the Oruanui formation are a combination of fluvial deposits and tephra.

3. Theoretical background on slip behaviour of faults

The simplest model for the seismic cycle on a single fault is a spring-slider model (figure 3.1; Scholz, 2002). The block is loaded through a spring with stiffness K . The stiffness represents the stiffness of the loading machine in a laboratory experiment or the elastic properties of the material around a fault in nature. As the spring is extended by a constant loading velocity (i.e. by plate motion in nature), force builds up on the fault plane which unloads when the block slides. During sliding, the force drops, the spring compresses and the movement ceases. As movement stops, the frictional strength of the fault plane is recovered and the process repeats itself. The repetitive motion is termed stick-slips, which are considered to be the laboratory representatives of earthquakes (Scholz, 2002).

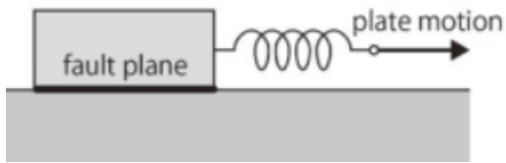


Figure 3.1: The spring-slider model (Scholz, 2002).

Friction controls the motion on a fault. A fault in nature typically contains the fine-grained product of wear of the fault interface, which is called fault gouge. The gouge determines the material properties for the frictional behaviour on the fault. The frictional strength differ along a fault during sliding or in rest. During sliding, friction is the ratio of shear to normal stress. The frictional behaviour of fault gouge depends on many factors such as pore fluid pressure, grain size, confining pressure, temperature, sliding distance, wear, hardness and sliding velocity.

$$\mu_d = \frac{\tau}{\sigma_n} \quad (3.1)$$

Dynamic friction, equation 3.1, denotes the resistance to motion during slip. Static friction is the resistance in absence of slip and has normally a higher friction unit than the dynamic friction. The static friction is the peak in friction after a hold period. The velocity reaches at this point the same value as during the pre-hold (Marone, 1998). The friction is called dynamic friction after the static friction has been reached. Friction evolves over a critical slip distance D_c consequent to a sudden change in loading velocity. D_c is the distance that is necessary to renew the surface contacts. The observations of frictional behaviour in experiments can be fitted by an empirical constitutive law, which is called the rate and state friction law. There are several variations of the law of which the best fitting one today is the Dieterich-Ruina law, equation 2 (Dieterich, 1979 & Ruina, 1983). The law depends on the slip rate V and a time-dependent state variable θ which is interpreted to be the average contact lifetime.

$$\mu = \mu(V, \theta) = \mu_0 + a \ln\left(\frac{V}{V_0}\right) + b \ln\left(\frac{V_0 \theta}{D_c}\right), \quad \frac{d\theta}{dt} = 1 - \left(\frac{V \theta}{D_c}\right) \quad (3.2)$$

In this friction law, equation 3.2, μ_0 is the friction of a steady state reference velocity V_0 . The values a and b are empirical constants. The formula can be rewritten in equation 3.3 for steady state friction assuming $\frac{d\theta}{dt} = 0$.

$$(a - b) = d\mu_{ss} \ln\left(\frac{V}{V_0}\right) \quad (3.3)$$

Equation 3.3 permits to derive the $(a-b)$ values for a velocity step by measuring the increase in friction at the two different velocities. The $(a-b)$ values tell us the stability development of the fault with an increase in velocity (figure 3.2). A decrease in dynamic friction with velocity increase is known as velocity weakening $(a-b) \leq 0$ (Scholz and Engelder, 1976). An increase in dynamic friction with velocity

is known as velocity strengthening ($a-b > 0$). Velocity strengthening results in steady state sliding along the fault.

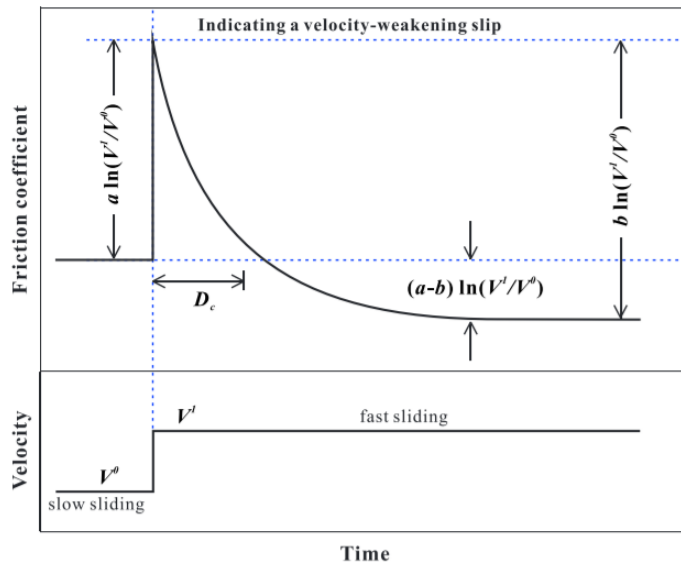


Figure 3.2: The frictional response to velocity change and the terms of the rate-and-state friction law a , b and D_c from (Chen et al., 2017).

Velocity weakening faults are conditionally unstable. Earthquakes nucleate only in an unstable regime. Between the stable and unstable regime is a Hopf bifurcation. The bifurcation happens at a critical value of the effective normal stress, equation 3.4.

$$\sigma_c = \frac{KD_c}{-(a-b)} \quad (3.4)$$

Higher normal stresses cause the system to be more unstable. The system is stable as long as it is not subjected to a large perturbation in sliding velocity, which destabilizes the system and stick-slips occur (Scholz, 2002). The size of the velocity perturbation necessary depends on the normal stress, D_c and $(a-b)$.

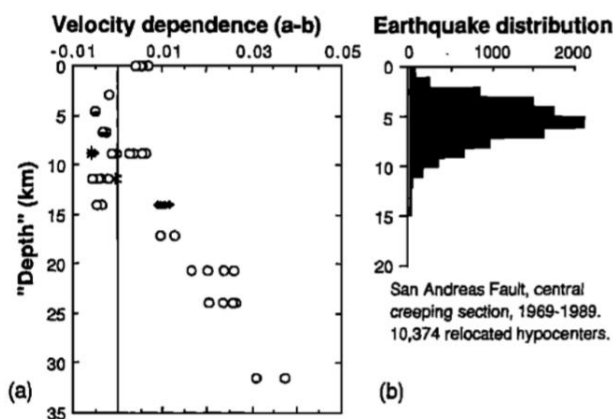


Figure 3.3: (a) The $a-b$ values of granite were determined for varying conditions and translated to a depth range and (b) compared with the earthquake distribution at the San Andreas Fault (Blanpied et al, 1991).

At low temperatures and pressure (room temperature) sliding in fault gouge occurs by frictional granular flow at critical state. Increase of temperature and pressure causes brittle-plastic transition.

Abrasive wear changes in adhesive wear on bear rock contacts (Scholz, 2002). Sliding with adhesive wear causes an unstable regime, the conditions for earthquakes (figure 3.3). A further rise in temperature and pressure shifts the regime to plastic continuum flow during sliding instead of wear (Scholz, 2002). This gives stable sliding conditions and positive a-b values. In figure 3.3 is shown the change in a-b value with depth and the number of earthquakes with hypo-central depth on the San Andreas fault due to changes in frictional processes. Those stability regimes for sliding vary per material.

Static friction increases logarithmically with hold time (Dieterich, 1972). This is healing of the fault. Healing is assumed to be the effect of three mechanisms; 1) the strengthening of contacts, 2) the increases of area contact and 3) gouge compaction that causes a higher packing density (Niemeijer et al., 2008). The mechanisms behind this are debated. One is the adhesion theory which assumes welding of contact asperities and the other theory assumes pressure solution which increase the contact between grains (McLaskey et al., 2012; Niemeijer and Spiers, 2007). The welding of asperities is thermally activated as well as pressure solution. A higher packing density requires dilation, when the fault gouge has to be re-sheared. The healing rate of the fault is affected by pressure, temperature and mineralogy (McLaskey et al., 2012). The healing rate varies with time and loading rate (Marone, 1998). Measurements of the hold time have to start with sliding to know the initiation of the hold. Plotting the duration of the hold against the change in friction delivers the logarithmically increase in static friction. The coefficient of this line is the healing coefficient. The increase in friction between steady state sliding before the hold and the peak in friction is $\Delta\mu_1$ (figure 3.4). The increase in friction between steady sliding after the hold and the peak in friction is $\Delta\mu_2$. The decay in steady state friction between the lowest obtained value for friction during the hold and the friction value at steady state sliding before the hold is $\Delta\mu_c$. Plotting the $\Delta\mu_1$ and $\Delta\mu_2$ against the hold time should give the same healing rate. $\Delta\mu_c$ depends on the relaxation rate of the gouge during the hold.

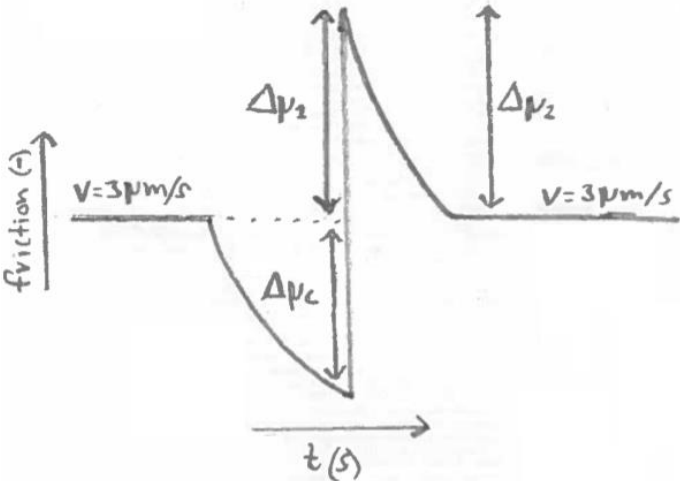


Figure 3.4: A slide-hold-slide with the indicated increases in friction $\Delta\mu_1$, $\Delta\mu_2$ and $\Delta\mu_c$.

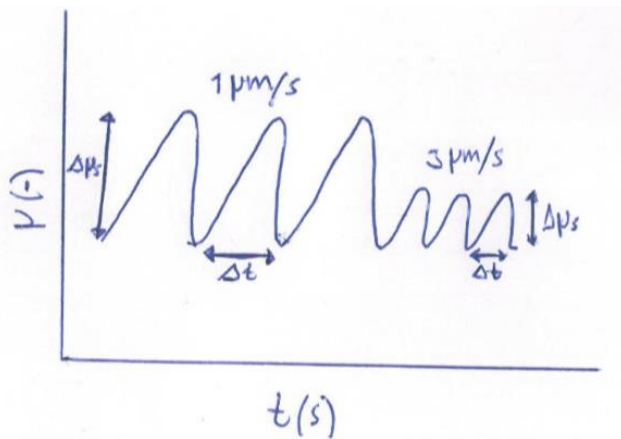


Figure 3.5: The increase in static friction derived over the duration of the stick phase at different velocities.

The healing rate is easy to obtain if the experiment has stable sliding. However, during unstable behaviour the healing rate is overprinted by the occurrence of stick-slips. During stick-slips, the sample does not slide for some time (the “stick” phase), before the stress reaches the strength of the sample and rapid slip occurs, accompanied by a stress drop. Then the process repeats itself. So in a way, stick-slips are like slide-hold-slide, except that the hold period is not controlled (the “stick” phase). However, according to theory, a lower loading velocity requires additional time for the stress to reach the strength of the sample, so that there will be a longer stick phase. A healing rate can thus be obtained by taking the duration of the stick phase and the subsequent peak in friction (figure 3.5).

4. Methods

Sampled cores and cutting have been prepared for six types of experiments, two frictional tests, three mineral determination tests and one particle size test. The Malvern particle sizer was used for determining the particle size. The frictional tests were velocity stepping and slide-hold-slide tests executed on the ring shear apparatus. The techniques used for the determination tests were X-ray powder diffraction (XRD), thermogravimetric analysis (TGA) and the scanning electron microscope (SEM).

Material

The samples were obtained from drill holes in the northwest of the Wairakei geothermal field. Six cuttings and two core samples were selected from five different drill holes (Figure 4.1 and Table 4.1).

Table 4.1: The samples and their specifications.

Sample	Drill hole	Depth (m)	Depth (m relative to sea-level)	Type	Formation	Lithology	Welded
WK261-100	WK261	100	418	cuttings	Oruanui	Tuff	Not
WK261-700	WK261	700	-182	cuttings	Waiora	Tuff	Not
WK261-1950	WK261	1950	-1432	cuttings	Tahorakuri	Rhyolite lava	
WK264-1850	WK264	1850	-1330	cuttings	Stockyard Ignimbrite	Ignimbrite	Strongly
WK271-1900	WK271	1900	-1400	cuttings	Tahorakuri	Ignimbrite	Not
WK404-1922.5	WK404	1922.5	-1489	core	Stockyard Ignimbrite	Ignimbrite	Strongly
WK681-1250	WK681	1250	-710	cuttings	Waiora	Ignimbrite	Moderate
WK681-1255	WK681	1255	-715	core	Waiora	Ignimbrite	Moderate

The samples were chosen to represent the different lithologies in the reservoir, namely ignimbrite, rhyolitic lavas and tuffs. The core and cutting samples from drill hole WK681 are spaced 5 m apart in depth and were therefore chosen to make a direct comparison between the use of samples derived from cores and those derived from cuttings. Different ignimbrite samples were chosen to investigate the potential influence of welding (WK271-1900 and WK264-1850). In general, the intensity of alteration increases with depth in geothermal fields. Samples of different depths were chosen to investigate the effects of alteration on frictional properties. WK681 lies in the Poihipi West area. It is located just outside the field, as defined from DC-resistivity survey, but shows mineralogical characteristics similar to the currently active field, suggesting that this area was geothermally active in the past. WK261, WK271 and WK264 are located together in the northwest of the field called the Te Mihi sector. WK404 lies in the south of the field next to another geothermal field called Karapiti South.

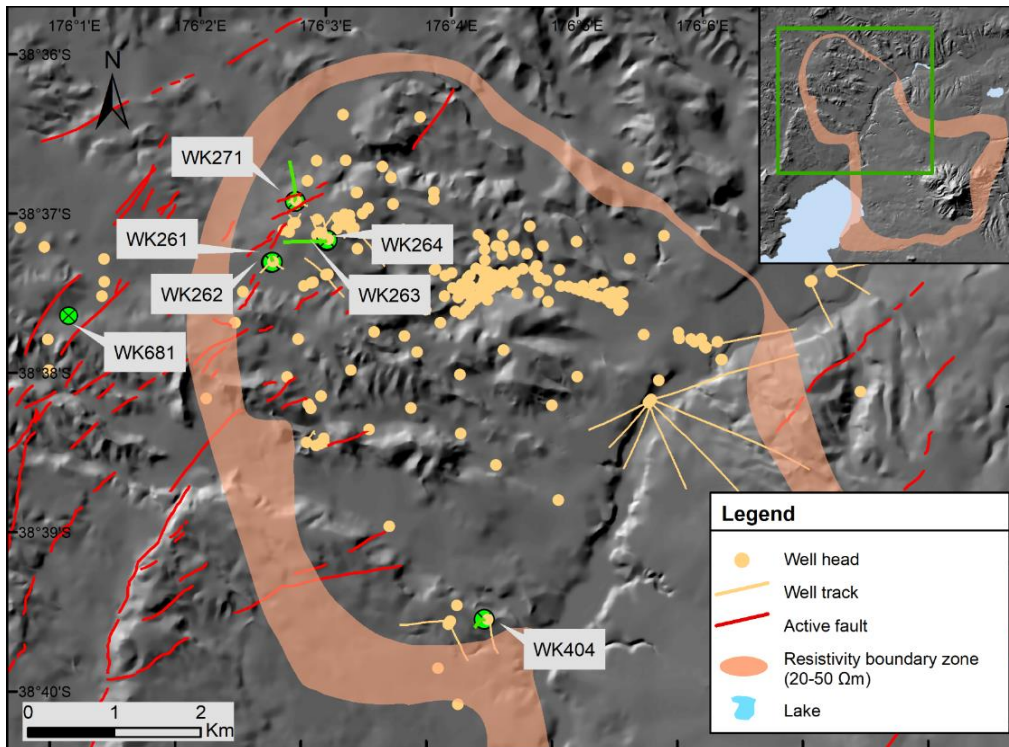


Figure 4.1: The location of the drill holes in the Wairakei geothermal field. Drill holes used in this study are labelled according to their names; mapped active faults (Langridge et al., 2016); resistivity boundary of the Wairakei geothermal field delineated by 20-50 Ωm (Risk et al, 1984). Drill holes wk262 and wk263 were not used in this study.

Sample preparation

A small grain size and with a narrow size distribution was required for the samples for using them in the XRD analysis and the rotary shear apparatus experiments. Consistency in sample grain size is also a necessity. The selected samples existed of cuttings and cores from drillings in the Wairakei geothermal field. The material was finely ground with pestle and mortar and sieved at 0.425 mm (figure 4.2; 4.3). Some sampled cuttings were contaminated with some small organic particles. They were excluded from the samples, where possible.



Figure 4.2: Core sample WK681-1255mRF
1250mRF



Figure 4.3: Cutting sample WK681-1250mRF

The grain size of the sieved powder was made more homogeneous by using the Retsch XRD-Mill McCrone. In the XRD-Mill 2,5 gram of the powder with 7 ml of ethanol was grinded for 5 min at the

machine velocity 2 and subsequently the liquid has been evaporated. Different XRD-mill speed settings were tested for the effect on the grain size distribution, but there were no significant differences. The obtained average particle size is 6 μm . The grain size distribution was tested by the Malvern particle sizer, see the result of the particle size distribution in figure 4.4.

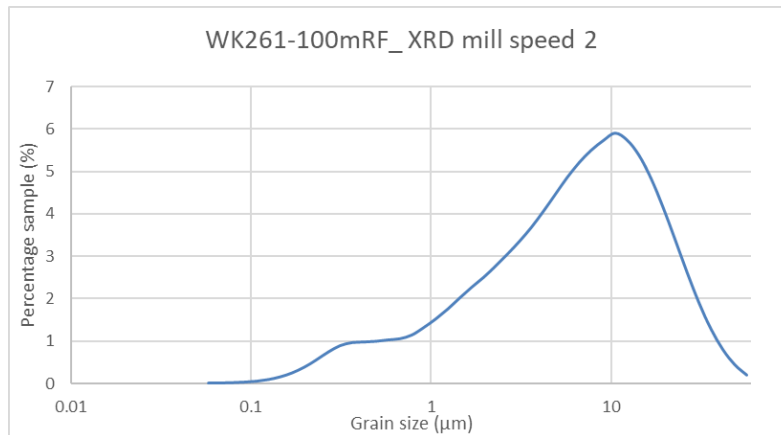


Figure 4.4: The distribution of the grain sizes for sample wk261-100 with the XRD mill speed of 2.

Prepressed rings were used for the rotary shear experiments. The rings were made by mixing 0.65 grams of the grinded sample with 0.05 grams of distilled water. This mixture was compressed in a mould for 15 minutes under 208 MPa. The compressed sample was dried overnight in an oven at 50 $^{\circ}\text{C}$ to evaporate the added water. The ring has an inner radius of 22 mm and an outer radius of 28 mm. The total surface area is 2.36 cm^2 . The obtained thickness of the samples was between 1.4 and 1.7 mm, corresponding to porosities between 10-20 %, assuming a bulk density of 1800 kg/m^3 . The starting thickness and sample weights are noted in table 4.2.

Table 4.2: The sample properties.

No.	Sample	Experiment	Mass sample	Mass water	Thickness after pressing (mm)	Mass after drying	Sample type
1	WK261-100mRF	u662 (velocity steps)	0.65	0.5	1.7	0.59	cuttings
3	WK261-700mRF	u663 (velocity steps)	0.65	0.5	1.4	0.63	cuttings
4	WK261-700mRF	u667 (slide-hold-slide)	0.65	0.5	1.3	0.58	cuttings
5	WK261-1950mRF	u671 (velocity steps)	0.65	0.5	1.6	0.62	cuttings
6	WK261-1950mRF	u679 (slide-hold-slide)	0.65	0.5	1.55	0.62	cuttings
7	WK271-1900mRF	u676 (velocity steps)	0.65	0.5	1.6	0.64	cuttings
8	WK271-1900mRF	u684 (slide-hold-slide)	0.65	0.5	1.55	0.63	cuttings
9	WK264-1850mRF	u670 (velocity steps)	0.65	0.5	1.45	0.55	cuttings
10	WK264-1850mRF	u681 (slide-hold-slide)	0.65	0.5	1.6	0.6	cuttings
11	WK404-1922.5mRF	u675 (velocity steps)	0.65	0.5	1.55	0.64	core
12	WK404-1922.5mRF	u678 (slide-hold-slide)	0.65	0.5	1.45	0.6	core
13	WK681-1250mRF	u694 (velocity steps)	0.65	0.5	1.6	0.62	cuttings
14	WK681-1255mRF	u695 (velocity steps)	0.65	0.5	1.6	0.64	core

Rotary Shear Apparatus

The rotary shear apparatus is shown in (figure 4.5) and was designed and built in the HTP laboratory in Utrecht. The functioning of the apparatus is described in detail by Niemeijer et al. (2008). The machine can simulate faults under hydrothermal conditions. The prepressed ring was placed between two pistons made of a nickel super alloy, René-41. The sample was kept between the pistons with rings

at his sides that were coated with molycoat D-321R. The pistons were placed inside a pressure vessel. The pistons in the vessel are sealed by Teflon-coating O-rings and closed by a threaded upper nut. The vessel is connected to a distilled water supply that supplies the pore fluid pressure in the sample. The sample is located inside a sheathed “thermocox” heating element that heats the sample and the pore fluid. The vessel is put into an Instron loading frame. A normal stress was applied on the upper piston and kept stationary. The lower piston with the vessel was rotated during the experiment resulting in shear of the sample. Dedicated load cells registrate the torque generated during the experiment and is converted to the shear stress. The friction coefficient during the experiment is calculated from equation 4.1, with σ_{neff} the effective normal stress, τ the shear stress measured, and μ the friction coefficient.

$$\mu = \frac{\tau}{\sigma_{neff}} \quad (4.1)$$

The generated data of normal stress and shear stress is corrected for the friction of the O-ring seals using seal friction values obtained in calibration tests (den Hartog et al., 2012).

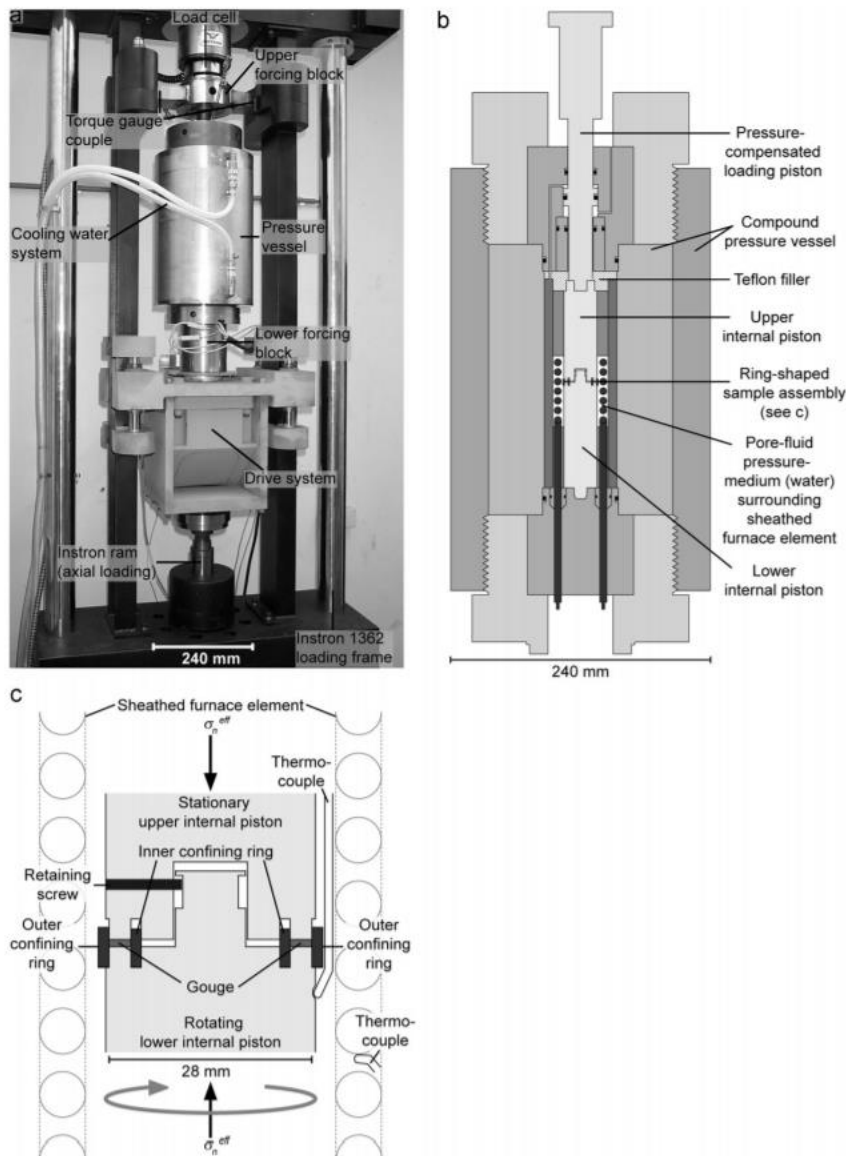


Figure 4.5 a-c: The rotary shear apparatus with indication of the different components, from (den Hartog et al., 2012).

The normal load applied to sample was 11.781 kN, which translates to 50 MPa of normal stress in the ring shear machine and the effective normal stress was kept constant during the experiment, because the piston assembly is internally compensated so that the fluid pressure does not exert any normal stress on the sample. The applied pore fluid pressure was 20 MPa during the experiments. The pressure and effective normal stress values were chosen to simulate the conditions at around a depth of 2-2.5 km in the crust. The density of rhyolitic volcanic rock varies a lot, so that an average density is roughly 2000-2500 kg/m³. The fluid pressure is assumed to be hydrostatic at depth. The Wairakei geothermal field lies in an extensional setting where pore space is freely connected and the crust is fluid saturated. Steep normal faults and fractures due to rifting connect fluid paths in low permeability strata. The density of water is almost insensitive to pressure increases, however it is very sensitive to temperature increase which will decrease the density of water. A pore fluid pressure of 20 MPa corresponds roughly to a depth of 2300 m in Wairakei Geothermal Field. The temperature was varied over the experiments to reflect different thermal regimes in the reservoir. The base temperature of the reservoir is 300 °C at 2 km depth (Milloy et al., 2014). The sample was sheared during 4 different temperatures, room temperature of 24 °C and 100 °C, 200 °C and 300 °C. Heating causes an overpressure of the fluid which was corrected by withdrawing water. After every temperature step the systems was left 20 minutes in rest to regain its equilibrium. Two types of experiments were conducted, velocity stepping and slide hold slide experiments. For both experiments the first shear velocity had a longer duration, the run-in time, to obtain a steady state shear stress and microstructure. In the velocity stepping experiments, the velocity of shearing was stepped up four times resulting in five velocities 1-3-10-30-100 µm/s with a displacement of 1.5 mm for each step, except for the run-in at room temperature which was 2.5 mm. I did a sequence of slide-hold-slides with hold times of 3-10-30-100-300-1000 and sliding at 3 µm/s with 1 mm displacement in between with also a run-in at the beginning at 1 µm/s with a displacement of 2.5 mm.

The obtained data was logged with Labview. The velocity-step data was numerically modelled in Xlook. Xlook is a modelling programme in which the rate and state friction values were obtained by inversion. The (a-b) value for the velocity steps during steady state gliding was modelled by determining the five constitutive parameters a, b1, b2 Dc1 and Dc2, following equation 3.3. Dc1 and Dc2 are characteristic displacements. Sticks-slips however are not possible to model by fitting a graph. The a-b values for stick-slips were determined by taking the peak friction and the end of a velocity step, where the most consistency in sliding is obtained. The (a-b) values are calculated with formula 3.3.

X-ray Powder Diffraction

A Bruker D8 Advance was used for the X-ray diffraction. The XRD machine has a Lyxeye detector and a copper x-ray tube. The measurements are executed at 40 kV and 40 mA in 2θ/θ mode with a detector opening of 2.95 degrees. XRD can help to identify the mineral composition of a bulk sample material. This is based on the diffraction pattern of the material. The emitted x-rays of a certain wavelength are reflected by a diffraction angle that is based on the lattice spacing in a crystalline sample. The reflected X-rays are measured and counted. This gives a certain pattern with peaks. The peaks are correlated to known mineral diffraction patterns owing to the unique patterns per mineral. A quantitative analysis was executed on the identified minerals in this study. The identification of the minerals and the quantitative analysis was done using the program Match! 3. The samples used for the XRD analysis are the same powdered material as for the ring shear apparatus.

Scanning Electron Microscope

The scanning electron microscope (SEM) was used for making high detail photographs to investigate microstructures. The used samples were the leftovers of the shear experiments in the rotary shear apparatus and came apart easily with clean break along the sliding fractures. The sheared samples were cast in epoxy, cut along a section quasi-parallel to the shearing direction (figure 4.6) and polished to obtain a smooth surface. The sections were coated with platinum and palladium to conduct the electric charge. The photographed surface of the sample is a cross section of the sheared ring (figure 4.6)

The SEM operates by shooting electrons on the prepared sample. The electrons are emitted in a focussed beam that moves over the sample resulting in building up bit by bit an energy dispersive spectrum of the X-ray emitted back by the sample. There are two modes of operation of the SEM, namely a secondary electron mode which gives about the topography of the sample and a backscatter electron mode which gives information about the composition. An analysis of the atomic composition was made for a part of sample wk264-1850. Four dots on sample wk404-1922.5 were analysed as well for their mineralogic composition. On the atomic composition was executed a quantitative analysis based on the peaks in energy dispersive spectrum. Photographs of the microstructures have been made for 5 samples (see section 5).

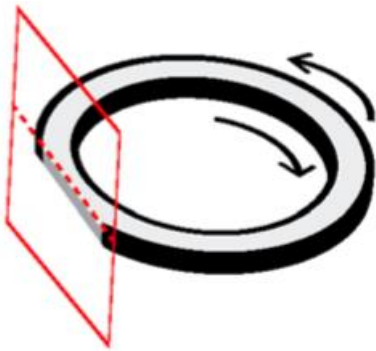


Figure 4.6: Photographed cross section of the ring shear by the scanning electron microscope (Verberne et al., 2015).

Thermogravimetric analysis

An Auto TGA 2950HR V5.4A was used for thermogravimetric analysis of the samples. The used sample powder was the same as used in the other experiments. The thermogravimetric analysis was executed for all eight samples. The used weight was 50 mg for all the samples except wk261-100 and wk261-700, for which only 25 mg was used for the analyses of wk261-100 and wk261-700. The experiment has been run with an increase of 10 °C per minute to a maximum temperature of 900 °C. A TGA analysis measures the mass of the sample over time with an increase in temperature. Different chemical reactions take place at different temperatures. From the derivative in mass change can be determined which substances lost volatiles.

Microstructures

Microstructures give information about the deformation processes that the gouge has experienced. Different kind of fractures can form during deformation of the. Logan (1992) separated these fractures based on their angle (figure 4.7). He linked the pattern of development of the fractures to the total strain. However, those experiments were executed on materials that composed only one mineral and under dry circumstances in triaxial experiments. The experiments in this study are under wet

conditions with a mineral mixture. The nomenclature of Logan (1992) is used for describing the fractures.

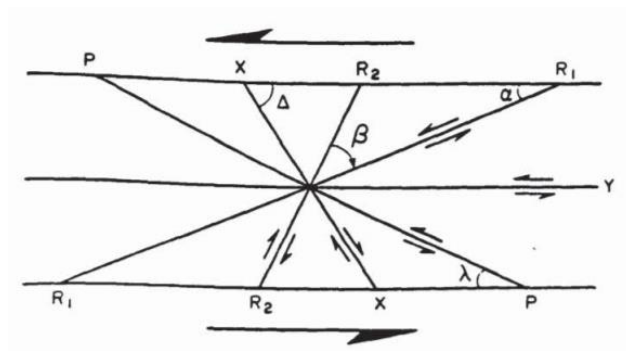


Figure 4.7: The different fractures that occur during shearing, R_1 , R_2 , x , P and Y .

Five cross sections were made in this study from the gouge remnants of the velocity steps experiments. The cross sections are made perpendicular to the shear direction. The last deformation that these samples underwent was during stick-slips with a sliding velocity of $100 \mu\text{m/s}$ at $300 \text{ }^\circ\text{C}$. The total displacement that the samples have been sheared is about 31 mm. The sample pieces have been impregnated in epoxy. They have been polished to reduce the scratches on their surface. The cross section have been photographed using the SEM. The epoxy gives a dark colour to the empty pores in the SEM photographs. The direction of shearing was not known when the pieces were put under the microscope. The samples fragments were flipped and rotated during removal of the pistons in which they were sheared. The most dominant fractures are normally the R_1 's. They were used for identifying the shear direction.

5. Results

I investigated the sampled cores and cuttings by three tests, X-ray powder diffraction (XRD), thermogravimetric analysis (TGA) and the scanning electron microscope (SEM), with the intention to determine the intensity of alteration and their mineral content. I performed two types of experiments, namely velocity-stepping and slide-hold-slide experiments to investigate the frictional properties and the seismogenic potential of the different materials and to investigate their re-strengthening (healing) potential. In the following, I will describe first the results of sample content analysis per sample, then I describe the main results of the two types of frictional experiments separately, as well I discuss the data derived from them (a-b) values and healing rates. Finally, I will present microstructural analyses of all sheared gouges from the velocity-stepping experiments

WK261-100

Those sampled cuttings are a tuff from the Oruanui formation. The sampled cuttings are contaminated with organic matter, identified by the naked eye during sieving (twigs, wood pieces), but those pieces are removed so far as possible by hand. This volcanic tuff is rich in pumice lithics. The alteration product is smectite, but the content is too low to be identifiable in the XRD spectrum. Instead, the XRD analysis shows that the sample contains quartz, albite and andesine (figure 5.1). Albite is indicated by Clayton and Steiner (1975) to be an alteration product of andesine in the Wairakei geothermal field. The ratio between them is shown in table 5.1. It is hard to distinguish between albite and andesine, because they have quite similar diffraction pattern. The chemical formula of andesine is $(Ca,Na)(Al,Si)_4O_8$ and the formula of albite is $Na_{1.0-0.9}Ca_{0.0-0.1}Al_{1.0-1.1}Si_{3.0-2.9}O_8$.

Table 5.1: Ratio's derived from the XRD data per sample.

	WK261-100	WK261-700	WK261-1950	WK264-1850	WK271-1900	WK404-1922.5	
Andesine	50.5	Quartz	85.4	Quartz	42.7	Quartz	51.1
Albite	25	Wairakite	14.6	Andesine	57.3	Albite	48.9
Quartz	24.4			Albite			

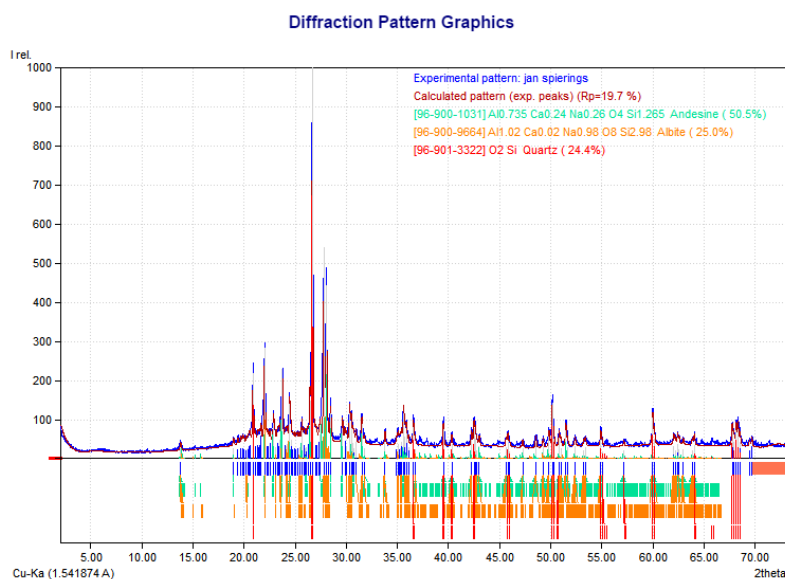


Figure 5.1: Diffraction pattern sample wk261-100 and the matched minerals.

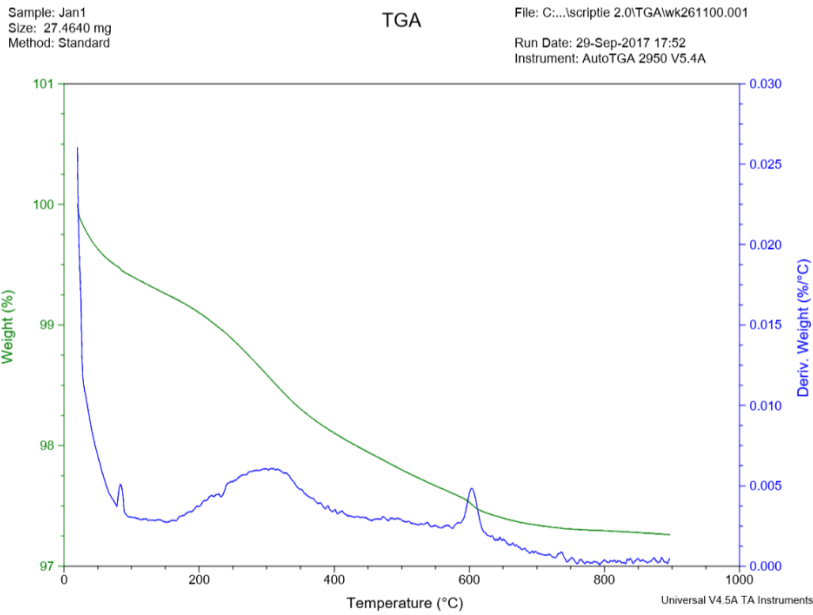


Figure 5.2: TGA measurement of wk261-100 showing the decrease in mass and the derivative of weight change with respect to temperature.

The TGA analysis of sample wk261-100 shows a mass loss of 2.7% (figure 5.2). The peaks at 80 °C and 600 °C indicates dehydration and dehydroxylation of smectite, respectively. The bulge around 300 °C is formed as the result of dehydration of Wairakite. Wairakite sometimes shows a peak at 500 °C, but that is not the case in here. The sample does not react with hydrochloric acid, indicating a negligible amount of calcite. The used hydrochloric acid was a 10% dissolution of HCL.

WK261-700

The sample is a tuff from the Waiora formation. The unit where the cuttings are taken from is indicated as an intercalated tuff with silicified mudstone and sandstones (Rosenberg, 2017). The alteration of the sample was observed to contain quartz, wairakite, chlorite, illite and calcite.

The XRD analysis shows that the minerals in the sample exist for at least of quartz and wairakite (appendix B.2). Quartz is the most abundant mineral in the sample. Wairakite is a zeolite. Zeolites form as a reaction of volcanic rocks and ash with alkaline groundwater. They are alteration products in pyroclastic material under low-temperature and low-pressure conditions (Utada, 2001). The ratio between the two minerals is presented in the table 5.1.

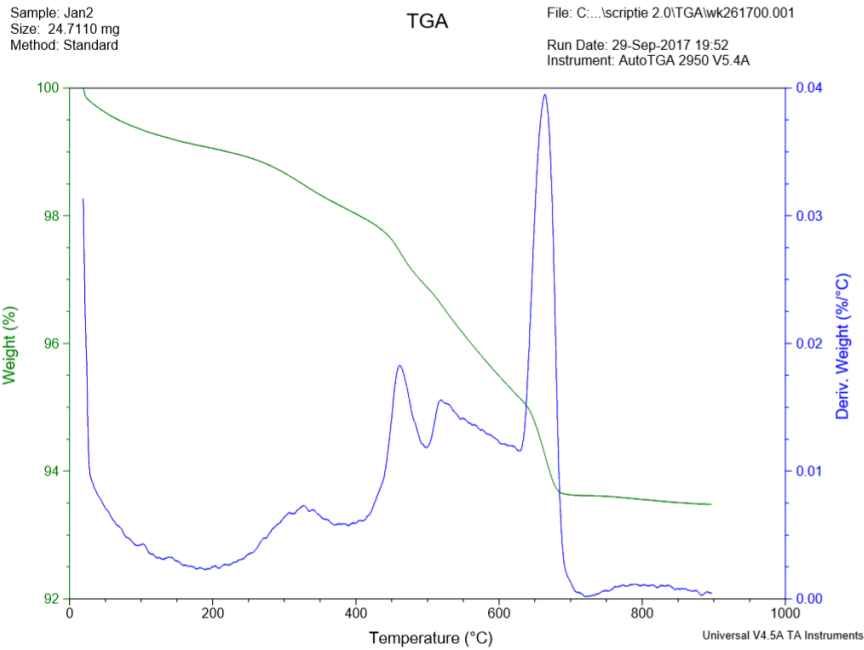


Figure 5.3: TGA measurement of wk261-700 showing the decrease in mass and the derivate of weight change.

The sample reacts with hydrochloric acid, indicating the presence of calcite. The peak at 670 °C shown in the TGA analysis thus likely corresponds to calcite, a carbonate (figure 5.3). The mass loss during the TGA experiment is 6,5% of the total weight. The biggest loss in weight is caused by calcite and shows that the calcite content has approximately a 3.4 mass percentage. At 300 °C is a bulge as result from wairakite. The bulge at 550 °C is probably a mixture of chlorite and minor content of illite. Illite dehydrates as well between 100 and 200 °C. The peak at 460 °C could be from laumontite which is a zeolite or from pyrite.

WK261-1950

The sample is a weakly porphyritic massive rhyolite lava. It belongs to the Tahorakuri formation. The rhyolite lava has a strong alteration in quartz. The alteration exists of quartz, albite, wairakite, epidote, illite and chlorite.

The XRD results show that the cuttings contain at least the minerals quartz and albite (table 5.1; figure 5.4). The peaks at the beginning of the graph are not identified. They probably belong to illite.

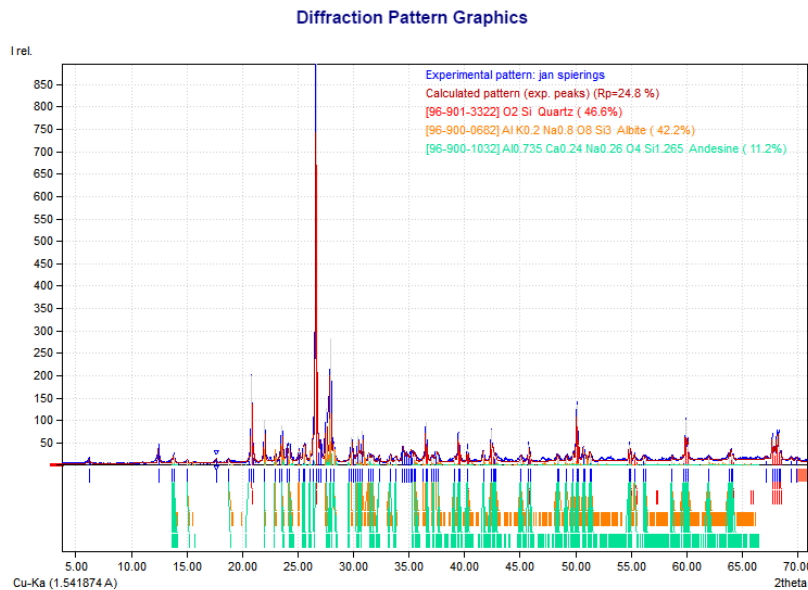


Figure 5.4: Diffraction pattern sample wk261-1950 and the matched minerals.

Sample wk261-1950 does not react with hydrochloric acid. The TGA analysis (appendix A.3) of the sample shows a decrease of 1.2% in weight. The peaks are identified as wairakite at 300 °C that has as well some losses at 500 °C. The bulge Between 500 °C and 600 °C is caused by kaolinite that has a dehydroxylation between 530 and 590 °C and probably some illite and chlorite that has losses around 550 °C. The dehydroxylation of kaolinite exists of two stage. First the removal of the OH-groups from the external surface and followed by the removal of internal OH-groups. At the end of the test near 900 °C is a rising peak. This can be a zeolite or the start of epidote. There is a small increase in weight at 800 °C, which is most likely an artefact of the measurement. The TGA results of wk261-1950 are similar to wk264-1850.

WK271-1900

The cuttings are from a non-welded ignimbrite. The ignimbrite is part of the Tahorakuri formation. Alterations in the ignimbrite exist of quartz, chlorite, illite, wairakite, albite and epidote.

The XRD matches quartz and albite or andesine for the sample (appendix B.4). Albite and andesine have both a very similar pattern in the XRD. Table 5.1 shows the ratio between quartz and albite. The ratio between quartz and andesine is roughly the same.

The TGA analysis (appendix A.4) of wk271-1900 shows a weight loss of 1.3%. The bulge around 300 °C is from wairakite. The sample most likely contains some illite and chlorite resulting in peaks at 550 °C. The peak at around 600 °C is probably from kaolinite. At the end at near 900 °C the sample shows an increase in weight loss that could indicate epidote.

WK264-1850

This sample is from cuttings from a strongly welded ignimbrite. The ignimbrite is from the Stockyard Ignimbrite formation which is a member of the Tahorakuri formation. The ignimbrite has a strong alteration with quartz. Quartz occurs in the rock in primary form and in precipitated form. The sample has also alterations of chlorite, epidote, illite, chlorite, albite and wairakite. The XRD results show the presence of quartz and albite (table 5.1; appendix B.5).

The TGA measurement (appendix A.5) shows a bulge at 300 °C and a little spike at 500 °C which are from wairakite. The big bulge from 500 °C till 600 °C is formed by kaolinite. The sample most likely contains some illite and chlorite resulting in some peaks at 550 °C. The peak at 800 °C is from chlorite. The sample does not contain calcite because it shows no reaction with hydrochloric acid and no pattern for it in the TGA analysis.

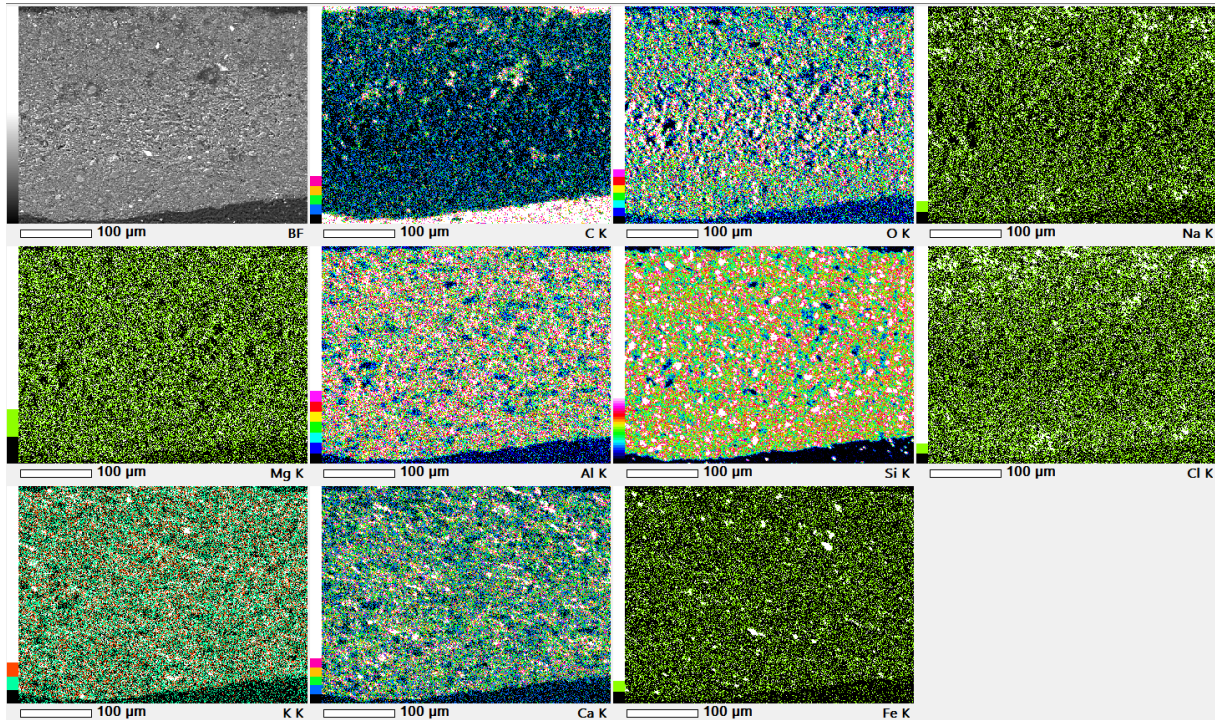


Figure 5.5: SEM scan of a part of sample wk264-1850 showing the intensity of C, O, Na, Mg, Al, Si, Cl, K, Ca and Fe atoms..

Table 5.2: The elements and their relative mass percentages measured by the SEM.

Element	Mass%	Atom%
O	53.88	68.07
Na	0.92	0.81
Mg	0.18	0.15
Al	6.48	4.85
Si	29.27	21.06
Cl	0.63	0.36
K	2.34	1.21
Ca	4.72	2.38
Fe	1.17	0.42
Total	100	100

The element analyses (table 5.2; figure 5.5) shows that most common atoms are oxygen and silica forming SiO_2 . Potassium, calcium and aluminium are the second most common elements. With SiO_2 , they form the feldspars in the sample.

WK404-1922.5

WK404-1922.5mRF is a core sample drilled in the Karapite South area. The sample is a strongly welded ignimbrite and part of the Stockyard Ignimbrite formation. The alterations contains quartz, calcite, chlorite and wairakite. The sample was dated at 1.0-1.1 Ma (Rosenberg, 2017). The XRD detected the minerals quartz, wairakite, calcite, chlorite and albite (table 5.1; appendix B.6).

The made thin section from the core sample shows a mineral content of 20%. The minerals observed in the thin section are quartz, albite, chlorite and pyroxene (figure 5.6).

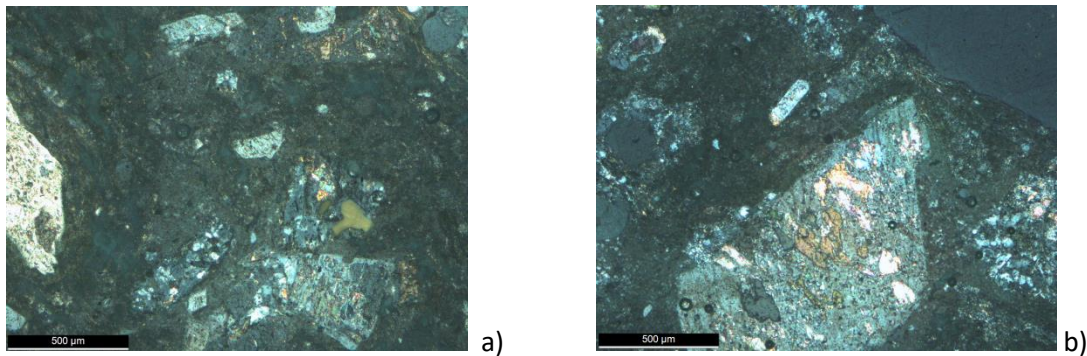


Figure 5.6: Thin section of wk404-1922.5 with in picture A quartz and plagioclase and in picture B plagioclase with inclusions.

The TGA results (appendix A.6) show a peak at 670 °C which is from calcite. The sample reacts with hydrochloric acid. The weight loss during the experiment is 3.8%. The most of the weight loss is caused by the decomposition of calcite. The mass percentage of calcite in the sample is 7.9%. The dehydration of wairakite is visible at 300 °C. The peak at the beginning of the measurement at 40 °C is the evaporation of surface water.

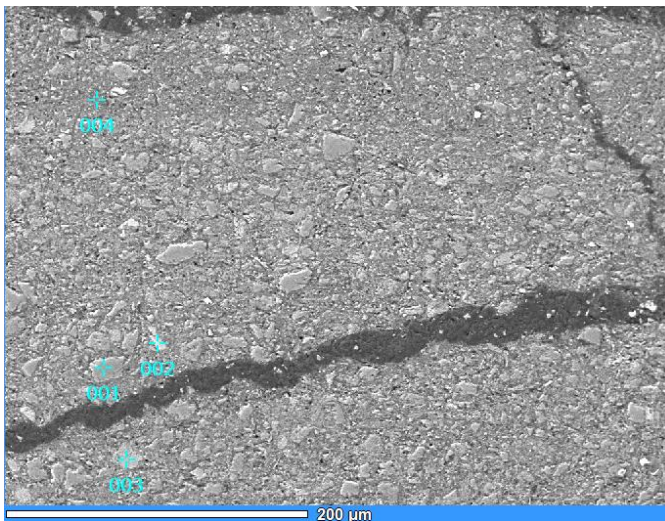


Figure 5.7: Scanned points on a part of sample wk404-1922.5

Table 5.3: The elements and their relative mass% from the scanned point on figure 5.11.

Elements point 1	Mass%	Atom%	Elements point 2	Mass%	Atom%	Elements point 3	Mass%	Atom%	Elements point 4	Mass%	Atom%
O	46.68	62.36	O	50.72	75.07	O	61.78	80.2	O	40.25	55.24
Na	5.93	5.51	Al	0.51	0.45	Ca	38.22	19.8	Na	2.71	2.58
Al	9.44	7.48	Si	1.34	1.13	Total	100	100	Al	12.06	9.82
Si	31.35	23.86	Ti	46.01	22.75				Si	35.01	27.37
Pd	0.78	0.16	Fe	1.41	0.6				K	4.57	2.56
Pt	5.82	0.64	Total	100	100				Ca	1.94	1.06
Total	100	100							Fe	3.47	1.36
									Total	100	100

Table 5.3 shows the elements that are the selected peaks from the SEM scans of the four points (figure 5.7). Point 1 consists of a mineral that is constituted of Na, Al and SiO₂. The mineral is a feldspar, probably albite. Point 2 is titanium oxide and point 3 is a calcite. Point 2 and 3 are forming both grains in figure 5.7. Point 4 is scan of the matrix and consists probably of volcanic shards that have not crystallized yet.

WK681-1255 core & WK681-1250 cuttings

The samples are from the Waiora formation. The sample is a welded ignimbrite with an age of 0.309 ± 0.014 Ma (Rosenberg, 2017). The sample has an alteration of quartz, albite, wairakite, chlorite and calcite. A thin section made from WK681-1255m (figure 5.8) shows albite, quartz, pyroxene, chlorite and a vitreous texture. The section comprises for at least of 20% of minerals.

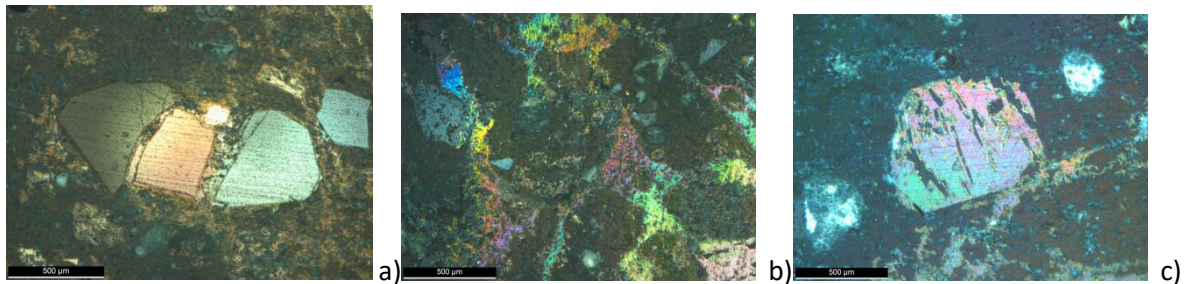


Figure 5.8: Thin section of wk681-1255 with in picture A albite, in picture B vitreous texture and in picture C a pyroxene .

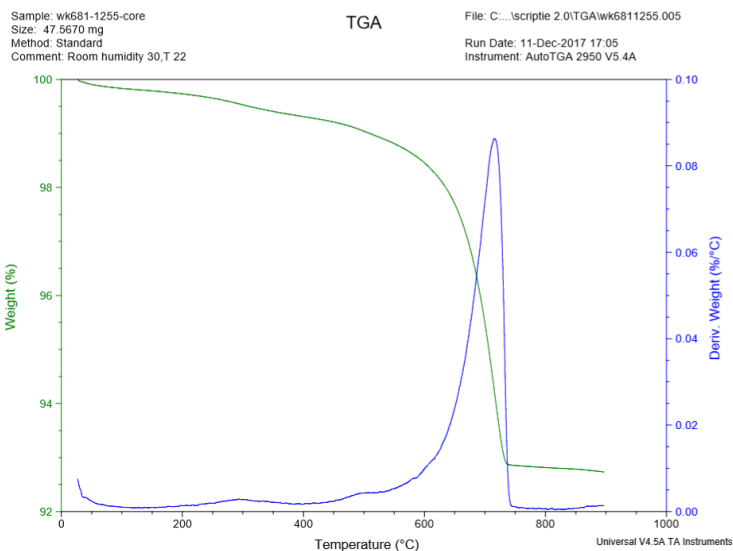


Figure 5.9: TGA measurement of wk681-1255 showing the decrease in mass and the derivate of weight change.

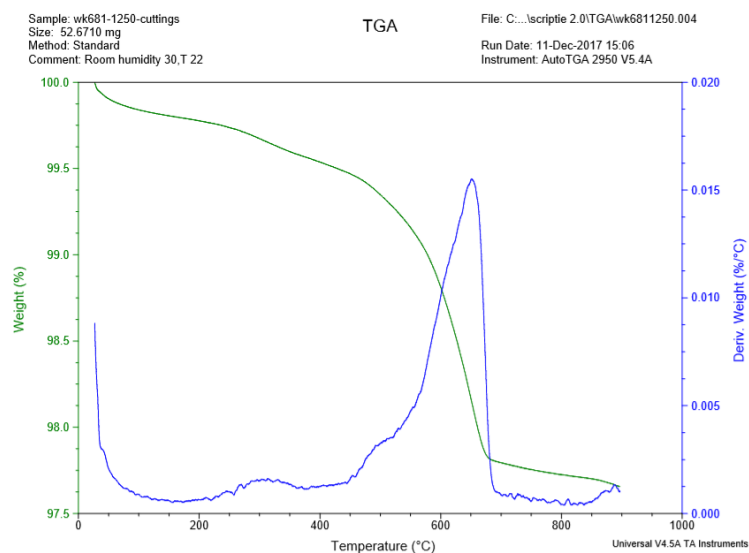


Figure 5.10: TGA measurement of wk681-1250 showing the decrease in mass and the derivate of weight change.

The TGA results of wk681-1250 and wk681-1255 both show a strong peak for calcite (figure 5.9; 5.10). Both the samples also react with hydrochloric acid. They have at bulge a 300 °C indicating wairakite. Only sample wk681-1250 has a bulge from 500-600 °C that is overprinted by the calcite peak. The bulge is from kaolinite. The mass loss is for wk681-1250 2.3% and for wk681-1255 7.3%, which indicates a mass percentage of calcite of 5.2 for wk681-1250 and 16.6 for wk681-1255.

Velocity stepping experiments

The velocity experiments (figure 5.11a-h) were all executed under the same conditions, an effective normal stress of 50 MPa and a pore fluid pressure of 20 MPa. Temperature was stepped from room

temperature up to 300 °C in increments of 100 °C and in each increment sliding velocity was increased from 1 to 100 $\mu\text{m/s}$ in half-order of magnitude steps. The sliding distances was 1.5 mm at all the velocities except at the start of the experiment at room temperature. This is the run-in, which was 2.5 mm of displacement, needed to obtain steady state friction as a starting condition for the velocity steps. The run-in starts at a displacement of zero and a friction of zero which is not shown in the figures below.

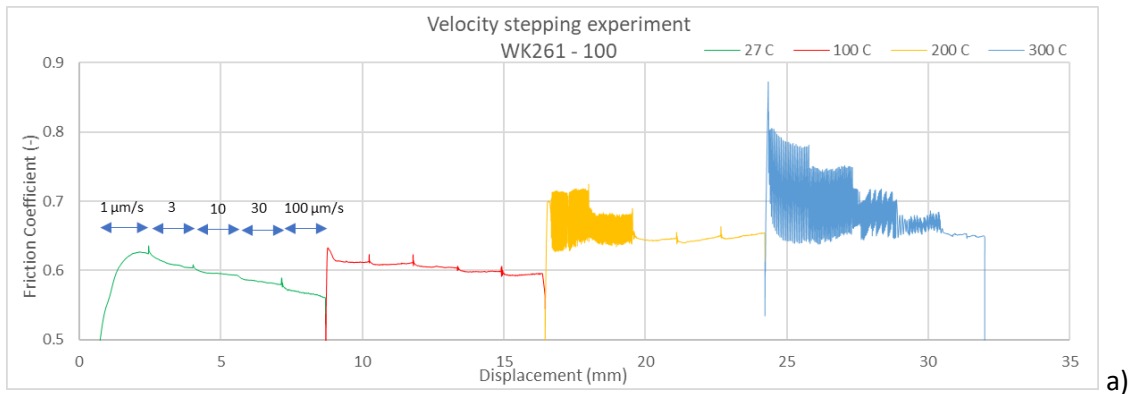
During the run-in the friction increases quasi-linearly, reaching a maximum value after which it stays at the same value except for wk404-1922.5. Sample wk404-1922.5 has a decrease in friction with distance after its highest value before the velocity stepping starts (figure 5.11e). The samples have an temporally increase in friction just after the up-step in velocity. Wk271-1900 has the highest friction value of 0.66 during the initial loading at room temperature. Sample wk404-1922.5 has the lowest peak value of 0.47 during the initial loading compared to the other samples step at room temperature. Five of the eight samples show a consistent weakening with increasing velocity at room temperature. Sample wk271-1900, wk261-700 and wk681-1255 show stable friction value with increasing velocity.

The peak friction during the first velocity step at 100 °C is for most samples a little lower than at room temperate. Only wk261-700 and wk681-1255 have a friction peak that is higher during the first velocity step. The highest peak value during the first velocity step is 0.63 for sample wk271-1900. The lowest peak value during the first velocity step at 100 °C is 0.43 for sample wk404-1922.5. The friction does not change much for sample wk261-100 and wk261-700. Wk404-1922.5 shows an increase in friction from 0.425 to 0.445. The rest of the samples show a decreasing trend in friction.

The first stick-slips occur at 200 °C. The highest peak frictions are during sliding at 1 $\mu\text{m/s}$. Sample wk261-100 and wk261-700 have the highest friction peak of 0.71 during sliding at 1 $\mu\text{m/s}$ at 200 °C. An increase in velocity has a consequence that stick-slips disappear. At which velocity step the disappearance of the stick-slips occurs, differs per sample. Sample wk404-1922.5 is the only sample that has no stick-slips at 200 °C. The lowest frictional values at 200 °C are obtained for sample wk681-1250. Wk681-1250 has a friction of 0.49 at a sliding velocity of 100 $\mu\text{m/s}$.

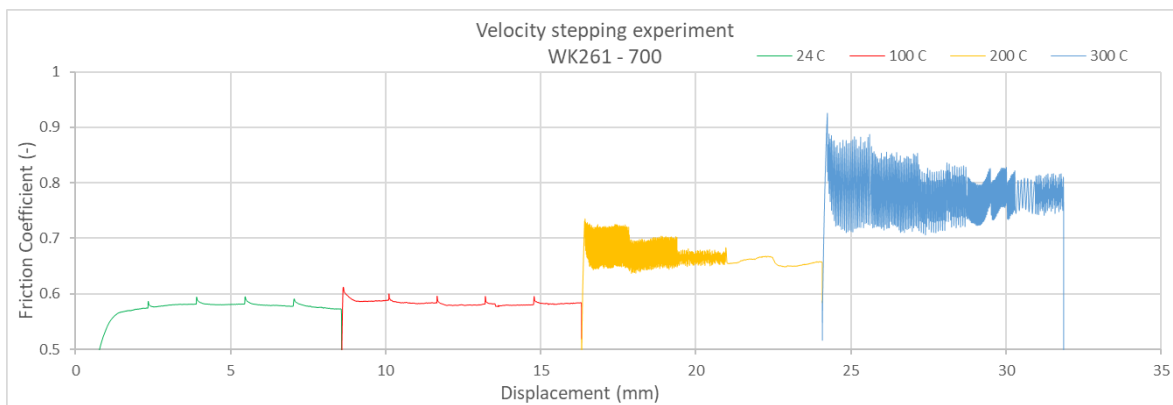
Stick-slips occur in all the samples at 300 °C. The difference in friction between the peak and the valley of a stick-slip is significant higher than at 200 °C. For example sample wk261-100 during sliding at 1 $\mu\text{m/s}$ has a difference in friction during a stick-slip of 0.08 at 200 °C, while at 300 °C this difference is 0.13. The highest frictional peak is 0.88 for sample wk261-700 at 1 $\mu\text{m/s}$. The lowest friction at 1 $\mu\text{m/s}$ at the peak of the stick-slip is 0.56 for sample wk404-1922.5 and wk681-1250. The difference in friction between peak and valleys of the stick-slips decreases with velocity increase. Sample wk264-1850 and wk261-100 have steady state sliding at a sliding velocity of 100 $\mu\text{m/s}$. Sample wk264-1850 get a higher average friction with increasing velocity at 300 °C.

The stick-slips are showing in some cases an oscillating pattern overprinted over the standard oscillating pattern of stick-slips. This oscillating pattern is observable by the change in maximum and minimum frictional values during stick-slips. This overprinting oscillating pattern is clearly observable for sample 261-100 at 10 $\mu\text{m/s}$ at 300 °C and sample wk261-700 at 30 $\mu\text{m/s}$ at 300 °C.



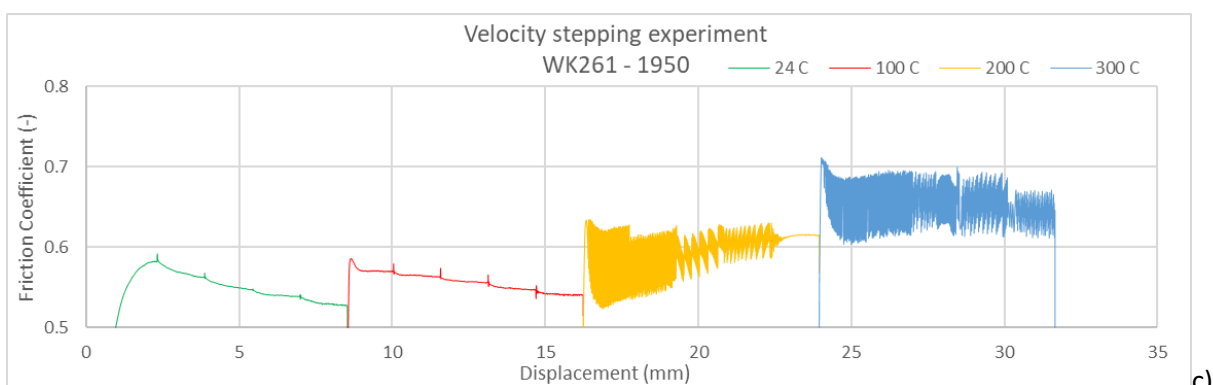
a)

Wk261-100 and wk261-700 have both a very stable pattern in friction independent of velocity increase. Only at room temperature for wk261-100 there is a clear decrease in friction with increasing velocity. The friction of wk261-100 at 100 $\mu\text{m/s}$ lies at room temperature around 0.56 and increases with increasing temperature to 0.65 at 300 °C. Wk261-100 has friction around 0.59 at room temperature that increases with increasing temperature to an average of around 0.78 at 300 °C.



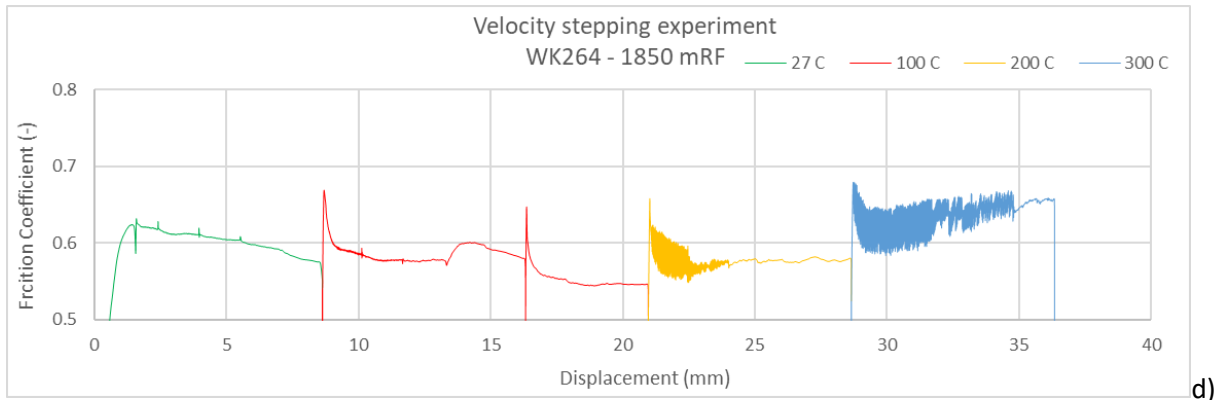
b)

Wk261-1950 has a friction coefficient between 0.5 and 0.6 at room temperature and 100 °C with clear velocity weakening trends. At 200 °C there seems to be a strengthening trend with displacement. At 300 °C the average friction is around 0.65.

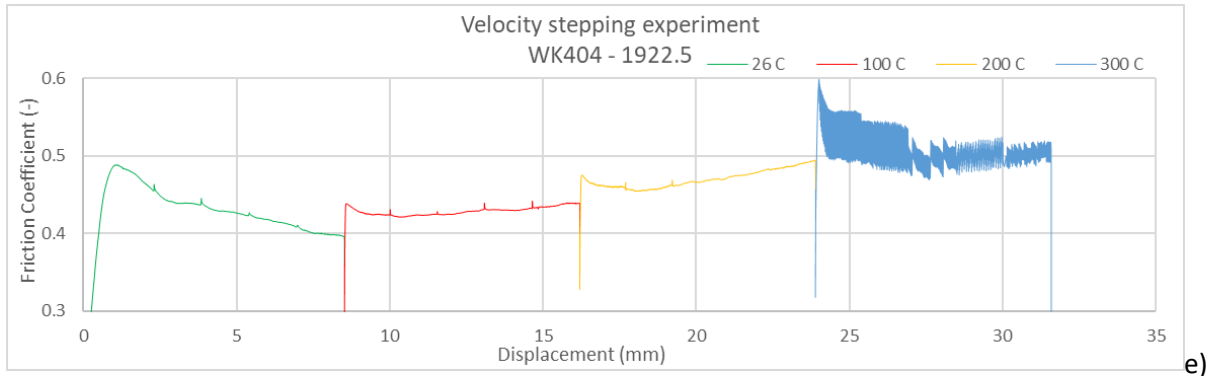


c)

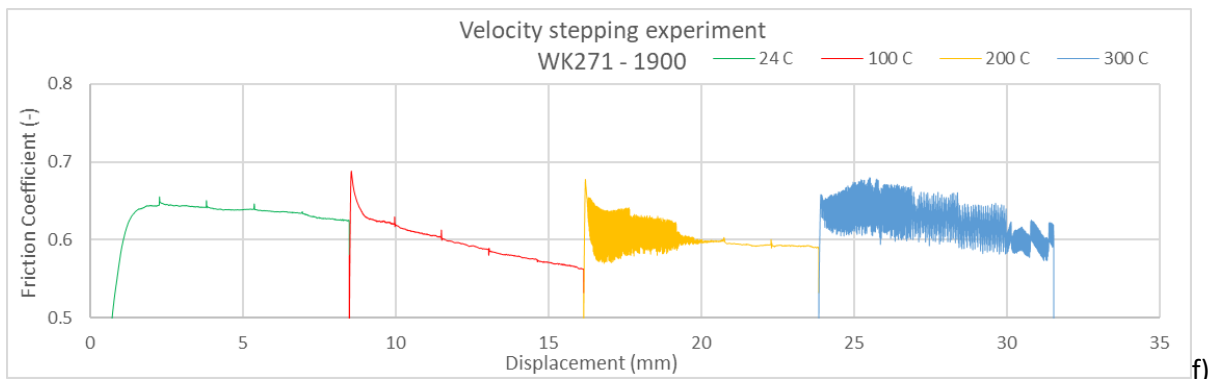
In the experiment with sample wk264-1850 a leak of the cooling water occurred during the run of the experiment at 100 °C creating the weird bulge around 15 mm displacement what resulted in missing the velocity steps of 30 and 100 $\mu\text{m/s}$. To continue the experiment, these steps were repeated starting at 10 $\mu\text{m/s}$. Something strange happens after 2 mm of sliding. There is a temporary drop in friction coefficient followed by a peak. It seems that sliding has ceased temporarily. However this is not traceable in the motor data. The friction of wk264-1850 ranges between 0.54 and 0.66.



Wk404-1922.5, sampled from the strongly welded Stockyard ignimbrite, differs from the other samples. It has the lowest friction coefficient. The friction reaches a friction of 0.4 at room temperature. An increase in temperature shows an increase in friction coefficient. Wk404-1922.5 changes from a velocity weakening trend at room temperature to a velocity strengthening trend at 100 and 200 °C. Wk404-1922.5 is the only sample that does not have any stick-slips at 200 °C.



WK271-1900 has a trend quite comparable with wk264-1850. The friction does not increase with temperature. The magnitude of the stick-slips decreases at 200 °C at a speed of 10 $\mu\text{m/s}$ and they are totally disappeared at the next velocity step. A displacement-dependent change in the peak and valley of the stick-slip stress gives an oscillating pattern at 300 °C at 100 $\mu\text{m/s}$.



Wk681-1250 and wk681-1255 are from the same depth to make the comparison between the use of cuttings and cores. They show roughly the same friction at room temperature. However in wk681-1255 the friction increases slightly with an increase of temperature, while wk681-1250 shows a decrease in friction with an increase in temperature. The stick-slips fade away and come back for both

samples during sliding at 1, 3 and 10 $\mu\text{m/s}$ at 200 °C. There is not a pattern observable in this behaviour, indicating a spontaneous behaviour.

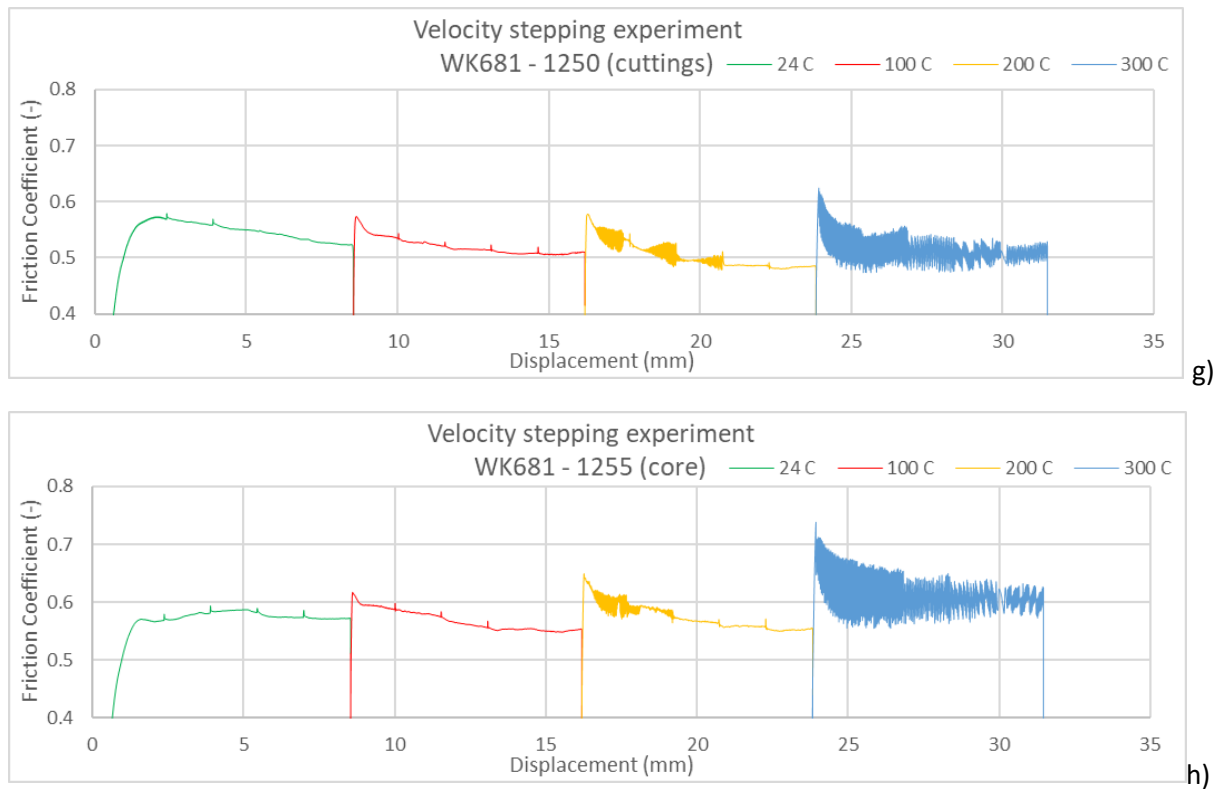


Figure 5.11 a-h: The friction vs. the displacement for the executed velocity steps experiments under 50 MPa normal stress (σ_n) and 20 MPa pore fluid pressure (P_f) with 4 velocity steps (1-3-10-30-100 $\mu\text{m/s}$) for each of the 4 temperatures. The velocity steps are indicated in figure a for sample wk261-100 at room temperature.

The layer thickness during the experiments changes due to volume loss. Volume loss can have numerous causes such as compaction due to grain crushing or due to escape of material in the setup. The normalized thickness of the velocity experiments is displayed in figure 5.12. The humps in the layer thicknesses are created by the change in temperature. The increase in temperature causes the expansion of water and the metal pistons. The overpressure of water is solved by withdrawing the water. Corrections were made for this expansion of the pistons, however the expansion is a time-dependent processes having as consequence that not all the expansion could be corrected. The thickness of the experiment with sample wk271-1900 was not measured after the experiment step at 100 °C, because the Instron position went out of scale. All the samples show a rapid decrease during the first 2 mm of sliding. Some have a higher decrease than others, however they all show only a minor decrease in thickness during sliding at 300 °C. The rate of volume loss decreases with sliding displacement. Sample wk261-100 and wk261-700 have the highest decrease in thickness. They have lost almost 25% of their volume at the end of the experiment. The other samples vary between 10 to 15% volume loss. Sample wk681-1250 and wk681-1255 show almost the same trend for volume loss.

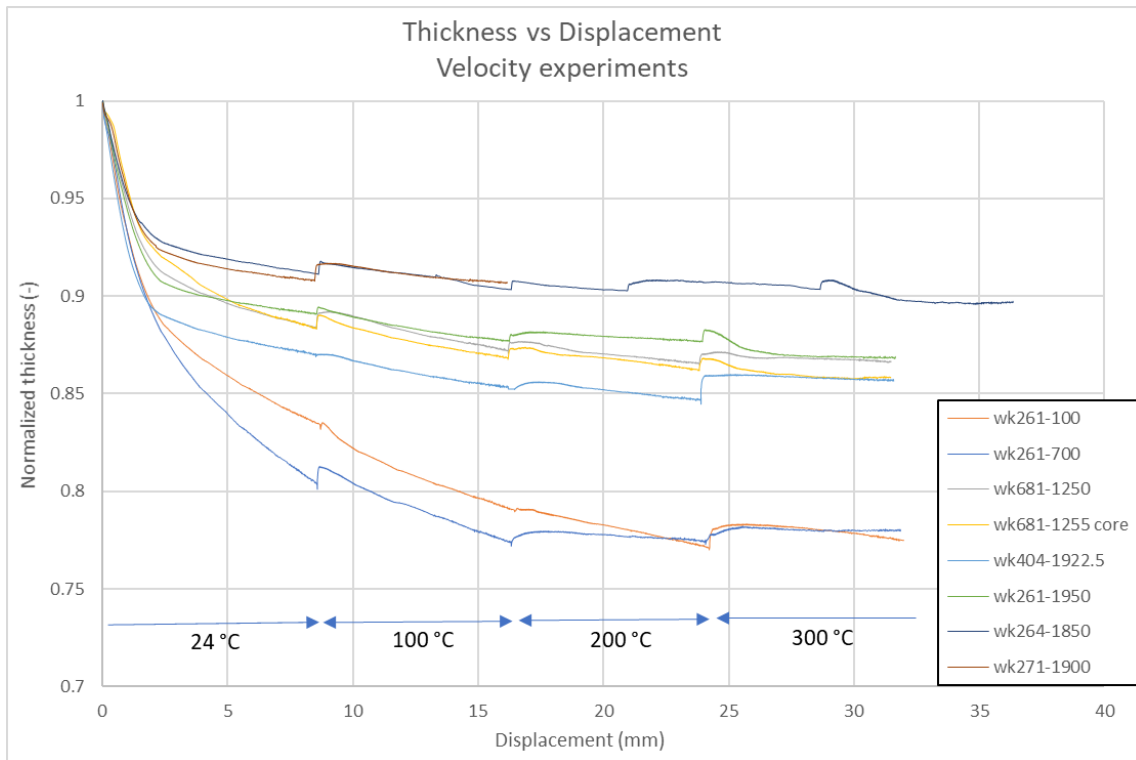


Figure 5.12: The normalized layer thickness of the sample during the velocity steps experiments.

Slide Hold Slide experiments

The slide hold slide experiments (figure 5.13; appendix C) were done under the same conditions as in the velocity experiments, an effective normal stress of 50 MPa and a pore fluid pressure of 20 MPa at 4 different temperatures.

All samples show an increase in static friction when the hold time increases. The relation between hold time and static friction is logarithmic. The static friction is observable as the peak in friction after the hold. Static friction fades away due to the intensity of the stick-slip and is no longer measurable at 300 °C and often at 200 °C. The friction values from the slide-hold-slide experiments are plotted in figure 5.13 at the different temperatures and can be compared to the friction values during sliding 3 $\mu\text{m/s}$ which have obtained in the velocity stepping experiments at this velocity step and the same displacement as plotted in 5.11. The slide-hold-slide experiment of sample wk261-700 and wk404-1922.5 are given as examples in figure 14a-b.

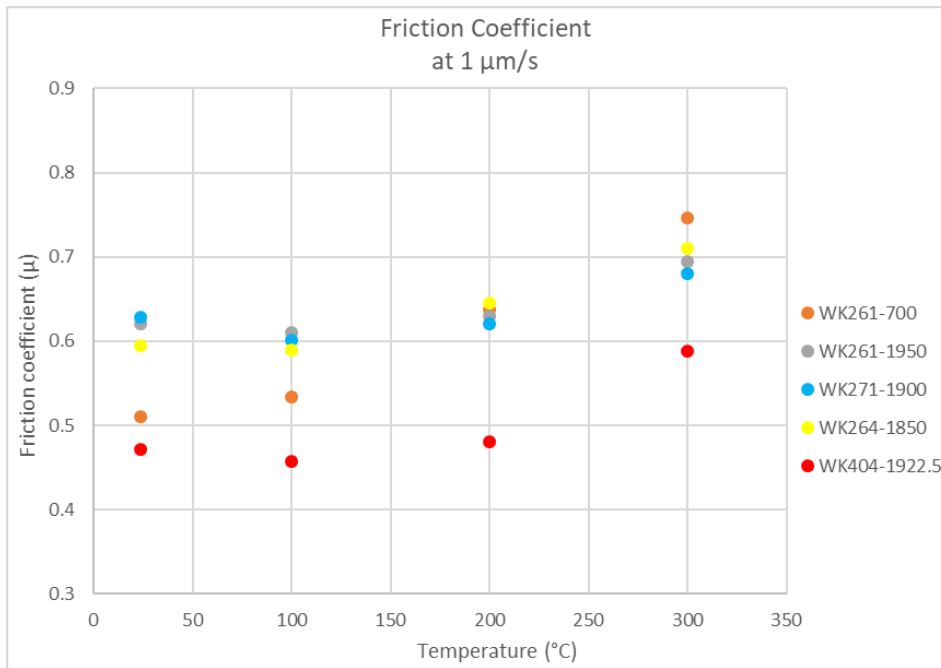
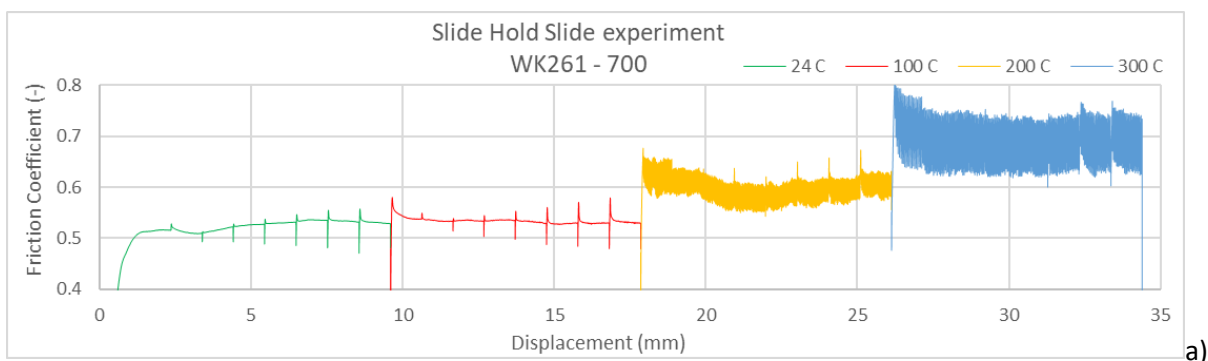


Figure 5.13: The friction plotted after 3 mm of sliding during the slide-hold-slide experiments at different temperatures.

Wk261-700 shows an increase in friction when the temperature increases, similar to that observed in the velocity-stepping experiment. The friction increases from 0.53 at room temperature to a friction coefficient around 0.7 at 300 °C. The value at room temperature is a bit lower as during the velocity stepping experiments in which it was 0.59. The friction is also lower at the other temperatures during the slide-hold-slide test. At room temperature, there is a strengthening in friction observable with increasing distance. Stick-slips occur at 200 and 300 °C. Wk261-700 is the strongest sample from the slide hold slide experiments. Wk404 is the weakest sample. It has a friction coefficient around 0.48 at room temperature and 100 °C. Occasional stick-slips are observed in between periods of steady state sliding. There is an increase in friction with displacement at 200 °C. This indicates that the material got stronger and the stick-slips fade out. The sample has constant stick-slip regime at 300 °C and the peak friction after the holds is barely visible. The sample is about 0.04 in friction stronger as during the velocity stepping experiment at room temperature. The difference in friction gets less between the two types of experiments with increasing temperature.



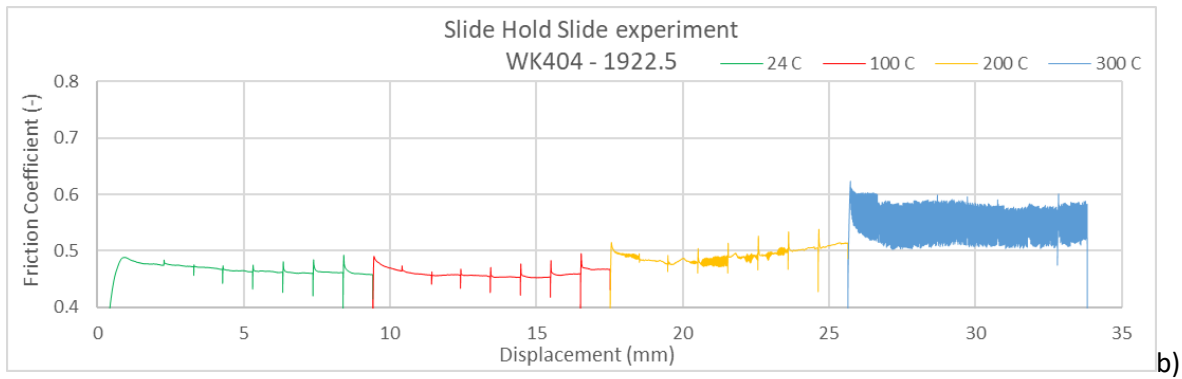


Figure 5.14 a-b: The friction vs. the displacement for the slide hold slide experiments under 50 MPa σ_n and 20 MPa P_f with 6 holds (3-10-30-100-300-1000 s) per temperature, sliding occurs at 3 $\mu\text{m/s}$.

Wk264-1850, wk261-1900 and wk271-1900 are very much the same in behaviour. They start with a friction around 0.6 at room temperature and at 100 °C. At 200 and 300 °C sliding takes place through stick-slips. The stress drops of the stick-slips are bigger in the three samples than at 200 °C.

In wk264-1850 the friction has a lower value at room temperature of 0.59 than during the velocity stepping experiments, where it was 0.62 at a sliding rate of 3 $\mu\text{m/s}$. However, the friction is higher in the slide-hold-slide experiment at 100, 200 and 300 °C. The friction decreases with displacement at room temperature. At 200 °C the friction seems to increase a bit with displacement. The change in friction with temperature is comparable with the velocity stepping experiment except at 200 °C. At 200 °C the friction does not increase during the velocity step experiment.

The values for wk261-1950 are about 0.05 higher in friction during all the temperatures compared to the velocity stepping experiment. The friction seems to decrease with displacement at 100 °C. At the other temperatures, the friction does not have displacement-dependent trends. The change in friction with temperature is comparable between the slide-hold-slide test and the velocity stepping experiment.

The frictional values are about 0.03 lower at room temperature as during the velocity stepping experiment for sample wk271-1900. The friction is quite comparable at the other temperatures between the two types of experiments. Wk271-1900 shows a decrease in friction with displacement at room temperature and at 100 °C. The change in friction with temperature is comparable between the slide-hold-slide and velocity stepping experiment.

(a-b) values

The velocity varies during the slip event of a stick-slip, but friction is velocity dependent, so the obtained (a-b) value for stick-slips is less reliable. Sometimes sliding changes from stick-slip into steady state sliding with an up-step in velocity. This also gives deviation for the (a-b) values. In some cases, it is not possible to obtain an (a-b) value. In these cases the stick-slips are not stable and they disappear and return irregularly during the same velocity step. Their (a-b) value cannot be modelled and cannot be calculated.

The (a-b) values obtained in the velocity-stepping experiments are shown in Figures 5.15a-g as a function of up-step sliding velocity. The velocity is plotted on a log scale to find log-linear trends in (a-b) values. In most samples the (a-b) values are clustering around 0 at room temperature and 100 °C. They get a more negative (a-b) value with increasing velocity. The same trend as at room temperature

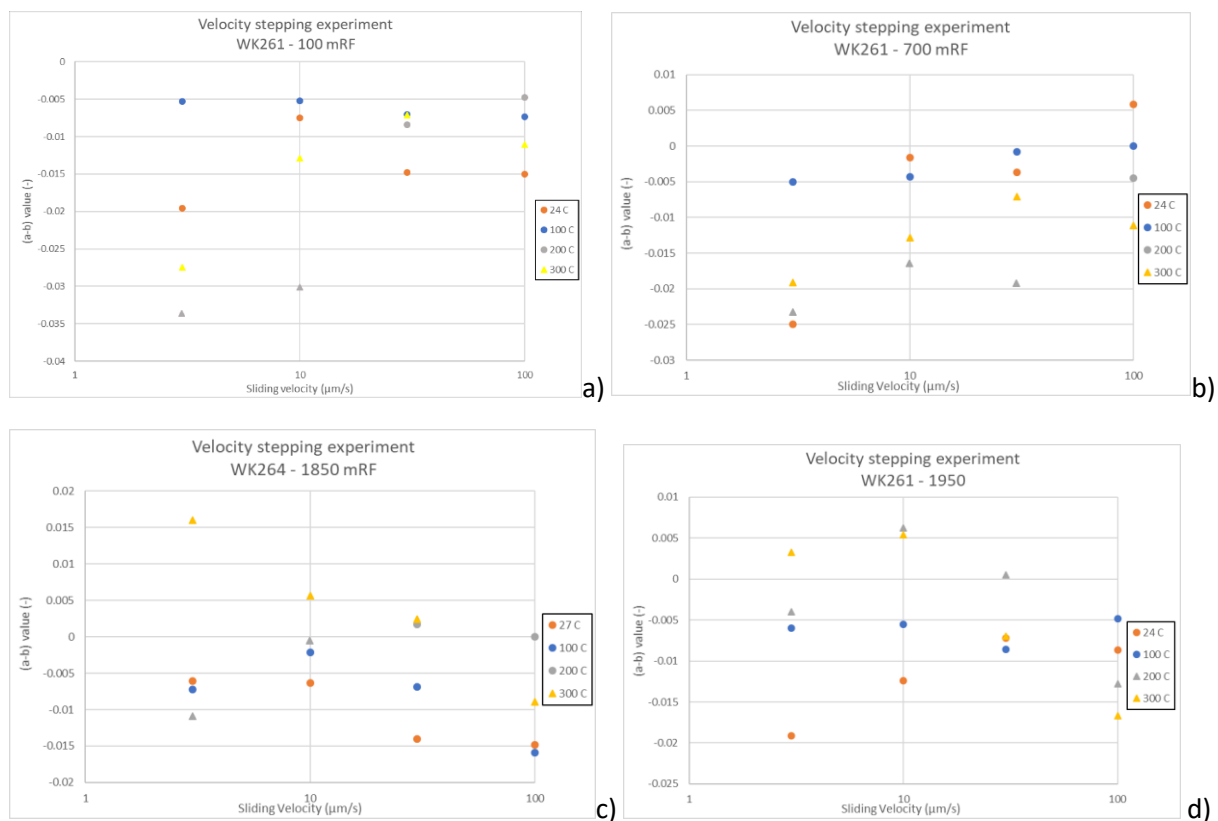
and 100 °C is noticeable at 200 °C. At 300 °C negative (a-b) values get more positive with increasing velocity. At room temperature the (a-b) values don't change much.

Wk261-100 has a roughly constant (a-b) value at room temperature and 100 °C. At the higher temperatures the a-b values get less negative with an increase in velocity. The sample has only negative values for (a-b).

Wk261-700 shows an increase in (a-b) value with sliding velocity for all the temperatures. At room temperature the (a-b) value has an increasing trend with velocity. The (a-b) value changes from negative to positive at 100 μm/s up-step sliding velocity. At 100 °C the value of (a-b) increase only a bit with velocity through which the value becomes zero.

At room temperature, wk264-1850 has with a positive value for (a-b) and changes with an increasing velocity to negative value. The (a-b) values at the lower temperatures 24 and 100 °C show a hyperbolic trend. The (a-b) value obtained from the first velocity step at 300 °C shows a deviating value that is positive compared to the other values at the same velocity.

Wk261-1950 has a hyperbolic trend for the higher temperatures. At 200 and 300 °C the (a-b) values become higher at the step from 3 to 10 μm/s. Hereafter the (a-b) values decrease for both temperatures and they change to negative (a-b) values. At room temperature there is an increasing trend in an (a-b) values that become less negative. At 100 °C the (a-b) value seems to be independent of the velocity steps and stays around a value of -0.005.



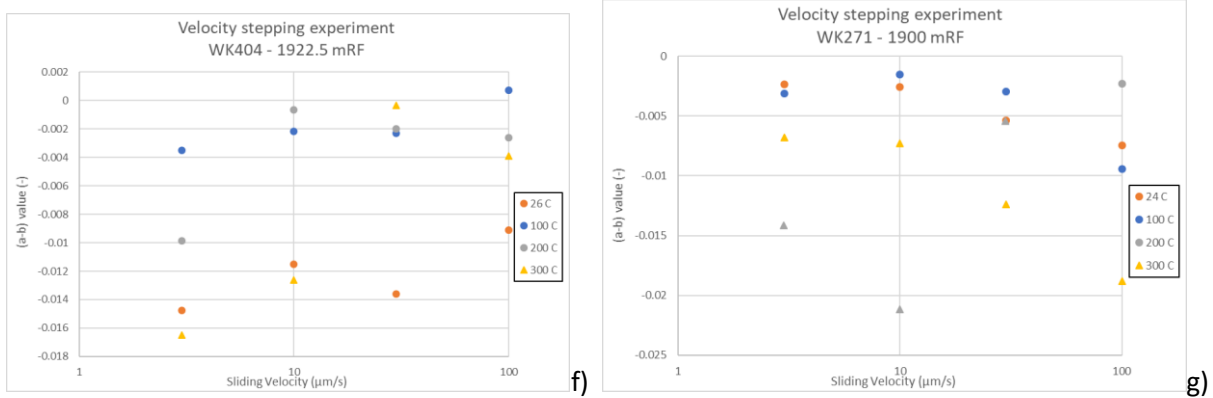


Figure 5.15 a-g: The (a-b) values plotted against the up-step velocity for the different temperatures per sample. The triangles are obtained from stick-slips and the circles from steady state sliding.

Sample wk404-1922.5 shows negative (a-b) values for all but one points on the plot. At 100 °C, there is a trend of increasing (a-b) values with increasing velocity. At 300 °C, the (a-b) value shows a large increase between the up-step velocity 10 μm/s and 30 μm/s. The (a-b) value changes from -0.012 to 0. The same change in (a-b) values is visible at 200 °C, but this change occurs a step earlier when the velocity changes from 3 to 10 μm/s.

Healing rates

The static friction of fault gouge starts to increase the moment rocks stop sliding. The slide hold slide experiments provide the means to measure the increase in frictional strength during the hold time. Plotting peak friction upon re-shear against the hold time yields a loglinear healing rate (figure 5.16). The $\Delta\mu_1$, $\Delta\mu_c$ $\Delta\mu_2$ are explained in the theoretical background. However the increase in static friction is only clearly measurable in the slide hold slide experiments during steady state sliding. The stick-slips overshadow the effect of healing. The velocity steps experiments are used to obtain the healing rate during stick-slips. The friction increases during the slip phase, which gives a loglinear relationship between the increase in friction and the recurrence interval of the stick-slip. Plotting these two against each other also yields a line for the healing rate (figure 5.17).

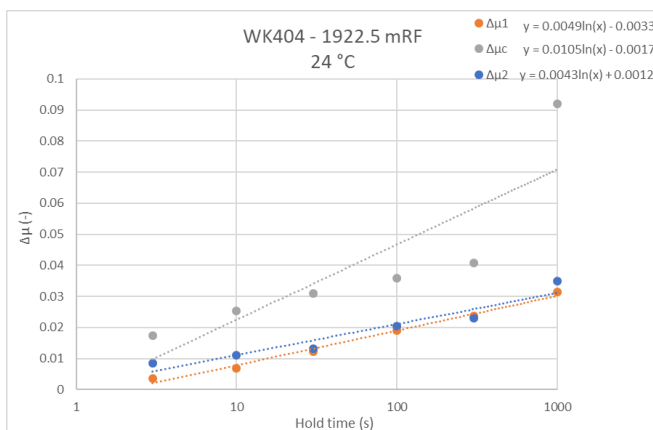


Figure 5.16: The increase in static friction vs. time from the hold slide hold experiment of wk404-1922.5.

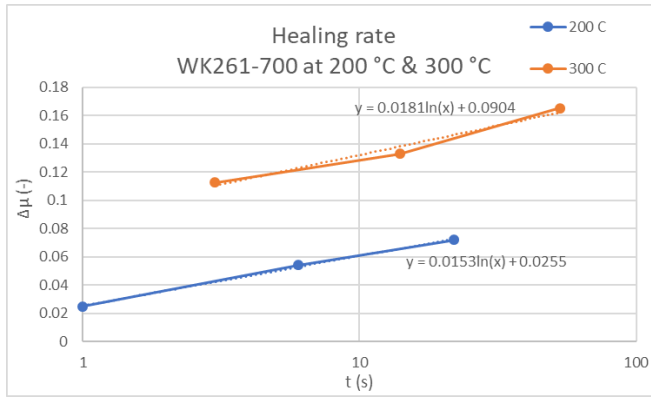


Figure 5.17: The increase in static friction vs. time from the velocity steps experiment of wk261-700.

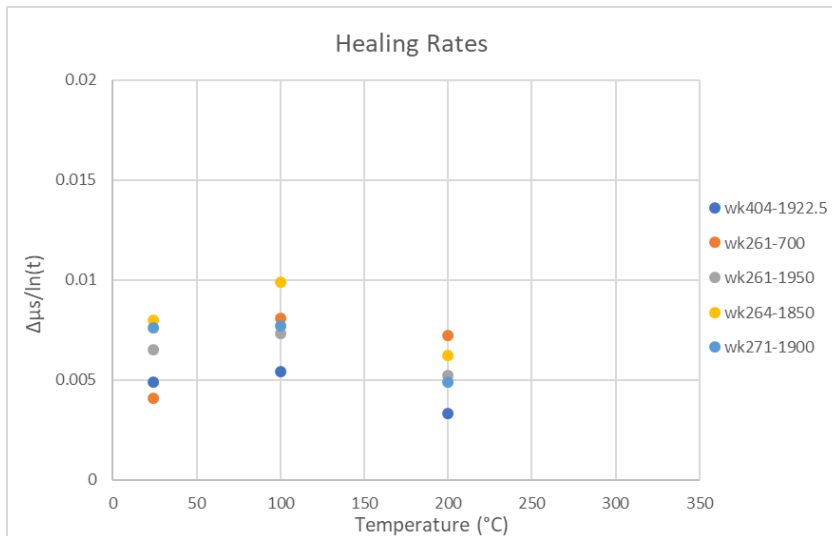


Figure 5.18: The healing rates obtained from the slide hold slide experiments. The values at 200 °C are obtained from stick-slips except for sample wk404-1922.5.

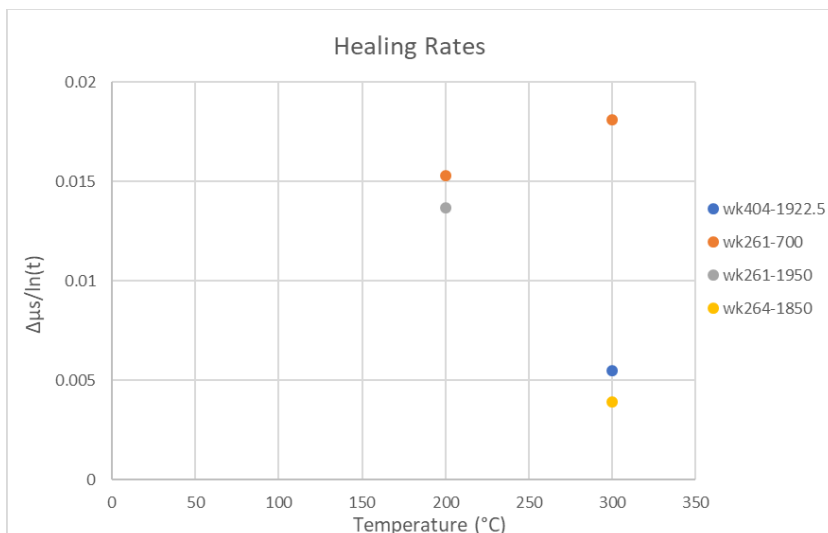


Figure 5.19: The healing rates obtained from the velocity steps experiments.

The healing rates obtained from loglinear fits to the peak friction are shown in Figures 5.18 and 5.19 as a function of temperature. Most of the healing rates at room temperature and 100 °C are between 0.004 and 0.008. Wk264-1850 has the highest healing rates reaching 0.01 at 100 °C. Wk404-1922.5

has the lowest healing rates of 0.0033 at 200 °C. Wk261-700 has the same healing rate at 100 °C as wk271-1900. The healing rate of wk271-1900 increases 92% from room temperature to 100 °C, while for the other samples the healing rate show a much lower increase in healing rate with temperature varying from 4 to 24%. The obtained healing rates for the higher temperature differ between the velocity steps experiments and the slide hold slide experiments. The data from the velocity stepping experiments shows higher healing rates at 200 °C. Only sample wk404-1922.5 does not have stick-slips at 200 °C and it has a value for the increase in static friction coefficient of 0.0033, which is four times lower than the healing values obtained for the other samples at 200 °C from the velocity stepping experiments. For sample wk261-1900, it was not possible to measure a healing rate at 200 and 300 °C, because of unregular behaviour of the stick-slips resulting in incorrect healing rates. It is strange that sample wk264-1850 has a lower rate measured from the velocity steps experiment at 200 °C than measured from the slide hold slide experiment. Also, it is noteworthy that sample wk264-1850 has a lower healing rate at 300 °C than at a lower temperatures, while the healing rate of the other samples increases a lot at 200 and 300 °C ignoring the healing rates obtained at 200 °C from the slide-hold-slide experiments that were obtained from stick-slips.

Microstructures

Sample wk261-100 has a thickness under the microscope of 0.8 mm (figure 5.20). The sample had a thickness of 1.1 mm after the experiment, so there is 0.3 mm missing of its boundaries. The large grains are salient in the centre of the sample compared to its edges. A smooth continuous band of very fine grains (comminute) is visible at both edges (5.21). These comminuted bands can be followed throughout the whole sample. The direction of shearing on the picture (figure 5.20) is sinistral, inferred from the R_1 fractures. The sample contains Y fractures and P fractures. The sample has some fractures perpendicular to the shearing direction which probably formed during preparation of the sample for the SEM.

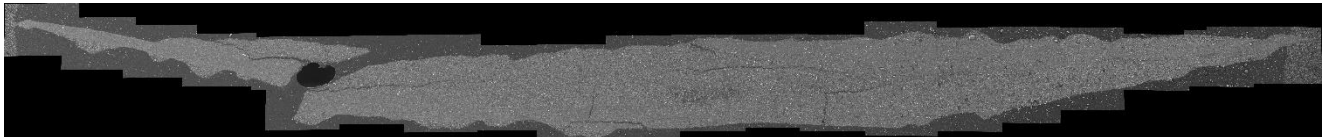


Figure 5.20: Cross section of sample wk261-100 experiment U662 made by SEM, scale vertical side is 1.2mm.

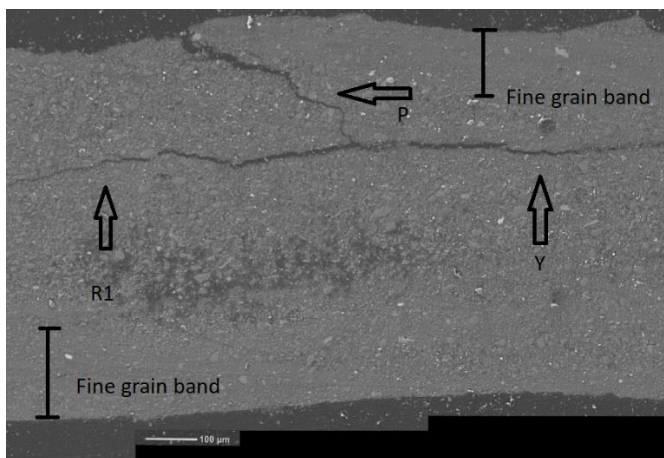


Figure 5.21: Cross section of sample wk261-100 experiment U662 made by SEM, indicated are R_1 , Y and P fractures and the fine grained bands. Scale vertical side is 0.9 mm.

Sample wk261-1950 has R_1 fractures indicating a sinistral sense of shear on the picture (figure 5.22). The sample has some cracks near the edges as a result of sample preparation. There are some thin Y fractures observable in the sample. The largest grains are roughly $20\ \mu\text{m}$. At the top of the sample is a band with fine comminuted grains. The fine grain band is easy to distinguish from the coarser material (figure 5.23). The sample thickness is nearly complete on the left side of the sample, which is 1.6 mm.

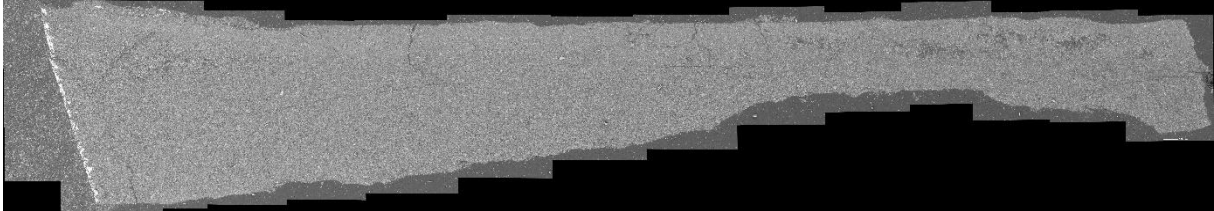


Figure 5.22: Cross section of sample wk261-1950 experiment U671 made by SEM. Scale vertical side is 1.6mm.

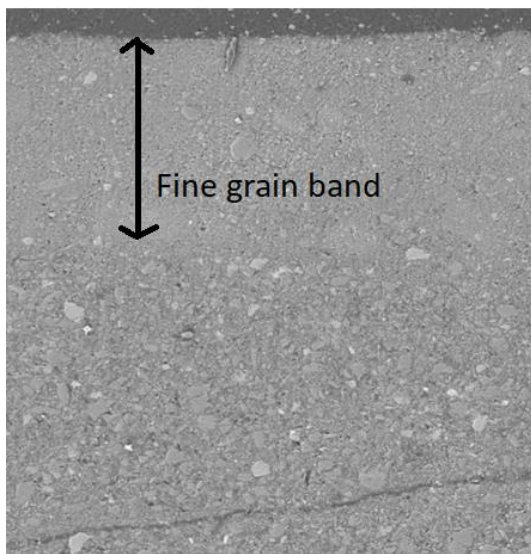


Figure 5.23: Cross section of sample wk261-1950 experiment U671 made by SEM. Scale vertical side is 0.6 mm.

Sample wk271-1900 has a lot of dark areas inside that are the result of epoxy filled holes (figure 5.24). Probably grains were plucked out during preparation for the SEM. The sample has a boundary-parallel band with a finer grain size near the upper edge. This band is about $200\ \mu\text{m}$ thick. The sample has R_1 fractures. The R_1 fractures indicate a sinistral sense of shear. Y fractures are also visible and connected with the R_1 fractures. The thickest part of the sample is 1.2 mm thick.

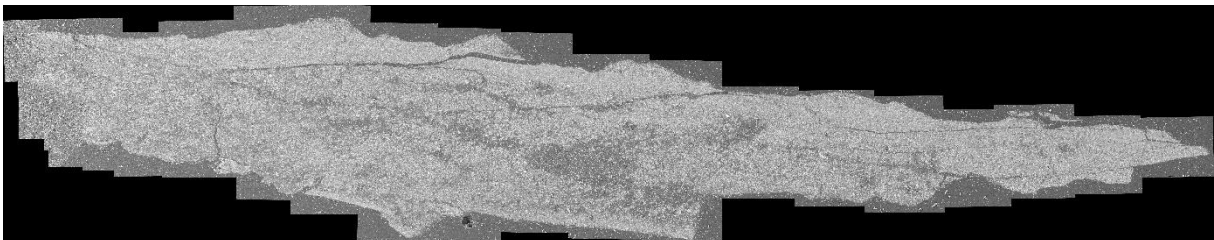


Figure 5.24: Cross section of sample wk271-1900 experiment U676 made by SEM. Scale vertical side is 1.5 mm.

Sample wk264-1850 is a very thin sample (0.5 mm). while the thickness of the sample was 1.45 mm (figure 5.25). The sample shows a thin band in the middle of the sample with coarse grains (figure 5.26). Both edges have bands with a small grain size. The coarser part in the middle seems to have more open pore spaces than the bands at the edges of the sample. The sample displays R_1 and Y fracture. The sense of shear is sinistral (figure 5.25). There are also R_2 fractures visible. These fractures stop where the coarser grains with more pore space begin (Figure 6.18)

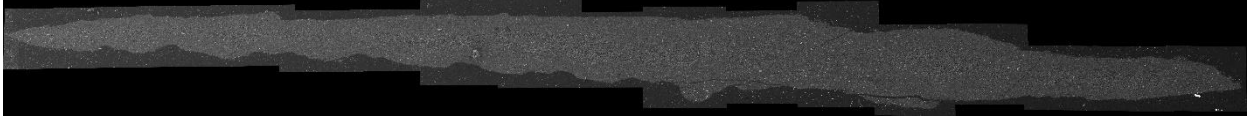


Figure 5.25: Cross section of sample wk264-1850 experiment U670 made by SEM. Scale vertical side is 1 mm.

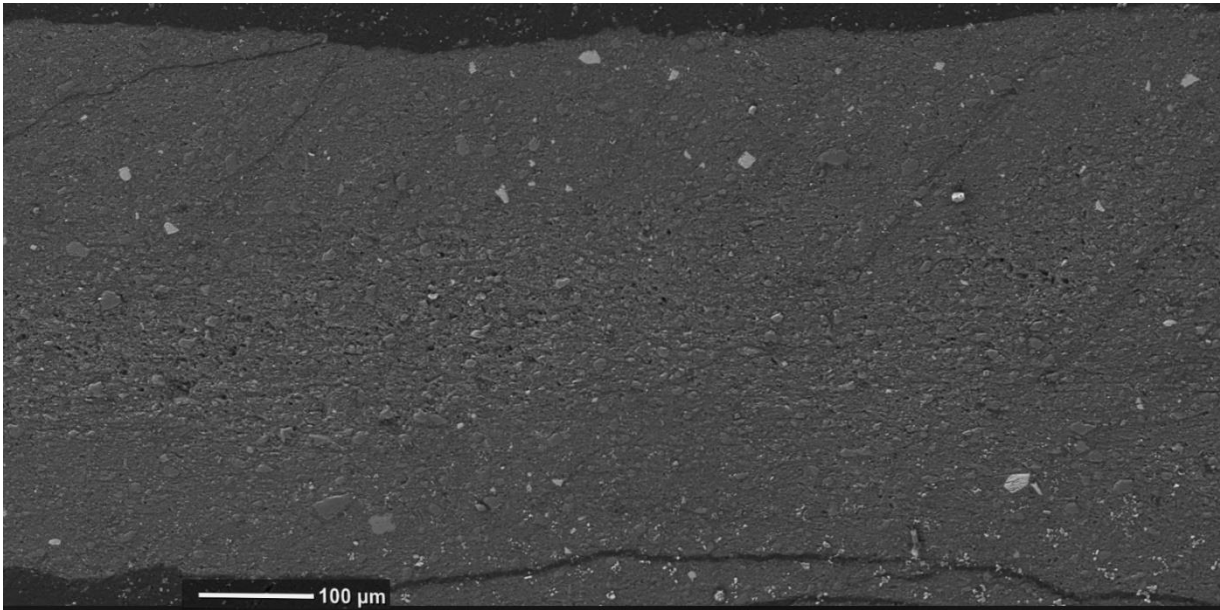


Figure 5.26: wk264-1850 with the thin coarse grained band in the middle. Scale vertical side is 0.5 mm.

Sample wk404-1922.5 seems to have a band in the middle of the sample that comprises more holes (figure 5.27). The grains of the band are coarse and have the same grain size as the surrounding grains. The sample is 1 mm thick. At the upper edge of the sample is a thin band of 100 μm with a finer grain size. This thin band is most likely the same as observed in all the other cross sections. The sample contains large R_1 fractures that cross the whole sample. At the end of the R_1 , they change to smaller Y fractures. The R_1 fractures indicate a sinistral sense of shear. The grains in sample seem to have a preferred horizontal orientation.

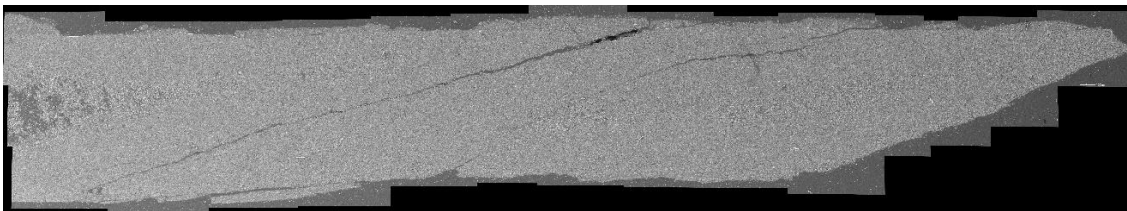


Figure 5.27: Cross section of sample wk404-1922.5 experiment U756 made by SEM. Scale vertical side is 1.3 mm.

7. Discussion

The variability of μ

In previous studies, volcanic rocks were investigated for their mechanical and physical properties. Some studies made attempts to link the effect of alteration to the mechanical properties of rocks. To my knowledge, no studies so far have investigated the frictional properties of hydrothermal altered volcanic rocks nor the effects of alteration on the frictional properties of rocks.

Mielke et al. (2015) and Wyring et al. (2014) investigated the effects of alteration on volcanic rocks in TVZ. Wyring et al. (2014) made a comparison in mechanical and physical properties of hydrothermal altered rocks from different geothermal reservoirs in the TVZ. They discovered high uniaxial strengths of 16-211 MPa for deep lithologies 1100-3280 m and low uniaxial strengths for shallow lithologies of 2-75 MPa at depths of 70-670 m. In my study I did not find the same trend with depth for the frictional properties. Wyring et al. (2014) suggest that the most important factor for differences in strength is related to the primary rock type and that high temperature alterations lead to higher mean strengths. They compare ignimbrites from shallow and deep depths which shows that the strength almost increases by 50%, because of the precipitation of strong minerals at high temperatures. The minerals precipitated are mainly quartz and calcite with some illite, albite, chlorite, epidote and pyrite. The ignimbrites in this study are from the same depth as the samples from the deep lithologies. Only the tuff wk261-100 belongs to the shallow lithologies. Comparing the frictional strength derived in this study does not show an increase in strength with depth. The precipitated minerals at high temperatures are the same for both studies.

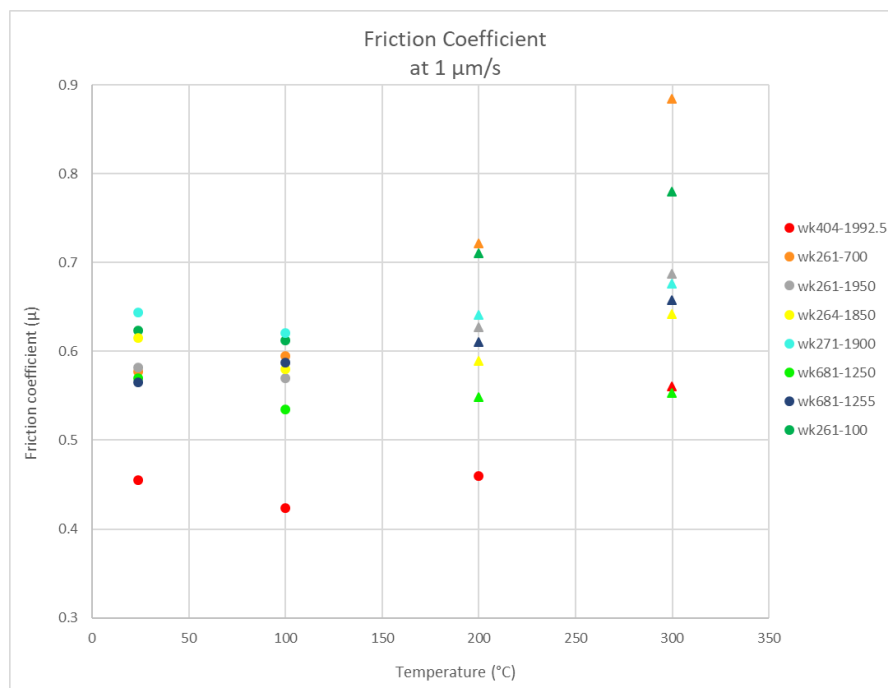


Figure 6.1: Friction coefficient at $1 \mu\text{m/s}$. The friction coefficients with a circle are obtained from steady state sliding and with a triangle from stick-slips.

The friction coefficient is plotted for different temperatures during sliding at $1 \mu\text{m/s}$ in figure 6.1. There is one sample significant different from the others, namely wk404-1922.5, when comparing the friction coefficients of the varying samples. This ignimbrite was drilled at 1922.5 m in the south of the geothermal field and has a friction coefficient of 0.4-0.5 at room temperature, while the other samples have a friction coefficient between 0.55 and 0.65. This difference in friction exists under all the

temperature conditions. It is not possible to explain the lower friction of wk404-1992.5 by the mineral composition. However, the sample was the only one drilled in the south of the Wairakei geothermal field, while the other samples were drilled in the northwest of the field. This indicates a difference in composition that is region bounded, but the compositional difference still has to be solved by further studies. The main trend for all the lithologies is an increase in friction with temperature, see figure 6.2. The friction of the two tuffs samples increases significant more than the other samples at 200 and 300 °C, namely to a friction coefficient around 0.7-0.9. The two tuff samples contain smectite minerals, which are unstable at higher temperatures, e.g. montmorillonite is stable until 140 °C. The disappearance of the clay minerals could strengthen the gouge. Clay minerals have normally low friction coefficients, see figure 6.8. The rhyolite lava develops quite similar as the majority of the ignimbrite samples, having a friction value of 0.58 at room temperature, which is increases with increasing temperature till 0.68 at 300 °C.

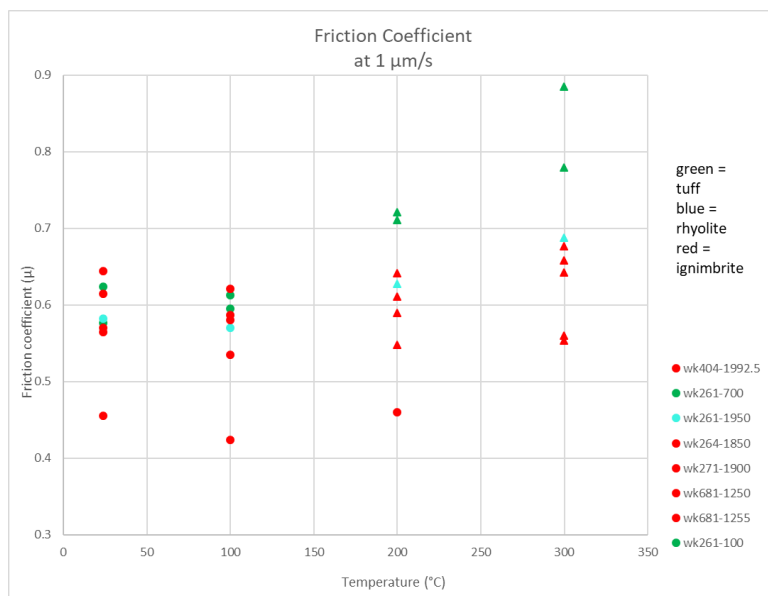


Figure 6.2: The friction coefficient at 1 μm/s loading velocity, classified by lithology.

Many experiments have been executed for investigating the frictional properties of fault gouges. Granite fault gouges are closest to the chemical composition of rhyolitic volcanic rocks. Previous tests (Blanpied et al., 1991; 1995) on Westerly granite fault gouges show friction values of 0.65-0.7 at room temperature (figure 7.3), which are slightly higher friction coefficients than the rhyolitic rocks. The applied conditions were, a confining pressure of 400 MPa and pore pressure of 100 MPa. Granite is almost completely crystallized, while rhyolitic volcanic rocks are not. Bonds in crystals are stronger than the bonds in volcanic glass shards which could explain the higher friction coefficient of granite compared to ignimbrite. Blanpied et al. (1991; 1995) found for temperatures above 300 °C a decrease in strength with increasing temperature and a strongly varying strength with slip velocity. I did not observe a decreasing strength between 200 and 300 °C for the tested volcanic rocks of the Wairakei geothermal field. Blanpied et al. (1995) showed only velocity weakening for wet granites between 90 and 360 °C under the applied loading conditions, whereas velocity weakening was already observed at room temperature in my study.

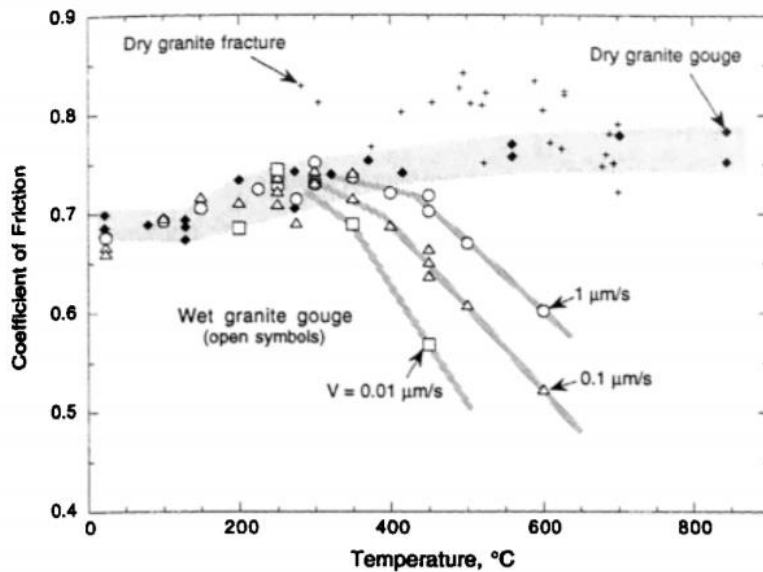


Figure 6.3: The friction coefficient versus the temperature for wet granite gouges at 400 MPa and 100 MPa pore fluid pressure at different sliding velocities, shown by the open symbols. Data from dry friction tests at 370 to 460 MPa is shown as well by the closed circles (Blanpied, 1995).

Mitchell et al. (2016) repeated frictional tests on Westerly granite in the same temperature range as Blanpied et al (1991). They used a direct shear apparatus. The experiments on the direct shear apparatus were at a normal stress of 30 MPa, pore fluid pressure of 0.7 MPa and larger slip distances than triaxial tests which makes the conditions of the experiments more comparable to my tests executed on the ring shear apparatus. Mitchell et al. (2016) shows for dry and hydrated conditions unstable slip for Westerly granite up to 600 °C. This is consistent with the negative (a-b) values up to 300 °C that were found in my study.

The effect of welding on μ

Pyroclastic rocks such as tuffs and ignimbrites can undergo different degrees of welding under formation. When they are deposited they are very hot. This heat can weld together the glass shards and pumice fragments. Their contacts adhere and compacts the rock. It is expected that welded ignimbrites have stronger frictional properties, because their fragments are welded together. The non-welded ignimbrite wk271-1900 and welded-ignimbrite wk264-1850 were compared. The non-welded ignimbrite has slightly higher friction coefficients than the welded ignimbrite. Based on this study conducted on limited cutting samples, the effect of welding on friction is probably negligible compared with the other effects. I expect that the effect of welding has been nullified during crushing of the grains for the preparation of the gouges. The crushing of the grains probably separates the welded grains.

The effects of temperature on μ

Temperature influences the behaviour of sliding, with stick-slip behaviour observed for most samples $\geq 200^\circ\text{C}$. An increase in temperature causes a brittle-plastic transition. The temperature increase causes at a certain moment "stickiness" of the grains, which is the creep at the asperity tips which strengthens the material (Mitchell et al., 2013). This can be seen as welding of the contacts. Another process that

could cause the gouge to stick more is pressure solution. Pressure solution is active under wet conditions and increases the area of contact between the grains. Pressure solution is active at higher temperatures (Renard et al., 1997; Niemeijer et al., 2008).

The change in friction coefficient at a sliding rate of 1 $\mu\text{m/s}$ during steady state sliding highlights the dependency of friction on temperature (figure 6.1). The friction coefficient increases with temperature. However the peak values in friction are taken for the stick-slips which makes them higher than their average. The tuff samples (wk261-100 and wk261-700) have the highest increase in friction with temperature. The ignimbrite samples wk271-1900 and wk681-1250 display a friction coefficient that stays roughly the same with an increase in temperature. However, they are not insusceptible for temperature, because they have a strong stick-slip pattern at 200 and 300 $^{\circ}\text{C}$. The other ignimbrite samples and rhyolite lava show an increase in friction with temperature. All samples show a stick-slip pattern at low slip velocities at 200 $^{\circ}\text{C}$ and almost all sliding velocities at 300 $^{\circ}\text{C}$ except the weak core sample wk404-1922.5. The stick-slips at 300 $^{\circ}\text{C}$ have a higher frictional peak than at 200 $^{\circ}\text{C}$. This is because of the thermally activated processes that strengthen the contacts during the stick phase. This also makes the stick phases to take longer at 300 $^{\circ}\text{C}$. The ignimbrite sample wk404-1922.5 does not slide through stick-slips at 200 $^{\circ}\text{C}$, which is deviating from all the other samples. Besides, this samples has a significant lower friction in comparison with the other samples. So there could be a correlation between its low friction coefficient and its sliding behaviour at 200 $^{\circ}\text{C}$. The material of wk404-1922.5 probably contains a weak substance that is less sensitive to thermal processes. The friction values at room temperature and 100 $^{\circ}\text{C}$ are almost the same, but they are slightly lower at 100 $^{\circ}\text{C}$.

The effects of velocity on μ

Faults are considered to be velocity weakening for $(a-b)<0$ and velocity strengthening for $(a-b)>0$. For $(a-b)=0$, it is velocity neutral. Periodic instabilities or stick-slips are assumed in faults when they display velocity weakening. Stable sliding or aseismic slip occurs under velocity strengthening. The deformation processes that are assumed to take place in fault gouge are dependent on velocity. Three deformation regimes have been indicated by Niemeijer and Spiers (2007; figure 6.4). They deduced for low shear strain rates a viscous or frictional-viscous flow with non-dilatant grain boundary sliding with a transition at higher strain rates to frictional granular flow with dilatation balanced by compaction creep. During the highest shear strain rate frictional granular flow at critical state is dominant. The shear strain rate is proportional to the shear velocity. However there is some localization of strain, which causes small variation in strain rate due to changes in thickness of the localized shear band.

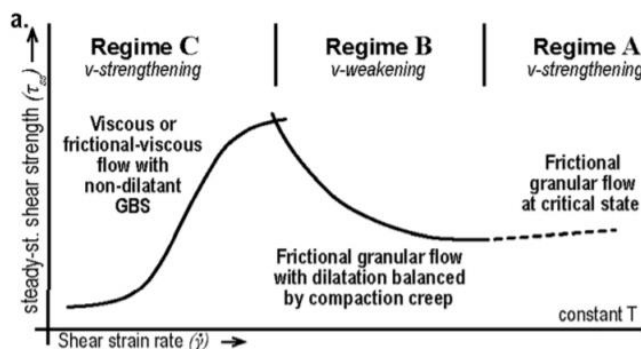


Figure 6.4: Model of the three regimes depending on steady state shear strength and shear strain rate (Verberne et al., 2015).

The effect of velocity on the frictional coefficient is a lowering of the friction with an increase in velocity. This is the general trend in all the samples at all temperatures. For example sample wk261-100 the friction is at 1 $\mu\text{m/s}$ 0.63 and at 100 $\mu\text{m/s}$ 0.57 at room temperature. The (a-b) values in this study are for all the samples negative from room temperature till 300 °C. They do vary in value. They have less negative values at room temperature and 100 °C compared to 200 and 300 °C, indicating a lower velocity weakening. They all fall in the seismogenic zone and have the potential for seismic nucleation, because the samples show velocity weakening. A change from stick-slip to steady sliding is observable with an increase in velocity at 200 °C. The explanation for this behaviour is that by an increase in velocity the frictional granular flow becomes more dominant and apparently determines the sliding behaviour. At low temperatures 24 and 100 °C the sliding behaviour is frictional granular flow and is way more dominant than compaction creep resulting in steady state flow under the applied shear rates in the test. At 300 °C the competition between frictional granular flow which causes dilation and compaction creep is more intense resulting in sliding through stick-slips.

It is questionable to determine the (a-b) for the stick-slips by taking their peak values. The differences in peak values between the velocity steps cause large negative (a-b) values as for example in sample wk261-700. The stick-slips decrease in size with increasing velocity. The recurrence interval of the stick-slips increases with decreasing velocity. The stick-slips have longer hold periods during lower velocities and so more time to re-strengthen. This causes a higher friction for failure of the stick period. This is presented in figure 6.5, where the recurrence time of the stick-slip is plotted against the friction peak for varying velocities.

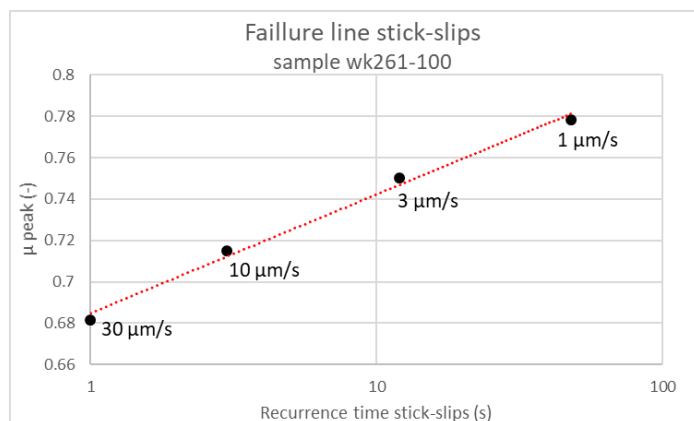


Figure 6.5: Schematic diagram for the recurrence interval of stick-slips plotted against the frictional peak. The red line is the failure line for the stick-slips.

At 300 °C are obtained positive (a-b) values during stick-slips for some samples such as wk264-1850. Positive (a-b) values indicate velocity strengthening which is not possible during stick-slips. The positive (a-b) is derived because it is based on the peak in friction. When the maximum friction is plotted against the minimum friction, it is visible that the difference in friction between quick recurrence intervals (high sliding velocities) is less than at long recurrence intervals (figure 6.6). Plotting the difference between maximum and minimum friction against the recurrence time for varying velocities (figure 6.7) shows that the friction decreases with velocity. This means that the obtained positive values for (a-b) are incorrect during stick-slips.

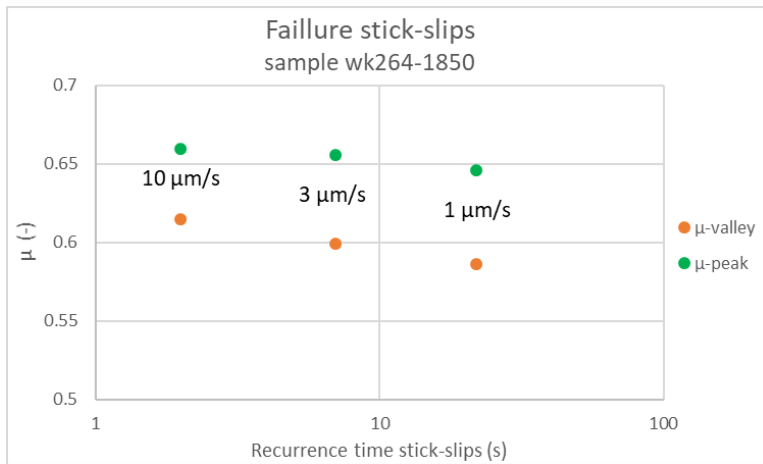


Figure 6.6: The plotted maximum and minimum friction during a stick-slip for different velocities.

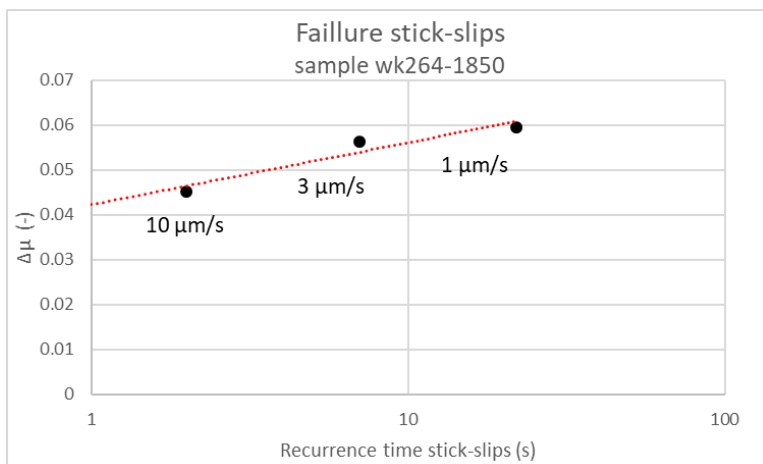


Figure 6.7: The $\Delta\mu$ which is the difference between μ_{max} and μ_{min} plotted against the recurrence interval of stick-slips.

Core versus cuttings

A comparison between cores and cuttings is necessary to determine whether cuttings are suitable to represent the frictional properties of reservoir rocks. Cuttings are brought to the surface by the drill fluid. The drill fluid can contaminate the cuttings or subtract substances. The cuttings are mixed on the way back up, which gives a range in the original depth of the cuttings. Naked eye observations showed that sample wk261-100 was contaminated with organic matter (twigs, wood pieces) and other cuttings samples were contaminated with plastic pieces. The cuttings contaminated with plastic were not used in this study. I tried to remove the contamination, but it is possible that there is contamination invisible to the eye. The organic matter is removed successfully from the cuttings, because it was not visible in the thermogravimetric analysis.

The core sample wk681-1255 and cuttings sample wk681-1250 have been compared by tests on their composition and their frictional properties. They both originate from the same well and their depths deviate a few meters. Sample wk404-1922.5 is another core sample that is used as a comparison with the cuttings of sample wk264-1850. They both are from the Stockyard Ignimbrite formation. However, wk404-1922.5 is from a drill hole in Karapiti South and wk264-1850 from a drill hole in the Poihipi West area.

The frictional tests show some discordance in value between the cores and cuttings. The wk681-1255 core sample has a friction of 0.05 higher than its counterpart at room temperature. The opposite is observable for core sample wk404-1922.5 that has a friction of 0.05-0.07 lower at room temperature. With increasing temperature wk404-1922.5 and wk264-1850 develop different. Wk681-1250 and wk681-1255 also develop different, but less significant. The friction of core sample wk681-1255 gets about 0.05 higher at 300 °C. The difference in friction between wk681-1250 and wk681-1255 can be explained by the fact that cuttings are taken over a broader range in the drill hole, which could lead to some minor variations in the frictional behaviour. However the difference in friction is very small and probably the results of minor differences in conditions during the two experiments. Core sample wk404-1922.5 differs from all the sample, which is probably due to its location in the south of the Wairakei geothermal field. All the other samples are drilled in the north of the field.

The TGA analyses of the cores don't show the presence of kaolinite, while the cuttings seem to have kaolinite. Kaolinite does occur at depths of 225-450 m at locations near and in the Wairakei geothermal field (Simpson and Rae, 2018). Deeper in the reservoir at the depths of the used sample prevail neutral to slight alkaline water conditions (Piragno, 2009). Drill fluid could have added kaolinite, but they don't contain this clay mineral which makes it less reliable. The drill fluid contained only bentonite and caustic soda. Kaolinite is a sheet structured mineral. It has a high frictional coefficient compared to other clay minerals (Morrow et al., 2000; Figure 6.8). The friction coefficient is higher for kaolinite than the observed friction in sample wk404-1922.5. Kaolinite probably does not have much influence on the frictional property of cuttings. Kaolinite is not a specific strong or weak mineral and the quantities present in the cuttings are estimated at only 0.5% mass percentage.

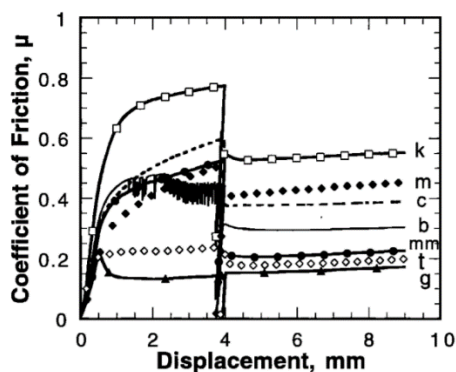


Figure 6.8: A sliding experiment at 0.5 $\mu\text{m/s}$ at room temperature. At 4 mm displacement is water added to the samples. The fault gouges contains kaolinite (k), muscovite (m), chlorite (c), montmorillonite (mm), talc (t) and graphite (g) (from Morrow et al., 2000).

The differences in mass loss during the TGA analysis of the samples of drill hole wk681 is 7.3% for the core and 2.3 % for the cuttings. The deviation in mass loss is caused by the higher loss in calcite for the core sample. Thus the core sampled contained more calcite than the cuttings. Calcite is a strong mineral with a friction coefficient of 0.7 undersaturated condition at room temperature (Morrow et al., 2000). Calcite could cause a difference in strength between wk681-1250 and wk681-1255. If the drill fluid was acid it could have dissolved a part of the calcite in the cuttings. However the drill fluid had a pH of 8.5-9. Rock interstices are usually filled with calcite, quartz and zeolites (Steiner, 1968). A higher density of interstices could explain the higher mass percentage in calcite.

In conclusion on cores versus cuttings: there is some contamination of the cuttings such as probably kaolinite, but the effects are negligible. The similarities in frictional behaviour between the cuttings and the cores allows to make geological interpretations on all samples, keeping in mind the limitations due to the sampling.

Static friction (healing)

Healing is the strengthening of the fault gouge during a hold in movement. It displays the growth in static friction. Healing is a combination of increase in packing density, contact strengthening and contact area increase. (Marone, 1998; Niemeijer et al., 2008). The healing rate of the fault gouge can be used to extrapolate to longer duration because of its log linear relationship. In figure 6.9 the increase in static friction over a year is plotted for sample wk404-1922.5. Faults in the reservoir probably only slip when there is a micro-seismic event. For larger earthquakes, with a magnitude of M 2 or M 3, the recurrence interval might be 1 year, that is why the healing rate is extrapolated over a year. The seismic slip velocity reaches during a seismic event about 1 m/s, but the final slip velocity before the slip stops will be much lower, that is why the starting position is taken at 1 $\mu\text{m/s}$. Hence the lowest sliding rate approximates the best the initial static friction.

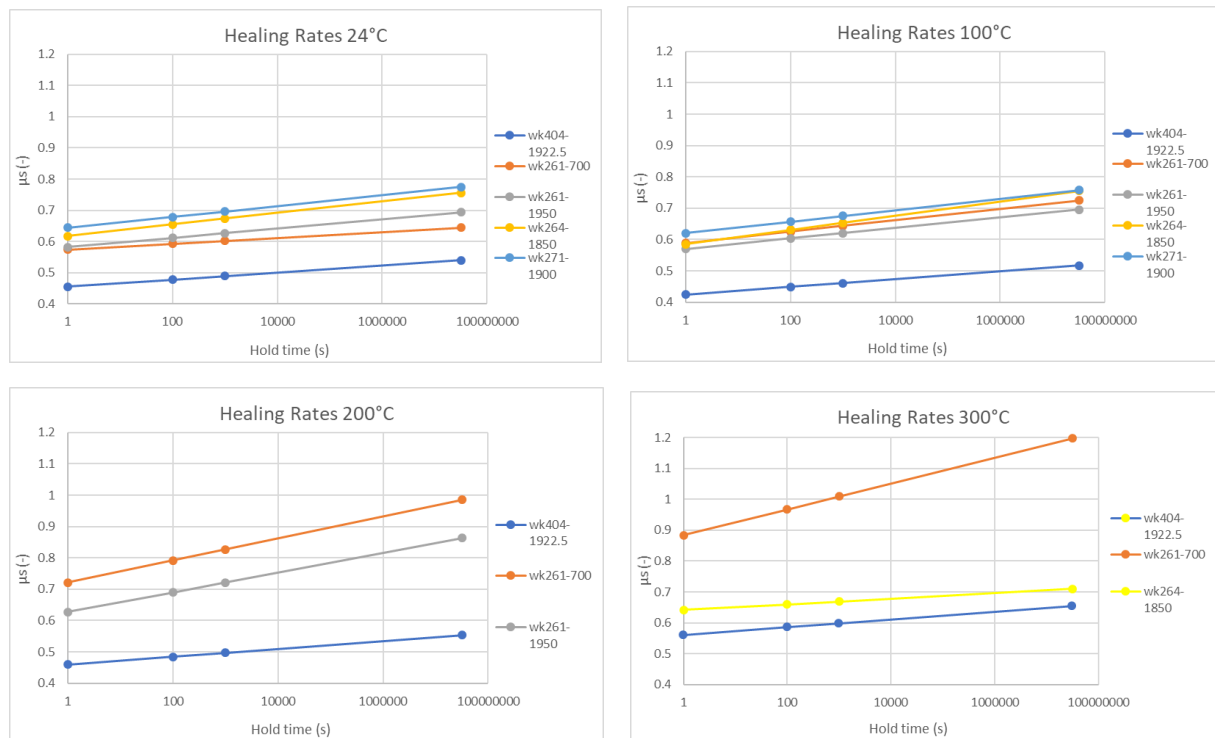


Figure 6.9: The development of the static friction of the fault over one year for the samples at four temperature conditions from 24 to 300 °C.

The friction coefficient during steady state sliding is picked at the end of the velocity step. The friction coefficient during stick-slip is harder to determine. The friction coefficient for shearing at 1 $\mu\text{m/s}$ with stick-slips is picked at the peak of the stick-slips. The healing rate is expected to be higher at higher temperature, because healing processes are thermally activated. This is observable for sample wk261-700 which has an increase in friction of 0.3 in one year at 300 °C, while the healing rate at 24 °C is only 0.05 per year.

There are no specific trends identifiable for specific lithologies. However, sample wk404-1922.5 has lower healing rates than the other samples. Especially at 200 °C, but this depends on the way the healing rate is derived. The healing rate is derived from steady state sliding instead of stick-slip, which gave lower healing rates. This creates an uncertainty in all the obtained healing rates. The healing rate at high temperatures which are obtained from stick-slips should be lower.

The effects of alteration on fault strength

Hot fluids alter rocks by dissolution and precipitation of minerals. This leads to varying rock composition vertically and laterally in a geothermal reservoir (Pirajno, 2009). Hydrothermal alteration is determined by rank and intensity. Rank is the mineral assemblage and intensity is the quantity of replacement of primary minerals by secondary minerals. The rank and intensity of alteration depends on primary lithology, pressure, temperature, composition of thermal fluids, duration of fluid-rock interaction and fluid phase (Frolova et al., 2010). Mielke et al. (2015) distinguished a smectite, argillic and propylitic alteration zones in three geothermal fields in the TVZ. These zones are characteristic for conventional geothermal systems (Robb, 2005). The smectite zone is located near the surface and only tens of meters deep due to low temperature alteration, followed by the argillic zone which comprises low to moderate temperature minerals (below 230 °C), mainly formed by interstratified illite-smectites (Robb, 2005). The propylitic zone has high temperature (200-300 °C) minerals such as chlorite, epidote and quartz, calcite and albite (Robb, 2005). The samples in this study have all undergone propylitic alteration except sample wk261-100, which belongs to the argillic zone.

Intensity of alteration is difficult to determine on the cutting samples. Normally the intensity of alteration is determined by optical microscopy. However, with use of sampled cuttings this is not possible. An effort was made by distinguishing them by the results of the TGA tests. The TGA test shows different quantities in mass loss for the samples. The samples with a propylitic alteration which don't contain calcite (wk271-1900, wk261-1950 and wk264-1850) have a significant lower loss in mass than those which do contain calcite. Using the mass loss from the TGA analyses as indicator for the degree in alteration will be based mostly on the loss in weight of calcite and zeolites. This indicates that the samples wk681-1250, wk681-1255, wk404-1922.5 and wk261-700 are more altered than the other samples. However, calcite also precipitates in interstices. An increase in calcite will be present, when the sample contained more parts with interstices and is not directly an indication for the intensity of alteration.

Albite is the alteration product of andesine and the quantity of albite present in the samples suggest highly altered rocks. However it is very hard to distinguish with the XRD between albite and andesine and impossible to tell the ratio between albite and andesine. So those samples could still be barely altered. A profound study on thin sections of core samples would be necessary to elucidate the alteration intensity.

It is not possible to elucidate the intensity of alteration on the samples. Only a comparison in rank can be made, which differentiates wk261-100 with an argillic alteration from the rest of the samples with a propylitic alteration. Wk261-100 is a tuff like wk261-700. The other samples are ignimbrites and rhyolitic lava and can't be compared due to their differences in lithology. Wk261-700 shows the same frictional development in pattern related to temperature and velocity stepping. The frictional coefficient of wk261-100 is significant lower at 300 °C, namely 0.1. Wk261-700 contains a significant amount of zeolites such as wairakite, which are maybe the reason for its lower friction coefficient, because it is the most significant difference in content between the two rocks. Expected would be that the friction of wk261-100 would increase more than wk261-700, because the weaker clay minerals such as montmorillonite disappear above 200 °C. It must be remarked that wk261-100 was contaminated with organic matter. However the contamination of organic matter was not noticeable in the TGA analyses.

Implications

Velocity weakening was observed for all the samples at 300 °C. The applied conditions of 50 MPa effective normal stress and 20 MPa pore fluid pressure correspond to a depth of around 2-2.5 km. At this depth, the temperature is expected to be around 300 °C (Milloy et al., 2014). Under those implied in situ conditions the faults in rhyolitic volcanic rocks (tuff, lava and ignimbrites) have the potential for seismic nucleation and permeability enhancement in the Wairakei geothermal field. The experiments at 24, 100 and 200 °C show also velocity weakening for all the samples. The applied stresses and pressures in the experiment are too high for the conditions under which those temperatures prevail in the Wairakei geothermal reservoir. However, Mitchell et al. (2016) showed for granite rocks that the normal stress does not have significantly changes the rate and state friction below 400 °C. I assume that the higher used effective normal stress than the in situ stress, won't change the state of velocity weakening of the material at the temperatures of 24, 100 and 200 °C. This means that in the Wairakei geothermal field the rhyolitic volcanic rocks from a depth of 700 to 2500 m all have the potential for seismic nucleation, and hence conducting fluid along reactivated critically-stressed fractures, which corresponds to the observed depths of micro-seismicity in the geothermal field (Sepulveda et al., 2013).

The deformation processes that determine the sliding behaviour of the fault gouge are dependent on temperature and velocity. They have been classified in three regimes based on the Niemeijer-Spiers model for steady state sliding (Niemeijer and Spiers, 2007). Those regimes have been observed for many lithologies such as halite, gabbro, granite, calcite and phyllosilicate-rich rocks (Verberne et al., 2015) and occur probably as well in rhyolitic volcanic rocks. Figure 7.3 shows that these regimes depend on strain rate. An increase in temperature shift this graph to the right. Regime A occurs at low temperatures, deforms brittle by critical state granular flow and results in velocity strengthening frictional behaviour. Regime C occurs at high temperatures, deforms plastic and results in velocity strengthening. Regime B is the transition between regime A and C and results velocity weakening. In regime B are the deforming processes a competition between frictional granular flow which dilates the material and time-dependent compaction creep that is thermally activated. The processes operating in the tests on the samples at 24 and 100 °C are expected to lie close the transition between regime A and B due to its low friction. That velocity strengthening is not observed at 24 °C which could be the result of the mineral content compared to volcanic glass. Rhyolitic volcanic rocks have a low content of strong minerals which normally strengthen the gouge and a high content of volcanic glass which probably have a low cohesive strength, but still a strong material (Morrow et al., 2000). The behaviour at 200 and 300 °C implies that the thermally activated processes, which are strengthening the material, became the more dominant in deforming the gouge compared to frictional granular flow. This also explains the higher healing rates at 200 and 300 °C.

The microstructures observed were taken from the leftovers at the end of the velocity stepping experiments at 300 °C. They show R_1 and Y shears and compaction bands near the boundaries. The grains are larger in the middle and less compacted. It suggests that frictional granular flow is dominant in the middle of the fault gouge and compaction creep near its boundaries. This results in localization of shear, that explains the spontaneous behaviour of stick-slips at 200 °C (e.g. wk681-1250).

The ignimbrite in one well in Karapiti South area is weaker than all the other samples from the Poihipi West area. The wk404-1922.5 has lower friction coefficients and lower healing rates than all the other samples. This means that this rock is more prone for seismic nucleation from changes in the effective stress state. It is still very debatable because this inference is based on only one sample for the region.

Further work on the frictional properties of the different rocks in the Wairakei geothermal field is advised for a complete analysis of the seismogenic potential of the geothermal field and in which formation they will nucleate. Future studies should examine cores samples to distinguish alteration and investigate the effect of mineral percentages and strength of volcanic glass for a complete analysis.

7. Conclusion

This study investigated the effect of alteration and lithologies on the frictional properties of the silicic volcanic rocks hosting the Wairakei geothermal reservoir, and their potential for seismic nucleation. Cores and cuttings have been sampled from drill holes in the Wairakei geothermal field, New Zealand, where reservoir temperature is 200 °C at 450 m and 300 °C at 2 km depth. They originate from depths varying from 100 m to 2 km. The samples consist of tuff's, ignimbrites and rhyolite lava. They have been tested by velocity stepping experiments and slide-hold-slide experiments on simulated fine-grained gouge. The experiments were conducted under the in situ conditions of 50 MPa effective normal stress and 20 MPa pore fluid pressure corresponding to reservoir conditions at 2-2.5 km depth, and temperatures varying from 24 to 300 °C. The applied loading rate varied from 10^{-6} to 10^{-4} m/s.

The friction coefficient of rhyolitic rocks varied for most samples between 0.55 and 0.65 at room temperature. The friction coefficient is the same for rhyolitic lava and ignimbrite under all conditions. The friction of the tuff samples is significant higher at 200 and 300 °C. An increase in temperature causes an increase in average friction. At 24 and 100 °C the material deformed by steady state sliding which changed into mainly stick-slip behaviour at 200 and 300 °C. An increase in velocity showed negative (a-b) values indicating velocity weakening. The velocity weakening observed at all temperatures indicates that the rocks are unstable under the applied in situ conditions and have the potential for seismic nucleation.

The ignimbrite sample located Karapiti South area with a friction coefficient between 0.4-0.5 is significant weaker than all the other samples from the Poihipi West area. The cause for this low friction coefficient has not been found.

The controlling effect on velocity weakening is assumed to be a competition between frictional granular flow which dilates the material and compaction creep that is thermally activated. The microstructures observed in the fault gouge at 300 °C show localized R_1 and Y shears and have shear bands near the boundaries.

Based on assessment by the naked eye, frictional tests, XRD analysis and TGA analysis, cuttings appear to be slightly contaminated by kaolinite and show a loss in calcite compared to core equivalents. Visual observations showed that some sampled cuttings were contaminated by organic matter (pieces of wood) and plastic. However, the behaviour of cores and cuttings appeared to be the same during the frictional test and the minor contamination does not influence the obtained frictional values.

The effects of welding on the frictional properties of ignimbrites was investigated. The non-welded ignimbrite sample had a higher friction coefficient than the welded ignimbrite samples. Welding is expected to be of minor importance on friction, probably because the rock loses the strength of welded grains during crushing of the grains for the preparation of the gouges.

The healing rates of the fault gouges are larger at higher temperatures. The weakest ignimbrite sample re-strengthens in one year from 0.46 to 0.54 at 24 °C. The static friction of the tuff sample from 700 m depth recovers at 24 °C by 0.07 friction units and at 300 °C by 0.31 over a one year duration.

This study did not succeed to identify the effect of alteration mineralogy (propylitic or argillic) on the frictional properties of volcanic rocks, which may be due to the limited amount of argillic samples. mineral content and quantity are expected to be an important factor on controlling the friction and need further investigation.

Acknowledgements

First of all I want to thank my supervisors Andre Niemeijer and Cécile Massiot. Andre had always time for questions and responds incredibly fast to emails. He guided me very well through the experiments and the interpretation of the results. Thanks to him I could finish my thesis in time. I want to thank Cécile and her team in New Zealand for sending me the samples of the Wairakei Geothermal Field. She gave me very useful feedback and helped in structuring the report. Cécile was supported by GNS Science's *Geothermal Resources of New Zealand* and *New Zealand Geothermal Future* research programmes, funding of which was provided by the Government of New Zealand. Thanks to Contact Energy Ltd. for providing the samples, allowing publication of this study and useful comments of Fabian Sepulveda. I want to thank the people that work in HTP lab in Utrecht that helped me as well.

References

- Barton, C. A., Zoback, M. D., & Moos, D. (1995). Fluid flow along potentially active faults in crystalline rock. *Geology*, 23(8), 683–686.
- Beeler, N. M., Simpson, R. W., Hickman, S. H., & Lockner, D. A. (2000). Pore fluid pressure, apparent friction, and Coulomb failure. *Journal of Geophysical Research: Solid Earth*, 105(B11), 25533-25542.
- Bertrand, E. A., Caldwell, T. G., Hill, G. J., Wallin, E. L., Bennie, S. L., Cozens, N., ... & Wameyo, P. (2012). Magnetotelluric imaging of upper-crustal convection plumes beneath the Taupo Volcanic Zone, New Zealand. *Geophysical Research Letters*, 39(2).
- Bibby, H. M., Caldwell, T. G., Davey, F. J., & Webb, T. H. (1995). Geophysical evidence on the structure of the Taupo Volcanic Zone and its hydrothermal circulation. *Journal of volcanology and geothermal research*, 68(1-3), 29-58.
- Bignall, G., Milicich, S. D., Ramirez, L. E., Rosenberg, M. D., Kilgour, G. N., & Rae, A. J. (2010, April). Geology of the wairakei-Tauhara geothermal system, New Zealand. In *Proceedings Worlds Geothermal Congress* (pp. 25-30).
- Blanpied, M. L., Lockner, D. A., & Byerlee, J. D. (1991). Fault stability inferred from granite sliding experiments at hydrothermal conditions. *Geophysical Research Letters*, 18(4), 609-612.
- Blanpied, M. L., Lockner, D. A., & Byerlee, J. D. (1995). Frictional slip of granite at hydrothermal conditions. *Journal of Geophysical Research: Solid Earth*, 100(B7), 13045-13064.
- Blanpied, M. L., Marone, C. J., Lockner, D. A., Byerlee, J. D., & King, D. P. (1998). Quantitative measure of the variation in fault rheology due to fluid-rock interactions. *Journal of Geophysical Research: Solid Earth*, 103(B5), 9691-9712.
- Bolton, R. S. (1970). The behaviour of the Wairakei geothermal field during exploitation. *Geothermics*, 2, 1426-1439.
- Browne, P. R. L., & Ellis, A. J. (1970). The Ohaki-Broadlands hydrothermal area, New Zealand; mineralogy and related geochemistry. *American Journal of Science*, 269(2), 97-131.
- Bryan, C. J., Sherburn, S., Bibby, H. M., Bannister, S. C., & Hurst, A. W. (1999). Shallow seismicity of the central Taupo Volcanic Zone, New Zealand: its distribution and nature. *New Zealand Journal of Geology and Geophysics*, 42(4), 533-542.
- Chen, J., Niemeijer, A. R., & Spiers, C. J. (2017). Microphysically Derived Expressions for Rate-and-State Friction Parameters, a , b , and D_c . *Journal of Geophysical Research: Solid Earth*.
- Clayton, R. N., & Steiner, A. (1975). Oxygen isotope studies of the geothermal system at Wairakei, New Zealand. *Geochimica et Cosmochimica Acta*, 39(8), 1179-1186.
- Contact Energy, 2017. Full year report 2017. <https://contact.co.nz/aboutus/media-centre>
- Den Hartog, S. A. M., Niemeijer, A. R., & Spiers, C. J. (2012). New constraints on megathrust slip stability under subduction zone P–T conditions. *Earth and Planetary Science Letters*, 353, 240-252.
- Dieterich, J. H. (1972). Time-dependent friction in rocks. *Journal of Geophysical Research*, 77(20), 3690-3697.
- Dieterich, J. H. (1979). Modeling of rock friction: 1. Experimental results and constitutive equations. *Journal of Geophysical Research: Solid Earth*, 84(B5), 2161-2168.
- Electricity Authority, 2016. Electricity in New Zealand. <https://www.ea.govt.nz/dmsdocument/20410>
- Ellsworth, W. L. (2013). Injection-induced earthquakes. *Science*, 341(6142), 1225942.

- Frolova, J. V., Ladygin, V. M., & Rychagov, S. N. (2010, April). Petrophysical alteration of volcanic rocks in hydrothermal systems of the Kuril-Kamchatka Island Arc. In *Proc. World Geochemical Congress, Bali*.
- Heap, M. J., Lavallée, Y., Petrakova, L., Baud, P., Reuschle, T., Varley, N. R., & Dingwell, D. B. (2014). Microstructural controls on the physical and mechanical properties of edifice-forming andesites at Volcán de Colima, Mexico. *Journal of Geophysical Research: Solid Earth*, *119*(4), 2925-2963.
- Houghton, B. F., Wilson, C. J. N., McWilliams, M. O., Lanphere, M. A., Weaver, S. D., Briggs, R. M., & Pringle, M. S. (1995). Chronology and dynamics of a large silicic magmatic system: Central Taupo Volcanic Zone, New Zealand. *Geology*, *23*(1), 13-16.
- Hunt, T. M., Bromley, C. J., Risk, G. F., Sherburn, S., & Soengkono, S. (2009). Geophysical investigations of the Wairakei Field. *Geothermics*, *38*(1), 85-97.
- Langridge, R. M., Ries, W. F., Litchfield, N. J., Villamor, P., Van Dissen, R. J., Barrell, D. J. A., ... & Lee, J. M. (2016). The New Zealand active faults database. *New Zealand Journal of Geology and Geophysics*, *59*(1), 86-96.
- Marone, C. (1998). Laboratory-derived friction laws and their application to seismic faulting. *Annual Review of Earth and Planetary Sciences*, *26*(1), 643-696.
- Massiot, C., McNamara, D. D., & Lewis, B. (2013). *Interpretive review of the acoustic borehole image logs acquired to date in the Wairakei-Tauhara Geothermal Field*. GNS Science.
- Massiot, C., McLean, K., McNamara, D.D., Sepulveda, F., Milicich, S.D., 2017. Discussion between a reservoir engineer and a geologist: permeability identification from completion test data and borehole image logs integration. *Proceedings 39th New Zealand Geothermal Workshop 22-24 November 2017 Rotorua, New Zealand*.
- McLaskey, G. C., Thomas, A. M., Glaser, S. D., & Nadeau, R. M. (2012). Fault healing promotes high-frequency earthquakes in laboratory experiments and on natural faults. *Nature*, *491*(7422), 101.
- McNamara, D. D., Bannister, S., Villamor, P., Sepúlveda, F., Milicich, S. D., Alcaraz, S., & Massiot, C. (2016). Exploring Structure and Stress from Depth to Surface in the Wairakei Geothermal Field, New Zealand. In *41st Workshop on Geothermal Reservoir Engineering Stanford University, Stanford, California*.
- Mielke, P., Nehler, M., Bignall, G., & Sass, I. (2015). Thermo-physical rock properties and the impact of advancing hydrothermal alteration—A case study from the Tauhara geothermal field, New Zealand. *Journal of Volcanology and Geothermal Research*, *301*, 14-28.
- Milicich, S. D. (2013). Aspects of the Chronology, Structure and Thermal History of the Kawerau Geothermal Field.
- Milloy, S. F., Newson, J., & Sepulveda, F. (2014). Geothermal Surface Features at Geysir Valley, Wairakei, New Zealand. In *38th Stanford Workshop on Geothermal Reservoir Engineering Proceedings*.
- Mitchell, E. K., Fialko, Y., & Brown, K. M. (2013). Temperature dependence of frictional healing of Westerly granite: Experimental observations and numerical simulations. *Geochemistry, Geophysics, Geosystems*, *14*(3), 567-582.
- Mitchell, E. K., Fialko, Y., & Brown, K. M. (2016). Velocity-weakening behavior of Westerly granite at temperature up to 600° C. *Journal of Geophysical Research: Solid Earth*, *121*(9), 6932-6946.
- Mizoguchi, K., Hirose, T., Shimamoto, T., & Fukuyama, E. (2007). Reconstruction of seismic faulting by high-velocity friction experiments: An example of the 1995 Kobe earthquake. *Geophysical Research Letters*, *34*(1).
- Morrow, C. A., Moore, D. E., & Lockner, D. A. (2000). The effect of mineral bond strength and adsorbed water on fault gouge frictional strength. *Geophysical research letters*, *27*(6), 815-818.
- Niemeijer, A. R., & Spiers, C. J. (2007). A microphysical model for strong velocity weakening in phyllosilicate-bearing fault gouges. *Journal of Geophysical Research: Solid Earth*, *112*(B10).

- Niemeijer, A., Marone, C., & Elsworth, D. (2008). Healing of simulated fault gouges aided by pressure solution: Results from rock analogue experiments. *Journal of Geophysical Research: Solid Earth*, 113(B4).
- Niemeijer, A. R., Spiers, C. J., & Peach, C. J. (2008). Frictional behaviour of simulated quartz fault gouges under hydrothermal conditions: Results from ultra-high strain rotary shear experiments. *Tectonophysics*, 460(1-4), 288-303.
- Pirajno, F. (2009). Hydrothermal processes associated with meteorite impacts. In *Hydrothermal Processes and Mineral Systems* (pp. 1097-1130). Springer, Dordrecht.
- Pola, A., Crosta, G., Fusi, N., Barberini, V., & Norini, G. (2012). Influence of alteration on physical properties of volcanic rocks. *Tectonophysics*, 566, 67-86.
- Pola, A., Crosta, G. B., Fusi, N., & Castellanza, R. (2014). General characterization of the mechanical behaviour of different volcanic rocks with respect to alteration. *Engineering Geology*, 169, 1-13.
- Renard, F., Ortoleva, P., & Gratier, J. P. (1997). Pressure solution in sandstones: influence of clays and dependence on temperature and stress. *Tectonophysics*, 280(3-4), 257-266.
- Risk, G. F. (1984). Electrical resistivity survey of the Wairakei geothermal field. In *Proc. 6th NZ Geothermal Workshop, Univ. Auckland, Nov. 1984* (pp. 123-128).
- Robb, L. (2004). *Introduction to ore-forming processes*. Blackwell publishing.
- Rosenberg, M. D., Bignall, G., & Rae, A. J. (2009). The geological framework of the Wairakei–Tauhara geothermal system, New Zealand. *Geothermics*, 38(1), 72-84.
- Rosenberg, M. D., Bignall, G., & Rae, A. J. (2009). The geological framework of the Wairakei–Tauhara geothermal system, New Zealand. *Geothermics*, 38(1), 72-84.
- Rowland, J. V., & Sibson, R. H. (2004). Structural controls on hydrothermal flow in a segmented rift system, Taupo Volcanic Zone, New Zealand. *Geofluids*, 4(4), 259-283.
- Ruina, A. (1983). Slip instability and state variable friction laws. *Journal of Geophysical Research: Solid Earth*, 88(B12), 10359-10370.
- Scholz, C. H., & Engelder, J. T. (1976, May). The role of asperity indentation and ploughing in rock friction—I: Asperity creep and stick-slip. In *International Journal of Rock Mechanics and Mining Sciences & Geomechanics Abstracts* (Vol. 13, No. 5, pp. 149-154). Pergamon.
- Sepulveda, F., Andrews, J., Alvarez, M., Montague, T., & Mannington, W. (2013). Overview of deep structure using microseismicity at Wairakei. In *35th New Zealand Geothermal Workshop: 2013 Proceedings*.
- Sepulveda, F., Andrews, J., Kim, J., Siega, C., & Milloy, S. F. (2015). Spatial-temporal Characteristics of Microseismicity (2009-2014) of the Wairakei Geothermal Field, New Zealand. In *Proceedings World Geothermal Congress 2015 Melbourne*.
- Scholz, C., Molnar, P., & Johnson, T. (1972). Detailed studies of frictional sliding of granite and implications for the earthquake mechanism. *Journal of geophysical research*, 77(32), 6392-6406.
- Scholz, C. H. (2002). *The mechanics of earthquakes and faulting*. Cambridge university press.
- Sherburn, S., Bromley, C., Bannister, S., Sewell, S., & Bourguignon, S. (2015). New Zealand geothermal induced seismicity: An overview. In *Proceedings of the World Geothermal Congress*.
- Simpson, M. P., & Rae, A. J. (2018). Short-wave infrared (SWIR) reflectance spectrometric characterisation of clays from geothermal systems of the Taupō Volcanic Zone, New Zealand. *Geothermics*, 73, 74-90.
- Smith, R., Sammonds, P. R., & Kilburn, C. R. (2009). Fracturing of volcanic systems: experimental insights into pre-eruptive conditions. *Earth and Planetary Science Letters*, 280(1-4), 211-219.

- Steiner, A. (1953). Hydrothermal rock alteration at Wairakei, New Zealand. *Economic geology*, 48(1), 1-13.
- Steiner, A. (1968). Clay minerals in hydrothermally altered rocks at Wairakei, New Zealand. *Clays and Clay Minerals*, 16(3), 193-213.
- Townend, J, and Zoback, M. D. "How faulting keeps the crust strong." *Geology* 28.5 (2000): 399-402.
- Utada, M. (2001). Zeolites in hydrothermally altered rocks. *Reviews in mineralogy and geochemistry*, 45(1), 305-322.
- Van den Bogert, P. A. J. (2015). Impact of various modelling options on the onset of fault slip and fault slip response using 2-dimensional finite-element modelling. *Restricted report No. SR, 15*.
- Van Thienen-Visser, K., & Breunese, J. N. (2015). Induced seismicity of the Groningen gas field: History and recent developments. *The Leading Edge*, 34(6), 664-671.
- Verberne, B. A., Niemeijer, A. R., De Bresser, J. H., & Spiers, C. J. (2015). Mechanical behavior and microstructure of simulated calcite fault gouge sheared at 20–600 C: Implications for natural faults in limestones. *Journal of Geophysical Research: Solid Earth*, 120(12), 8169-8196.
- Villamor, P., Berryman, K. R., Ellis, S. M., Schreurs, G., Wallace, L. M., Leonard, G. S., ... & Ries, W. F. (2017). Rapid Evolution of Subduction-Related Continental Intraarc Rifts: The Taupo Rift, New Zealand. *Tectonics*, 36(10), 2250-2272.
- Wilson, C. J. N., Houghton, B. F., McWilliams, M. O., Lanphere, M. A., Weaver, S. D., & Briggs, R. M. (1995). Volcanic and structural evolution of Taupo Volcanic Zone, New Zealand: a review. *Journal of volcanology and geothermal research*, 68(1-3), 1-28.
- Wilson, C. J. N., (2001). The 26.5 ka Oruanui eruption, New Zealand: an introduction and overview. *Journal of Volcanology and Geothermal Research* 112.1-4: 133-174.
- Wilson, C. J. N., & Rowland, J. V. (2016). The volcanic, magmatic and tectonic setting of the Taupo Volcanic Zone, New Zealand, reviewed from a geothermal perspective. *Geothermics*, 59, 168-187.
- Wyering, L. D., Villeneuve, M. C., Wallis, I. C., Siratovich, P. A., Kennedy, B. M., Gravley, D. M., & Cant, J. L. (2014). Mechanical and physical properties of hydrothermally altered rocks, Taupo Volcanic Zone, New Zealand. *Journal of Volcanology and Geothermal Research*, 288, 76-93.
- Wyering, L. D., Villeneuve, M. C., Kennedy, B. M., Gravley, D. M., & Siratovich, P. A. (2017). Using drilling and geological parameters to estimate rock strength in hydrothermally altered rock—A comparison of mechanical specific energy, R/NW/D chart and Alteration Strength Index. *Geothermics*, 69, 119-131.
- Yang, K., Huntington, J. F., Browne, P. R., & Ma, C. (2000). An infrared spectral reflectance study of hydrothermal alteration minerals from the Te Mihi sector of the Wairakei geothermal system, New Zealand. *Geothermics*, 29(3), 377-392.
- Yerkes, R. F., & Castle, R. O. (1976). Seismicity and faulting attributable to fluid extraction. *Engineering Geology*, 10(2-4), 151-167.

Appendix A - Results TGA Analysis

Sample: Jan1
Size: 27.4640 mg
Method: Standard

TGA

File: C:\...scriptie 2.0\TGA\wk261100.001

Run Date: 29-Sep-2017 17:52
Instrument: AutoTGA 2950 V5.4A

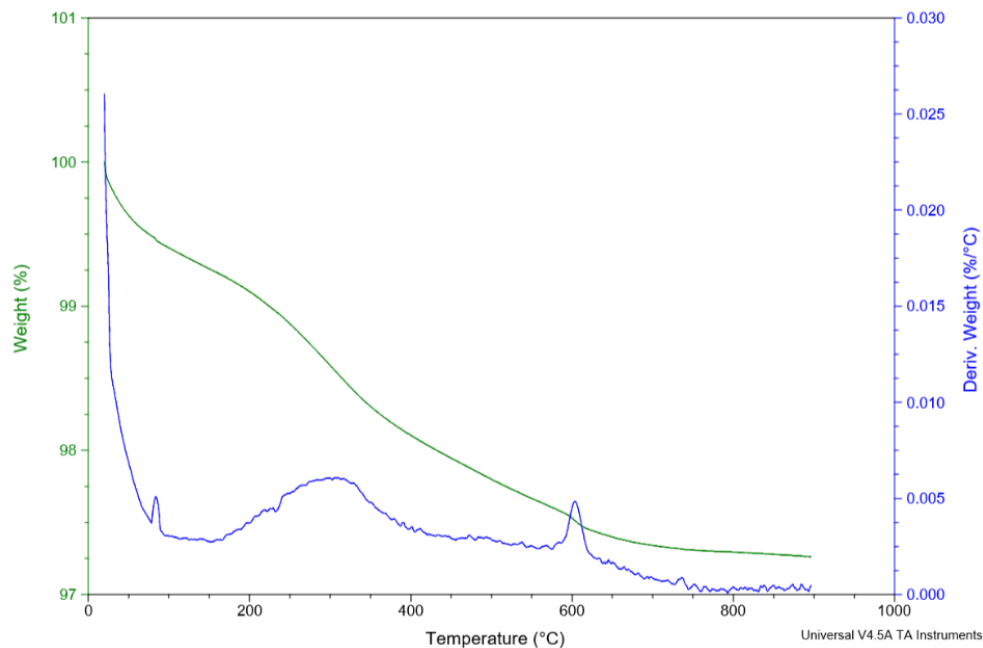


Figure A.1: TGA measurement of wk261-100 showing the decrease in mass and the derivative of weight change with respect to temperature.

Sample: Jan2
Size: 24.7110 mg
Method: Standard

TGA

File: C:\...scriptie 2.0\TGA\wk261700.001

Run Date: 29-Sep-2017 19:52
Instrument: AutoTGA 2950 V5.4A

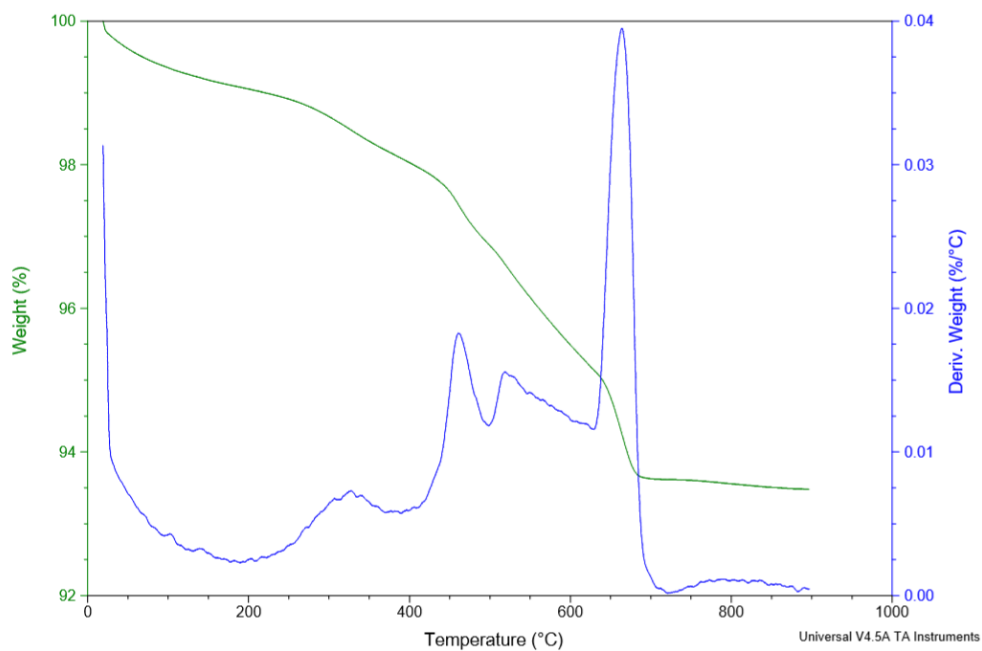


Figure A.2: TGA measurement of wk261-700 showing the decrease in mass and the derivate of weight change with respect to temperature.

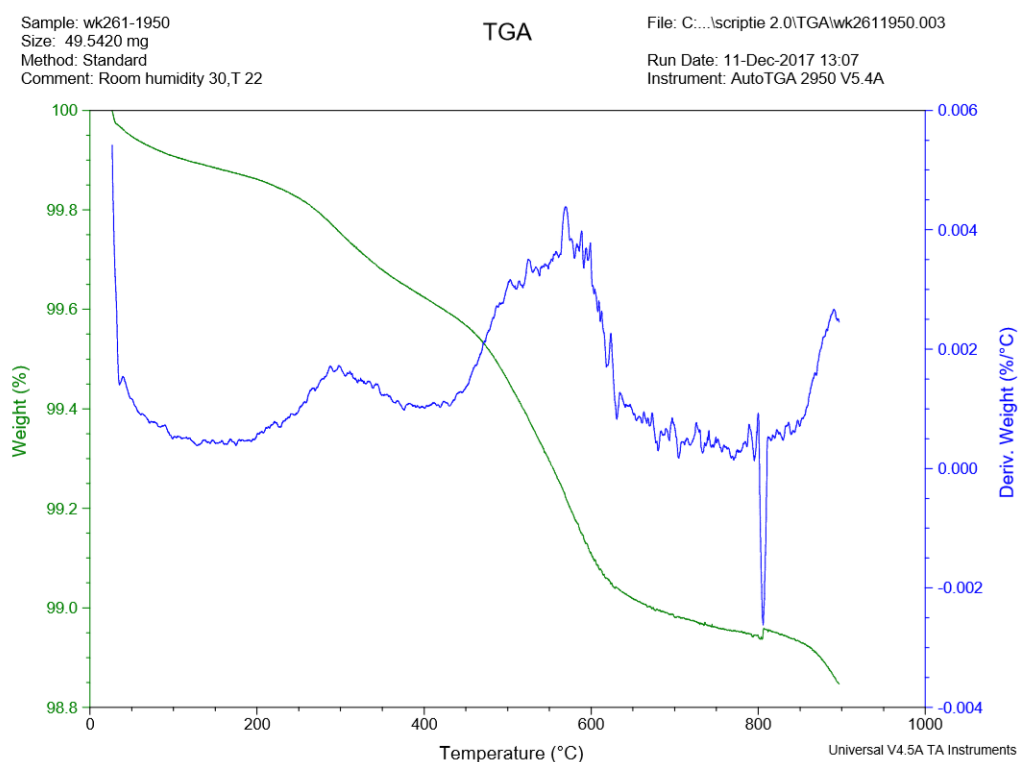


Figure A.3: TGA measurement of wk261-1950 showing the decrease in mass and the derivate of weight change with respect to temperature.

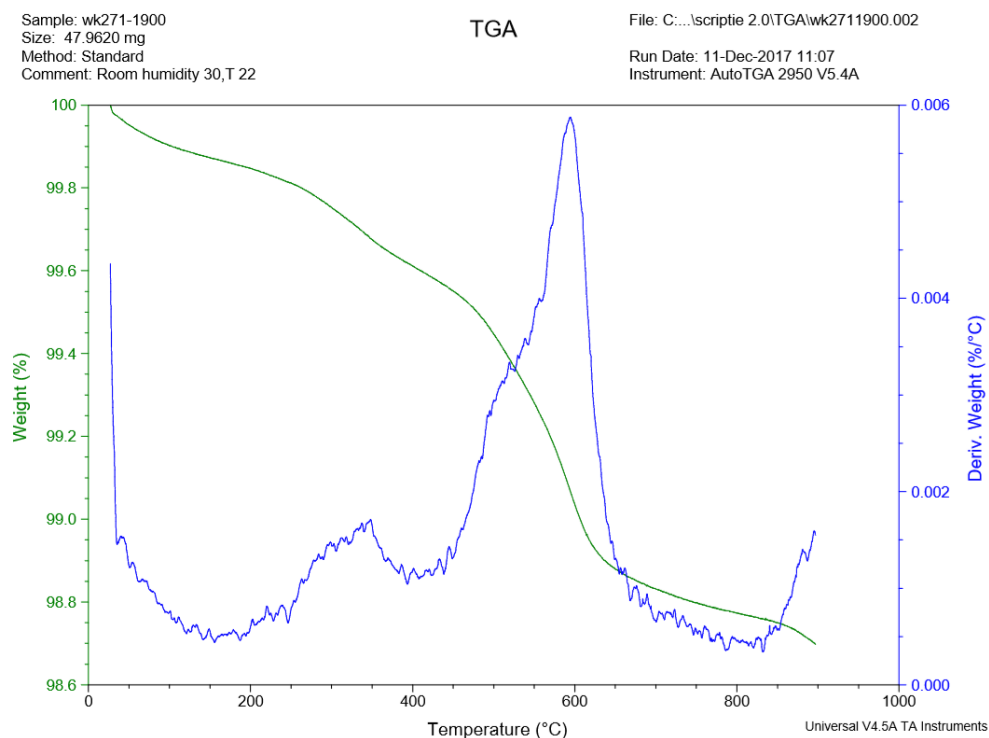


Figure A.4: TGA measurement of wk271-1900 showing the decrease in mass and the derivate of weight change with respect to temperature.

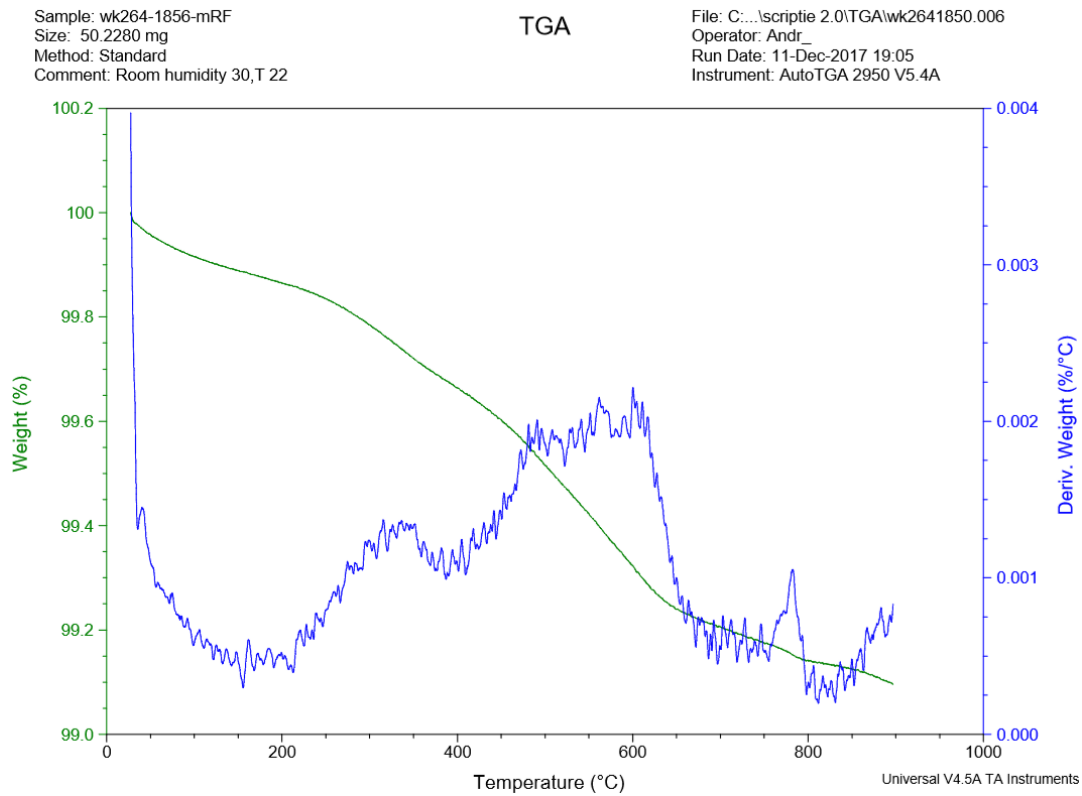


Figure A.5: TGA measurement of wk264-1850 showing the decrease in mass and the derivate of weight change with respect to temperature.

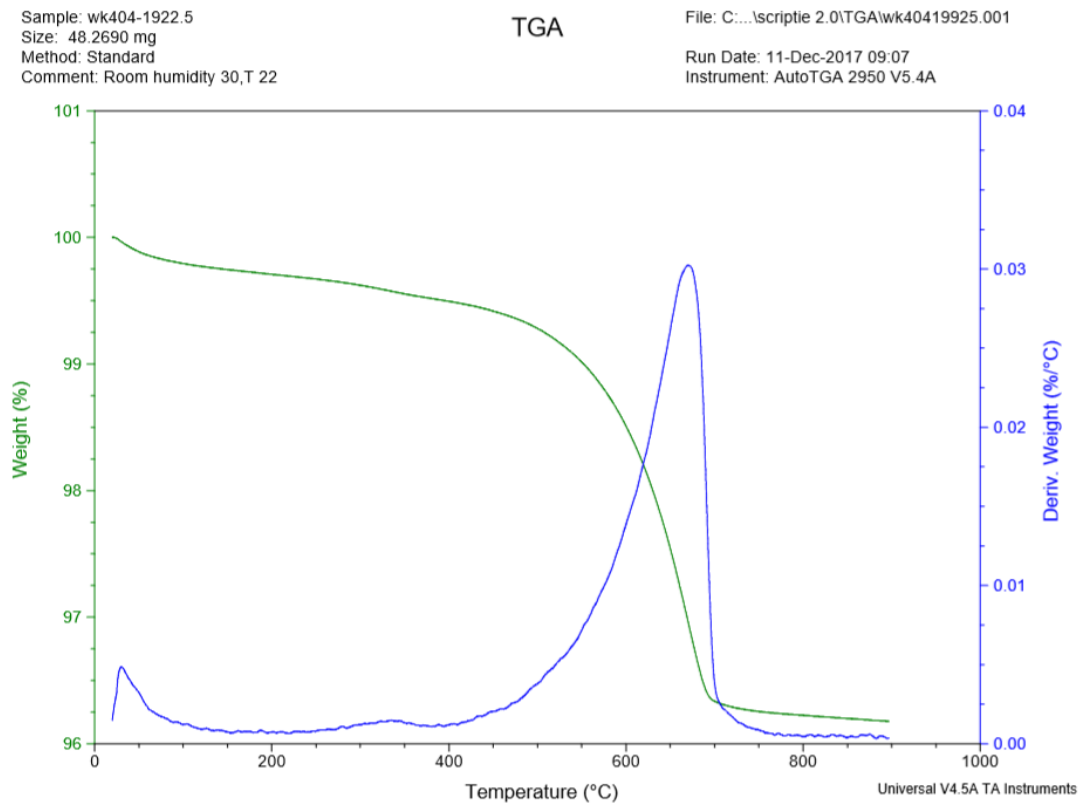


Figure A.6: TGA measurement of wk404-1922.5 showing the decrease in mass and the derivate of weight change with respect to temperature.

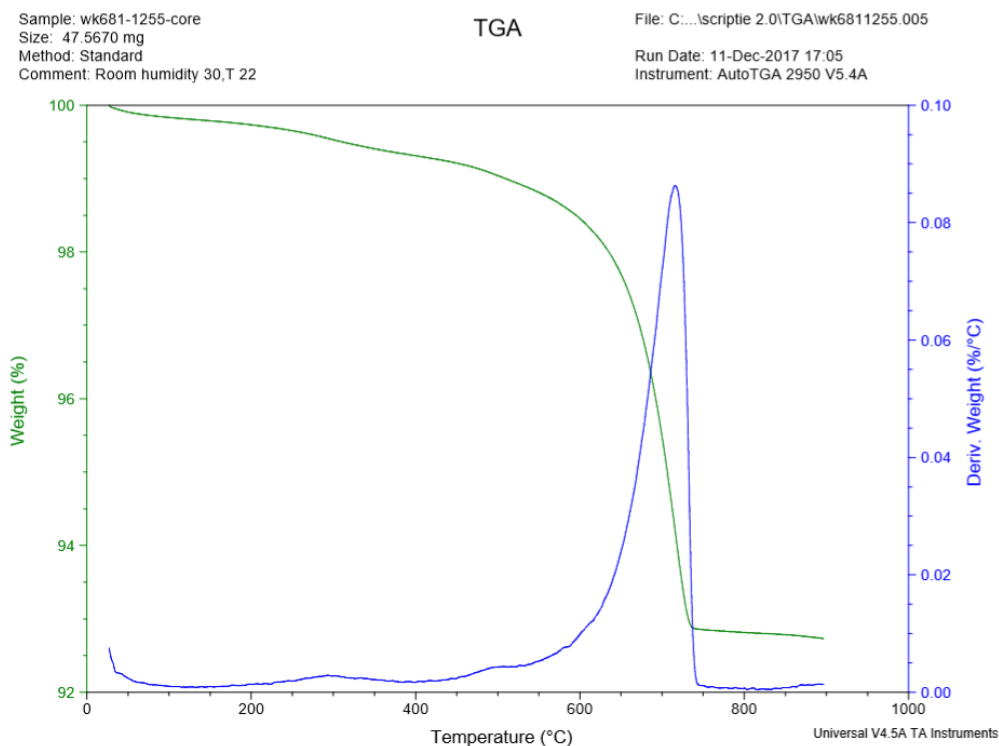


Figure A.8: TGA measurement of wk681-1255 showing the decrease in mass and the derivate of weight change with respect to temperature.

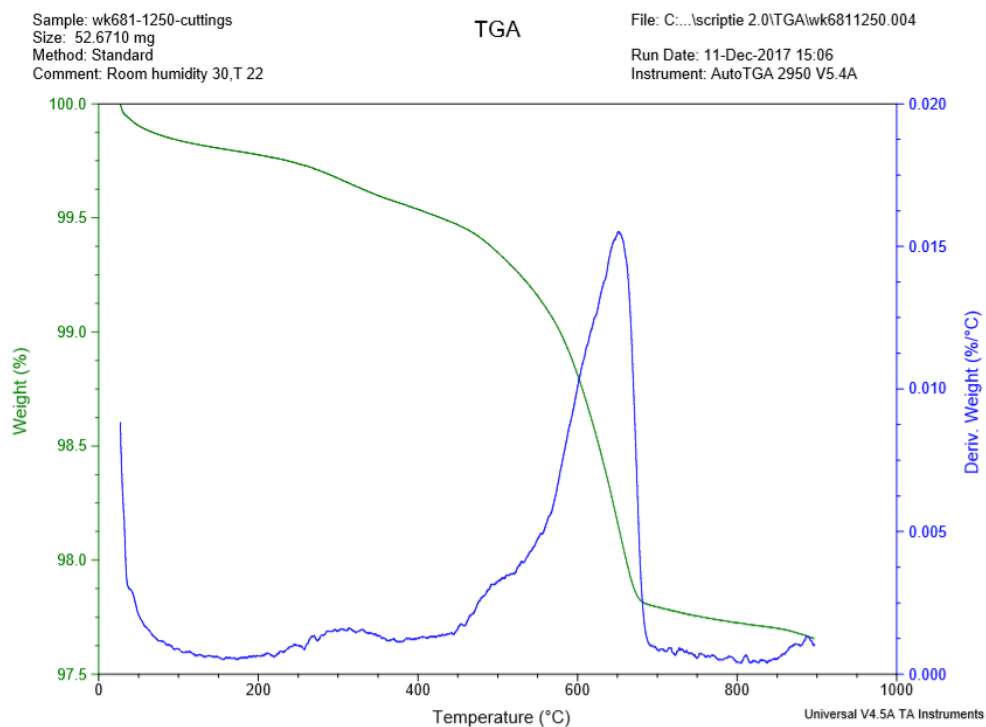


Figure A.8: TGA measurement of wk681-1250 showing the decrease in mass and the derivate of weight change with respect to temperature.

Appendix B - Results XRD Analysis

(Coupled TwoTheta/Theta)

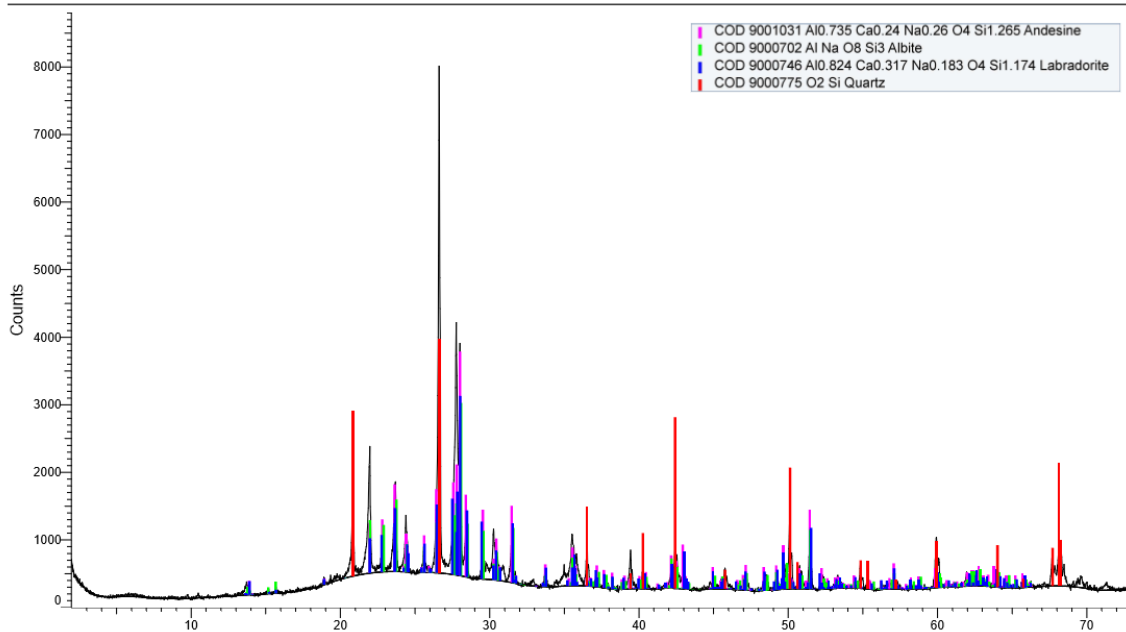


Figure B.1: XRD diffraction pattern sample wk261-100 and the matched minerals.

(Coupled TwoTheta/Theta)

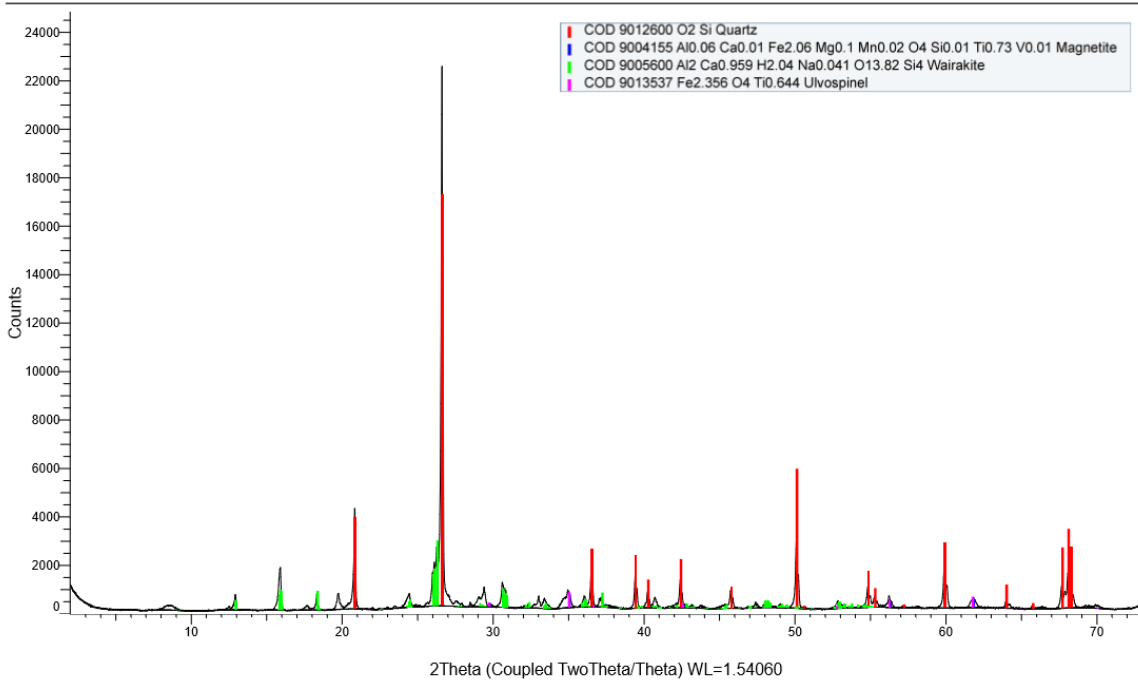


Figure B.2: XRD diffraction pattern sample wk261-700 and the matched minerals.

(Coupled TwoTheta/Theta)

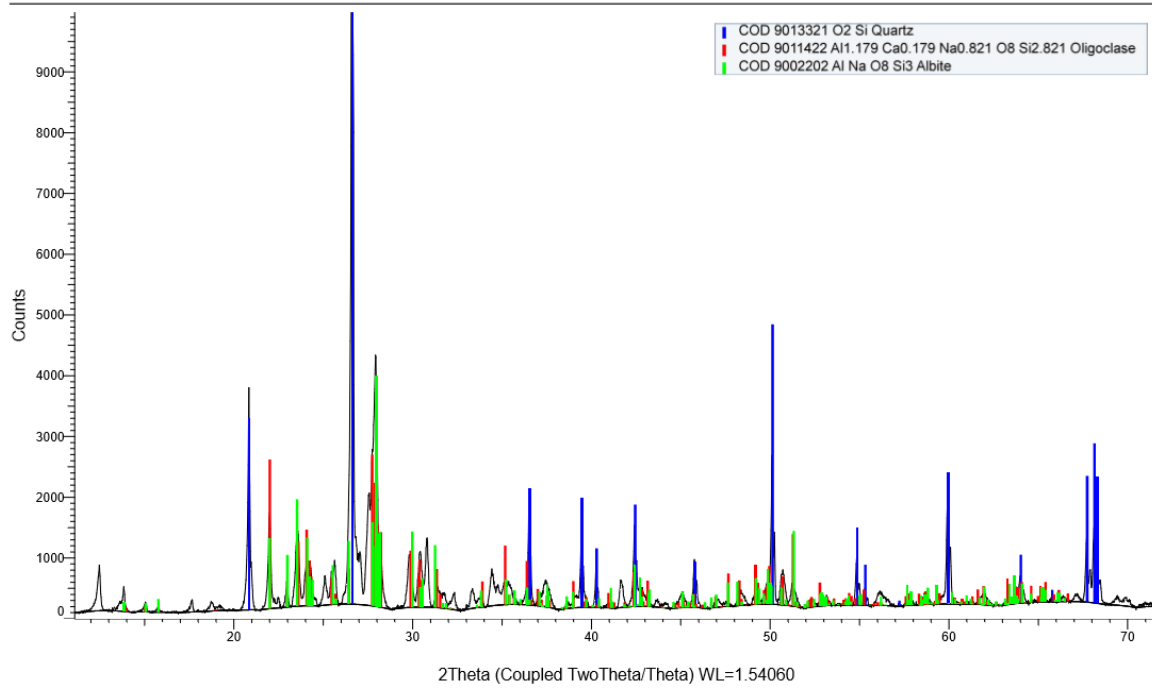


Figure B.3: XRD diffraction pattern sample wk261-1950 and the matched minerals.

(Coupled TwoTheta/Theta)

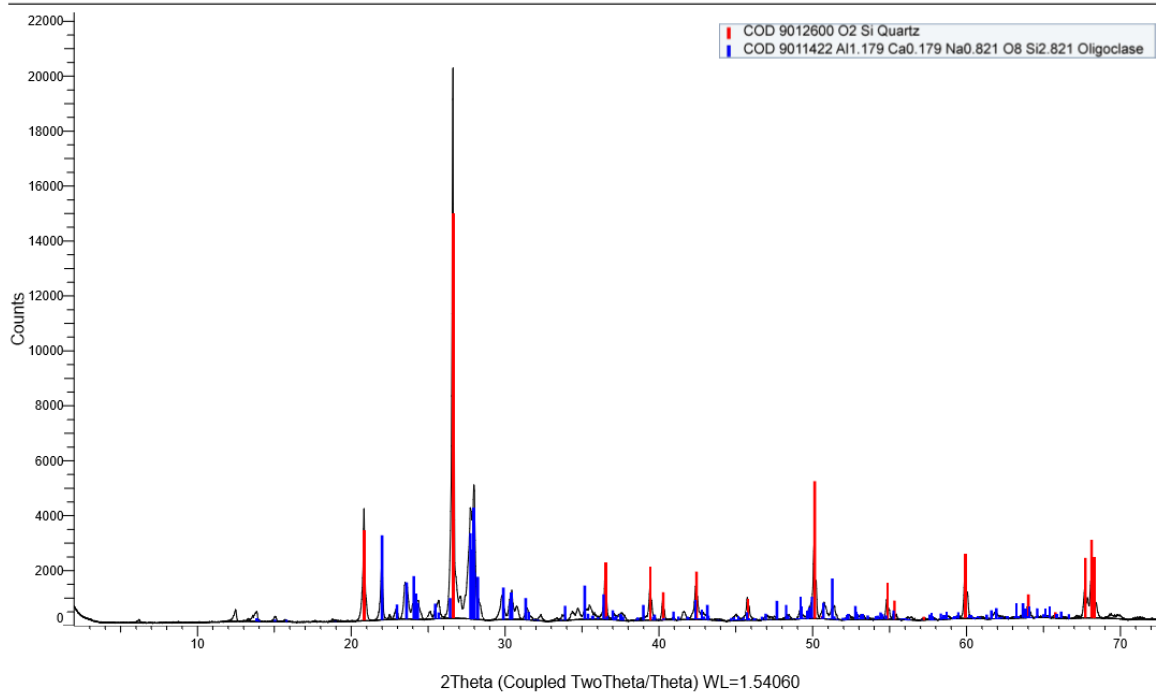


Figure B.4: XRD diffraction pattern sample wk264-1850 and the matched minerals.

(Coupled TwoTheta/Theta)

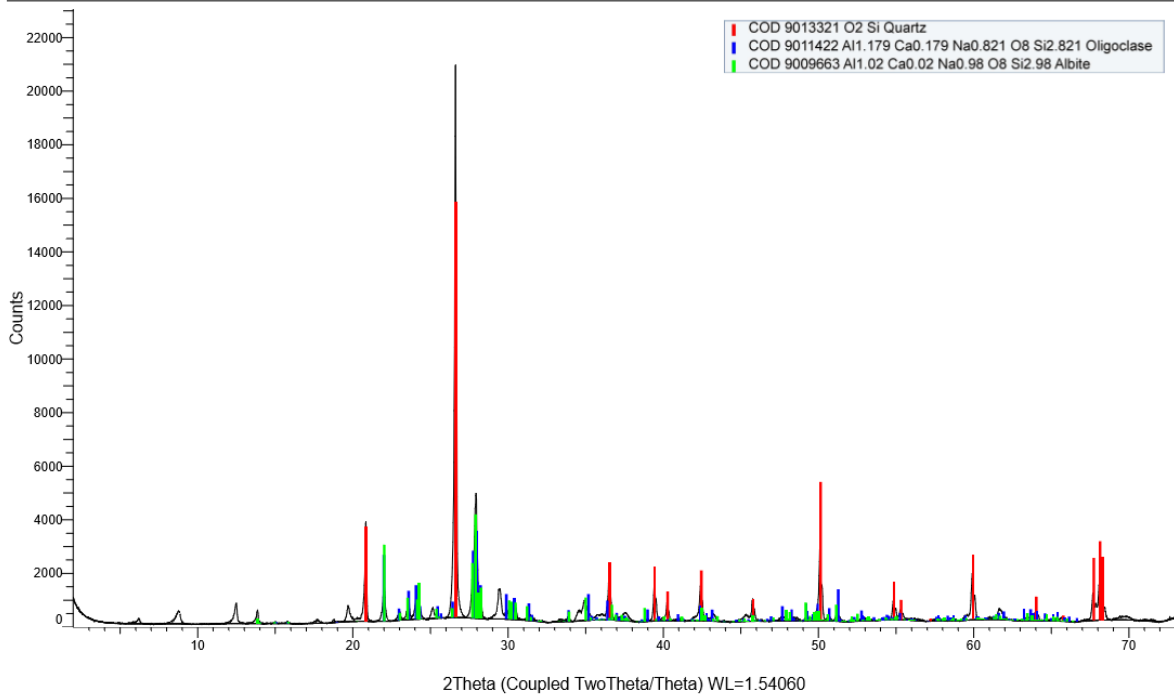


Figure B.5: XRD diffraction pattern sample wk404-1922.5 and the matched minerals.

(Coupled TwoTheta/Theta)

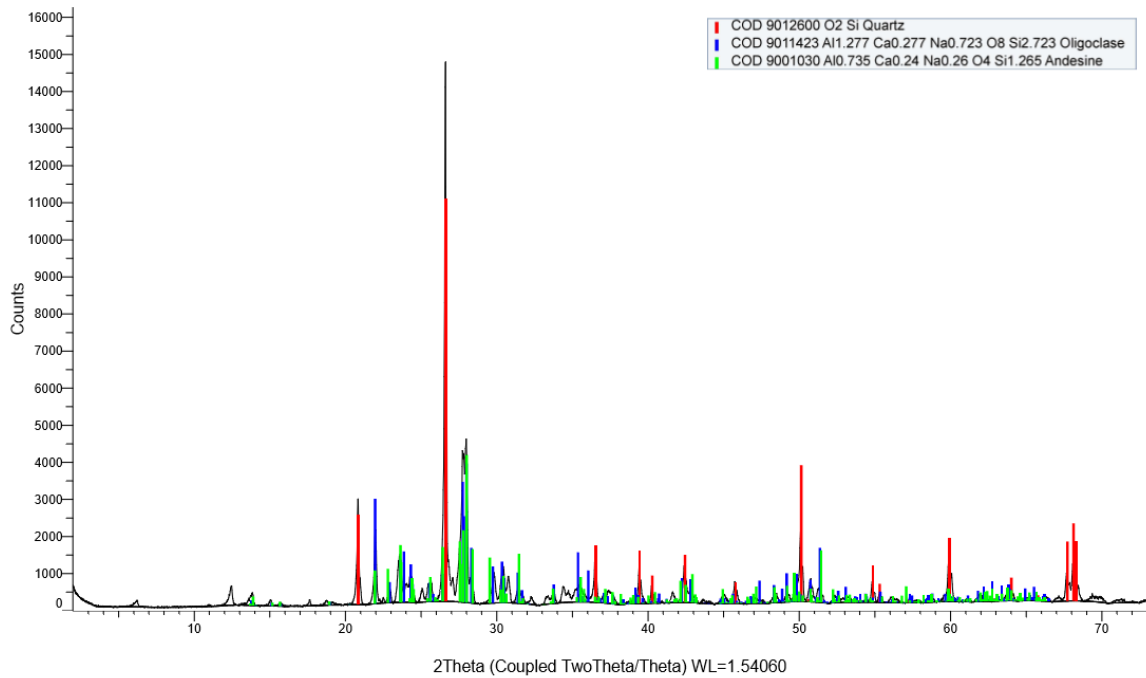
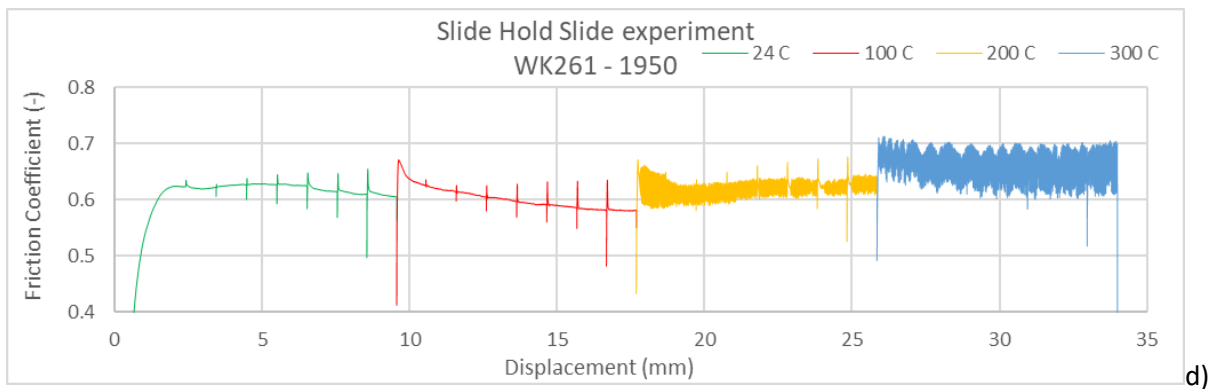
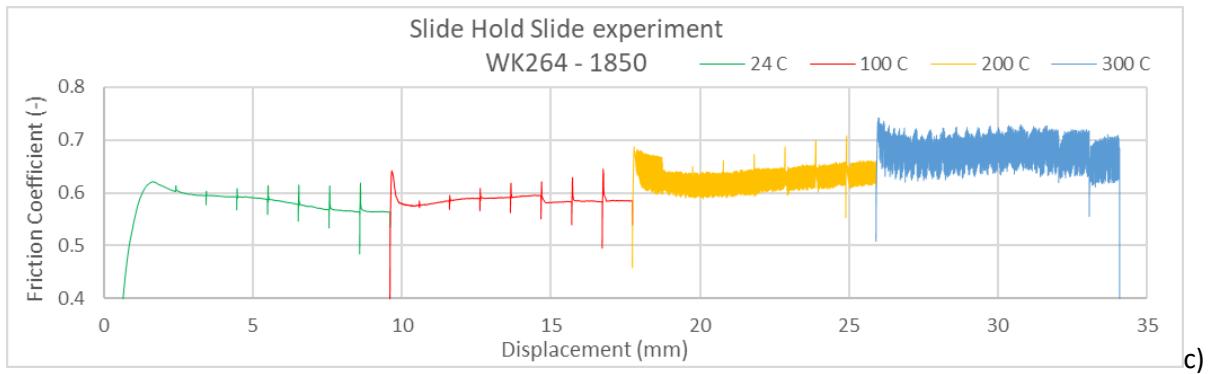
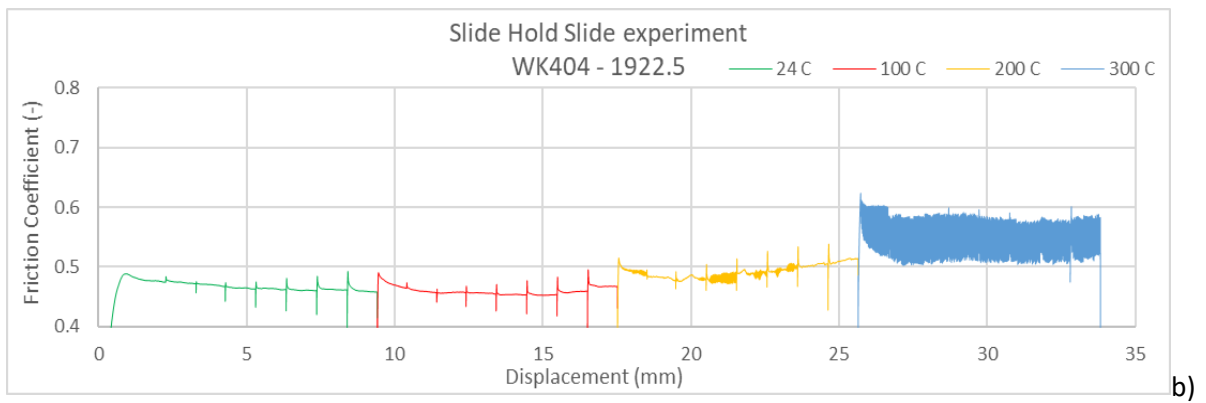
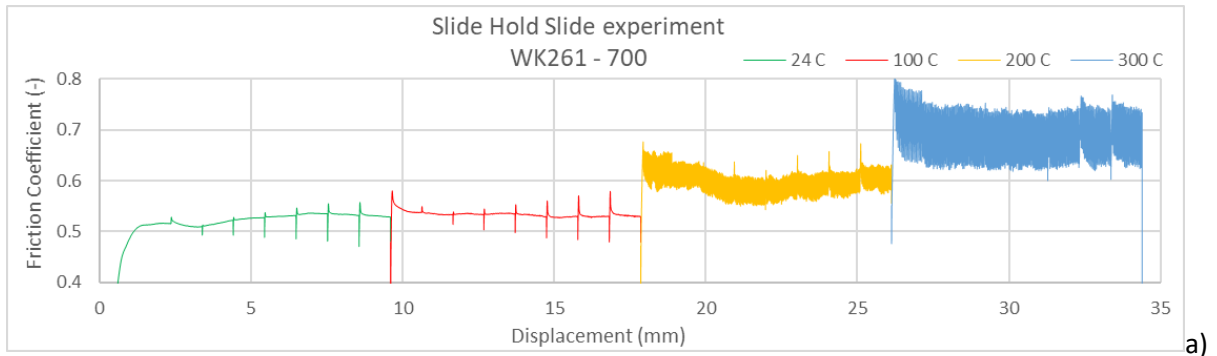


Figure B.6: XRD diffraction pattern sample wk271-1900 and the matched minerals.

Appendix C - Slide-hold-slide experiments



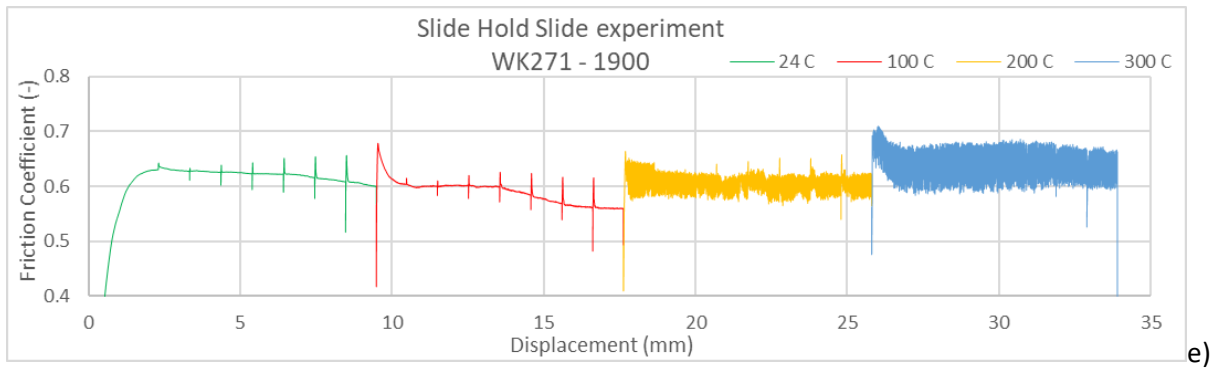


Figure 6.3 a-e: The friction vs. the displacement for the slide hold slide experiments under 50 MPa σ_n and 20 MPa P_f with 6 holds (3-10-30-100-300-1000 s) per temperature, sliding occurs at 3 $\mu\text{m/s}$.